Mechanisms of oxygen bubble formation in a glass melt in the nuclear waste vitrification context

Luiz de Paula Pereira

To cite this version:

Luiz de Paula Pereira. Mechanisms of oxygen bubble formation in a glass melt in the nuclear waste vitrification context. Material chemistry. Université Paris sciences et lettres, 2020. English. NNT : 2020UPSLM033 . tel-03097356

HAL Id: tel-03097356
https://pastel.hal.science/tel-03097356

Submitted on 5 Jan 2021

PSL
UNIVERSITÉ PARIS

THÈSE DE DOCTORAT
DE L'UNIVERSITÉ PSL

Préparée à MINES ParisTech

MÉCANISMES DE FORMATION DE BULLES D'OXYGÈNE DANS UN BAIN DE VERRE FONDU DANS LE CONTEXTE DE LA VITRIFICATION DES DÉCHETS NUCLÉAIRES.

MECHANISMS OF OXYGEN BUBBLE FORMATION IN A GLASS MELT IN NUCLEAR WASTE VITRIFICATION CONTEXT.

Soutenue par
Luiz DE PAULA PEREIRA
Le 12 Novembre 2020

Ecole doctorale n° 364
Sciences Fondamentales et Appliquées (SFA)

Spécialité
Mécanique Numérique et Matériaux

Composition du jury :

Caroline MARTEL
Directrice de Recherche, Université d'Orléans *Rapporteur*

Michel VILASI
Professeur, Université de Lorraine *Rapporteur*

Rudy VALETTE
Professeur, MINES ParisTech *Président*

Jaroslav KLOUŽEK
Professeur Associé, UCT Prague *Examinateur*

Michael TOPLIS
Directeur de Recherche, Université de Toulouse *Examinateur*

Olivier MASBERNAT
Directeur de Recherche, Université de Toulouse *Examinateur*

Annabelle LAPLACE
Ingénieure de Recherche, CEA Marcoule *Encadrante*

Franck PIGEONNEAU
Chargé de Recherche, MINES ParisTech *Directeur de Thèse*

MINES ParisTech | PSL

Dedicated to my family, in particular,
to my beloved grandma Anésia!

Acknowledgements

I am first really greatful to have had Annabelle Laplace and Franck Pigeonneau as PhD suppervisors. Thank you, Annabelle, for the great scientific rigor, valuable discussions, patiance, and huge support over these three years. Thank you, Franck, for the enthusiams, patiance, and vital discussions. It was a really pleasure to work with you both.

I also would like to thank the jury members for accepting to evaluate this research work and for all discussions and ideas.

I thank CEA (*Commissariat à l'énergie atomique et aux énergies alternatives*) for the finantial support that enable me to do this PhD as well as Florence Bart for hosting me during these three years at SEVT. Thank you!

I also would like to thank you, Jarda Kloužek, and the staff from UCT Prague. Thank you for the time and energy spent during my exhange period in Prague.

I am greatful to have worked in the LDMC in, at the first half, Olivier Pinet's and at the second half, Isabelle Giboire's team. Thank you both for making me feel at home and for the attention, especially to Isabelle during this COVID time.

A huge thank you to the permanent staff (Charlène Vallat, Damien Perret, Elise Regnier, Emilien Sauvage, Isabelle Hugon, Jean-François Hollebecque, Julia Agullo, Jennifer Renard, Muriel Neyret, Lionel Campayo, Maxime Fournier, Stéphane Gin, Sophie Schuller, Sylvain Mure, Sylvain Vaubaillon, Thierry Blisson, Valérie Debono, and Virgnie Ansault) who have given me tremendous technical and human assistence and for providing a good work environment. I must also thank the doctoral students/interns (Aline Dressler, Antony Boyer, Birsen Cansin, Boris Venague, Cloé Laurin, Dylan$^{\text{cabritinho}}$, Erik Hansen, Kolani Paraiso, Léa Wic, Leila Galai, Laura Dhellemmes, Matheus Cruz, Morgane Bisel, Norma Marchado, Olivier Podda, Raphael Penelope, Sara El Hakim, and Sophie Achigar) for the support, good humor^2 and lovely work environment too. It was superb to work with you all!

I would like to thank the CEMEF team that makes me feel welcome during my stays in my doctorate schools. I would like to thank Prof. Elie Hachem and Marie-Françoise Guenegan for helping me during these years. A special thanks to Carlitos Mensah and Corentin Perderiset for hosting me at their place when I stayed for the weekends.

Thank you Rafael Nuernberg, my friend and also scientific collaborator, for all frutiful discussions about science and the beautiful insights that we have obtained together. Thank you for the beers and coyotes we had with Rodrigo and Marcelo too.

I must not forget my good friends Caio Gomes, Élcio Duarte, Mateus França, Lucan Mameri, and Rafael Nuernberg. Thank you for the great support. I am glad to be your friend!

I would like to thank my beloved friends from Avignon (Ana, Ana, Anne, Anne, Aurélie, Bast, Camen, Fanny, Greg, Hélène, Manon, Milton, Pablo, Robin, Tony, Vana, Yann, and Yas), especially the ones from the "coloc JeanMarie" for the time spent during the first lock-down. You all were amazing and the time spent with you has renewed my energies to keep going! Turbines!!!

Gabi Miranda, Romain Gerbi, and Benoît Gros-Flandres for being really good flatmates and people.

I am forever grateful to my family (Anésia, Delma, Edna, Júlia, and Luiz PQ) who supported me, gave me good conditions and examples to keep pushing forward my work and goals in life.

A special thank you goes to Anne Zing. I am glad to have met you. Thank you for understanding and providing me this enormeous support! You have been wonderful!

Thank you, thank you, thank you!

As the brazilian singer-poet Cazuza used to say: "*Sozinho eu não dou conta*". Merci!

Table of Contents

Abstract

This doctorate takes place in the framework of nuclear waste vitrification and it deals with gas production occurring during the high-temperature process. We are focused on molecular oxygen produced by redox reactions of multivalent elements. Indeed, these elements can be found in different contexts, including natural and industrial systems. This thesis aims to understand, fundamentally, the mechanisms of oxygen bubble formation and growth and how they are linked to redox reactions taking place in this context. We have chosen a simplified nuclear glass system composed of a borosilicate glass doped with cerium oxide. To support the understanding of bubble formation and growth in this given context, we characterized the simplified system in terms of physical and thermochemical properties.

First, we studied the mass transfer between an oxygen bubble and the melt, for varying cerium contents (% $\mathrm{Ce_2O_3}$) and oxygen fugacities ($\mathrm{f_{O_2}}$). This study was carried out by both experimental and numerical means. The results confirm that cerium redox reaction significantly enhances the mass transfer, mainly in reduced states and high cerium oxide contents. A theoretical model assuming instantaneous redox reaction and a diffusion dominated by molecular oxygen allows, globally, to explain the experimental results.

Afterward, we expanded the study to a bubble population scenario. This part of the work has also been investigated by both experimental and numerical means. The melting of a granular medium, composed of glass beads, leads to a bubble population nucleated mainly due to air trapping. Assuming that the bubble dynamics is driven by their residence time in the crucible, the overall dynamics at various temperatures is the same. A numerical model based only on mass transfer does not estimate bubble behavior, and consequently coalescence should be taken into account.

Finally, we proposed a novel *in-situ* method to infer bubble volume fraction. We demonstrated the theoretical and technical viability of this novel method by comparing the results with other well-established approaches from the literature.

Keywords: oxide melt, bubbles, redox reaction, experimental approach, and numerical approach.

Résumé

Ce doctorat est réalisé dans le cadre de la vitrification des déchets nucléaires et est focalisé sur la production de gaz formé lors du processus de vitrification à haute température. Nous nous concentrons sur l'oxygène moléculaire produit par des réactions d'oxydo-réduction d'éléments multivalents. En effet, ces éléments sont présents dans plusieurs domaines naturels et industriels. Cette thèse vise à comprendre, fondamentalement, les mécanismes de formation et de croissance des bulles d'oxygène et comment ceux-ci sont liés aux réaction d'oxydo-réduction se déroulant dans ce contexte. Nous avons choisi un système de verre nucléaire simplifié composé d'un verre borosilicaté dopé avec l'oxyde de cérium. Pour étayer notre compréhension de la formation et de la croissance des bulles, nous avons caractérisé le système simplifié en termes de propriétés physiques et thermochimiques.

Nous avons tout d'abord étudié le transfert de masse entre une bulle d'oxygène et la fonte verrière avec différentes teneurs en cérium (% $\mathrm{Ce_2O_3}$) et différentes fugacités en oxygène ($\mathrm{f_{O_2}}$). Cette étude a été menée à la fois par des moyens expérimentaux et numériques. Les résultats confirment que la réaction d'oxydo-réduction du cérium augmente de façon significative le transfert de masse pour les milieux réduits et à forte teneur en oxyde de cérium. Un modèle théorique considérant les réactions d'oxydo-réduction comme instantanées et une diffusion dominée par celle de l'oxygène permet globalement de retrouver les résultats expérimentaux.

Nous avons ensuite étendu le système à une population de bulles. Cette partie de la thèse a également été abordée par des moyens expérimentaux et numériques. En faisant fondre un milieu granulaire, constitué de grains de verre, la nucléation des bulles est principalement liée à l'emprisonnement de l'air. En considérant que la dynamique des bulles est pilotée par leurs temps de résidence dans le creuset, le comportement des bulles à différentes températures se révèle équivalent. Un modèle numérique basé sur le simple transfert de masse ne permet pas d'estimer le comportement des bulles, ainsi la coalescence des bulles devrait être prise en compte.

Enfin, nous avons proposé une nouvelle méthode *in-situ* pour déterminer la fraction volumique des bulles. Nous avons démontré la viabilité théorique et technique de cette nouvelle méthode en utilisant d'autres approches robustes de la littérature.

Mots-clefs : fonte de verre d'oxyde, bulles, réaction d'oxydo-réduction, méthode expérimentale, méthode numérique.

Communications

Articles in Journals

Pigeonneau F, **Pereira L**, Laplace A. "Sherwood number on a bubble rising in a glass former liquid coupled to reversible oxidation-reduction reaction". *Chemical Engineering Science*. (**Submitted**).

Pereira L, Neyret M, Laplace A, Pigeonneau F, Nuernberg, R. "Inferring bubble volume fraction through *in-situ* impedance spectroscopy measurements". *International Journal of Applied Glass Science.* (**Submitted**).

Pereira L, Kloužek J, Vernerová M, Laplace A, Pigeonneau F. "Experimental and numerical investigations of an oxygen single-bubble shrinkage in a borosilicate glass-forming liquid doped with cerium oxide". *Journal of the American Ceramic Society*. **2020**. https://doi.org/10.1111/jace.17398.

Pereira L, Podda O, Fayard B, Laplace A, Pigeonneau F. "Experimental study of bubble formation in a glass-forming liquid doped with cerium oxide". *Journal of the American Ceramic Society*. **2020**. https://doi.org/10.1111/jace.16950.

Talks in Congresses

Pereira L, Laplace A, Pigeonneau F. "Mechanism of O_2 bubble formation in borosilicate melts". *Annual Conference of the Society of Glass and Technology*. Cambridge, United Kingdom. **2019**.

Pereira L, Laplace A, Pigeonneau F. "Oxygen bubble formation due to oxidation-reduction reactions in borosilicate glasses". *Conference Matériaux 2018.* Strasbourg, France. **2018**.

Prizes

Pereira L, Laplace A, Pigeonneau F. "Mechanism of oxygen bubble formation in a glass melt in nuclear waste vitrification context". 3rd Prize Pierre Laffitte, Sophia Antipolis, France. **2019**. Worth 500€.

Notations

Latin letters

Symbol	Name	Units
a	bubble radius	m
A	sample surface area	m^2
a_0	initial bubble radius	m
A^{diff}_i	diffusion pre-exponential constant	$m^2.s$
A_i	pre-exponential factor for ionic conductivity	$\Omega^{-1}.m^{-1}.K$
A^{sol}_i	solubility pre-exponential constant	$mol.m^{(2.\beta i-3)}.N^{(-\beta i)}$
B^{diff}_i	diffusion exponential constant	K
β_i	saturation exponent of gas i	-
B^{sol}_i	solubility exponential constant	K
C^{∞}_i	gas i concentration on melt bulk	$Kg.m^{-3}$ or $mol.m^{-3}$
$CPE_{i(g)}$	constant phase element of the glass (ionic contribution)	F
$CPE_{p(2e)}$	constant phase element of the two-electrodes (polarization effect)	F
C^s_i	gas i concentration on bubble surface	$Kg.m^{-3}$ or $mol.m^{-3}$
C^x_i	gas i concentration in the x situation	$Kg.m^{-3}$ or $mol.m^{-3}$
d^{2D}	2D bubble mean diameter	m
d^{3D}	3D bubble mean diameter	m
D_i	diffusivity of gas i	$m^2.s^{-1}$
d_{max}^{2D}	2D maximum bubble mean diameter	m
d_{max}^{3D}	3D maximum bubble mean diameter	m
E_a	activation energy for ionic conductivity	J
fO_2	oxygen fugacity	Pa
g	gravity acceleration	$m.s^{-2}$
H	melt height	m
h_i	convection mass transfer coefficient	$m.s^{-1}$
i	notation for a random gas species	-
J	diffusive mass flux	$Kg.m^{-2}.s^{-1}$
K_B	Boltzmann constant	$J.K^{-1}$
K_i	oxide coefficient for Fe redox model - Kress et al. (1991)	-
k_s	reaction constant of attachment	$m\cdot s^{-1}$
L	sample thickness	m
$L_{(w)}$	inductance of the wires	H
L_i	Henry coefficient of gas i	$mol.m^{(-3)}.Pa^{(-\beta i)}$

N_b^{2D}	2D bubble mean density	m^{-2}
N_b^{3D}	3D bubble mean density	m^{-2}
N_{Ce}	dimensionless Ce number	-
N_g	number of gaseous species	-
n	number of exchanged electrons in a redox reaction	
n_i	number of moles of gas i	mol
p	internal bubble pressure	Pa
P_0	atmospheric pressure	Pa
Pe	Péclet number	-
Pe'	modified Péclet number	-
Pe'_i	modified Péclet number under the initial conduction	-
P_{ij}	film rupture probability	-
PO_2	oxygen partial pressure	Pa
P^x_i	gas i partial pressure in the x situation	Pa
R	idea gas constant	$J{\cdot}K^{-1}{\cdot}mol^{-1}$
R	electrical resistance	Ω
R^∞	cerium redox state	-
$R_{bubbled}$	electrical resistance bubbled-glass	Ω
$R_{bubbled}$	electrical resistance bubbled-glass	Ω
$\rho_{bubble\text{-}free}$	overall density of bubble-free glass	$Kg.m^{-3}$
$R_{bubble\text{-}free}$	electrical resistance of bubble-free glass	Ω
$R_{bubble\text{-}free}$	electrical resistance of bubble-free glass	Ω
$R_{i(g)}$	resistance of the glass (ionic contribution)	Ω
$R_{i(l)}$	resistance of the liquid (ionic contribution)	Ω
S	supersaturation	-
Sa	saturation ratio	-
Sh_i	Sherwood number of gas i	-
T	temperature	K or °C
t	time	s
T_g	glass transition temperature	K
T_w	wall crucible temperature	K
V_T	bubble terminal velocity	$m.s^{-1}$
W_A	sample weight in air	Kg
W_N	weight with no sample	Kg
W_W	sample weight in water	Kg
X_i	oxide molar fraction for Fe redox model - Kress et al. (1991)	-
z	bubble vertical position	m
Z’	real part of specific impedance	Ω.m or Ω
Z’’	imaginary part of specific impedance	Ω.m or Ω

Notations

Greek letters

Symbol	Name	Units
α	mass transfer coefficient of the modified Péclet number	-
β	angular coefficient of normalized mass transfer coefficient	-
β'	mass transfer integration constant	-
δ	melted glass thickness	m
ΔE	electrochemical potential difference	$kg \cdot m^2 \cdot s^{-3} \cdot A^{-1}$
ΔG	Gibbs free energy	J
ΔG_{hetero}	Gibbs free energy heterogeneous nucleation	J
ΔG_{homo}	Gibbs free energy homogeneous nucleation	J
ΔG_v	Gibbs bulk free energy per unit of volume	$J.m^{-3}$
ΔP_s	supersaturation pressure difference	Pa
ε	effective emissivity	-
ϕ_b	bubble fraction	-
ϕ_b^{2D}	2D bubble fraction or bubble surface fraction	-
ϕ_b^{3D}	3D bubble fraction or bubble volume fraction	-
γ'	redox activity coefficient	-
η	glass melt viscosity	Pa.s
ϑ_{ij}	molar volume of dispersed phase	$m^3 \cdot mol^{-1}$
Λ	optical basicity	-
λ	thermal conductivity	$W.m^{-1}.K^{-1}$
θ	contact angle	°
ρ_a	air density	$Kg.m^{-3}$
$\rho_{bubbled}$	overall density bubbled-glass	$Kg.m^{-3}$
ρ_{gran}	density of glass granular medium	$Kg.m^{-3}$
ρ	glass / melt density	$Kg.m^{-3}$
ρ_w	water density	$Kg.m^{-3}$
σ	surface tension	$N.m^{-1}$
$\sigma_{bubbled}$	ionic conductivity of bubbled-glass	$\Omega^{-1}.m^{-1}$
$\sigma_{bubble\text{-}free}$	ionic conductivity of bubble-free glass	$\Omega^{-1}.m^{-1}$
σ_{gas}	ionic conductivity of gas	$\Omega^{-1}.m^{-1}$
σ_i	ionic conductivity	$\Omega^{-1}.m^{-1}$
σ_{SB}	Stefan-Boltzmann constant	$W.m^{-2}.K^{-4}$
τ	characteristic time for mass transfer	s
t_η	characteristic bubble residence time	s
Ω_{ij}	coalescence rate	s^{-1}
ω_{ij}	collision frequency	s^{-1}

Chapter 1

Introduction

Chapitre 1

Introduction

Résumé : Ce chapitre est dédié à la présentation du contexte de ce travail, c'est-à-dire, la vitrification des déchets nucléaires. Dans ce contexte de vitrification à haute température, nous présentons les espèces gazeuses impliquées, dont l'oxygène qui peut être formé par réaction d'oxydo-réduction entre deux couples redox, comme par exemple : $\mathrm{Ce(IV)}/\ \mathrm{Ce(III)}$ et $\mathrm{O_{2(g)}}/\mathrm{O^{2-}}$. Nous présentons ensuite le système vitreux simplifié, qui est composé d'un verre borosilicaté dopé avec un élément multivalent (cérium). A la fin de ce chapitre, les objectifs de cette thèse ainsi que la démarche scientifique appliquée sont présentés.

Chapter 1

Introduction

1.1 Nuclear waste vitrification

Nuclear reactors are driven by the splitting of atoms, which is called nuclear fission. This split comes from the collision of an external neutron with fissile atoms (*e.g.* ^{235}U and ^{239}Pu). This collision releases a great amount of energy, smaller atoms and neutrons. Some of these released neutrons hit other atoms, causing them to fission as well and release more neutrons. Thus, the chain reaction is established. Controlling rods, which are typically made of neutron absorbing materials, such as boron, are used to ensure that nuclear fission reaction takes place at the right speed, allowing the operators to accelerate, slow and shut the reactor. This mentioned released energy is removed from the reactor by a circulating fluid (typically water). Thus, this heat is used to generate steam, which drives turbines for electricity production.

After being used in the reactor, the nuclear fuel usually goes through a recovery process which aims to retrieve plutonium and uranium from the spent fuel. The separation process used for light water reactor (LWR) oxide fuel adopted in some well-known reprocessing plants, such as La Hague (France) and Sellafield (UK), is the hydrometallurgical process based on plutonium and uranium refining by extraction (PUREX).[1] To date, up to 96 % of the spent fuel can be recovered into plutonium and uranium, but still 4 % become waste. This nuclear waste contains fission product (FP) mixed with minor actinides (MA), which belong to the waste type called high-level waste (HLW). Vitrification is the current choice to immobilize these two former by-products.[1] Not only HLW is vitrified nowadays in France, but also intermediate-level waste long-lived (ILW-LL). They can be found in different scenario, such as nuclear decommissioning, and legacy waste treatment. Indeed, in France, the first demonstration of the feasibility of the vitrification process was carried out at Marcoule nuclear site in the late 1960's.[2] Vitrification is not a simple encapsulation procedure, but consists of making a new material, in which the glass matrix is chemically bonded to the atoms from the waste and it can be only released by destruction of the network bond.[1] In terms of vitrification of nuclear waste, most of the countries have adopted borosilicate glass composition as a hosting matrix.[3] It can also be highlighted the use of phosphate glasses to immobilize nuclear waste.[4] The final nuclear glass can guarantee a long term durability and, due to the glass network disorder, it is possible to incorporate a wide range of elements.[5,6]

1.2 Bubble formation in nuclear waste glass melts

Several types of gases and possibly bubbles release might be observed in vitrification processes of nuclear waste. One can highlight bubble formed during the high-temperature melting process, such as N_2, CO_2, O_2.[1] Nitrogen may come from entrapped air, while carbon dioxide may come from the glass precursors and molecular oxygen is mainly formed by redox reactions of multivalent elements. The gas composition depends on the feed/glass composition, the glass melting process, as well as the stage of the process which is analyzed.[7-9] Nuclear waste contains different multivalent elements such as cerium, ruthenium, iron, chromium and molybdenum.[1,3] In molten oxide glasses, due to its great amount, O_2^{diss}/O^{2-} redox couple is involved in redox reactions. O_2^{diss} is the physically dissolved oxygen, while O^{2-} is the oxygen ion. Thus, Eq. (1.1) presents a redox reaction of a general redox couple $(M^{m+}/M^{(m-n)+})$ in a molten oxide glass.

$$M^{m+} + \frac{n}{2} O^{2-} \rightleftarrows M^{(m-n)+} + \frac{n}{4} O_{2(g)}. \tag{1.1}$$

As this equation progresses towards the right, molecular oxygen forms until it reaches the saturation of the glass melt. This saturation is characterized as the maximum amount of gas that can be dissolved at a given temperature under a given pressure.[10] Therefore, after overtaking this saturation threshold, the gas in question would be more energetically stable in a gaseous phase than solubilized. It has been experimentally observed that higher temperature lead to more reduced states for the most of the multivalent elements, favoring then molecular oxygen production.[11-13]

In the literature, there are articles related to redox reactions of multivalent elements in molten glasses[11-16] as well as to bubble formation in magmas.[17-20] In this latter field, the formation of bubbles is a natural event, which happens in silicate-based melts and the formed bubbles are generally composed by H_2O and/or CO_2 gases.[19,20] Bubble formation is also researched in the field of glass making industry.[21-23] In these investigations, the nucleation, growth and behavior of bubbles are taken into account. Still in this industrial field, N_2, CO_2, H_2O might come from raw materials and from the processes itself, while SO_2 and O_2 might be generated in the so-called fining stage, which is also composed by a redox reaction.[21] My thesis work is articulated therefore in the hiatus of these two subjects: the production of molecular oxygen by a redox reaction and bubble formation linked to that.

1.3 PhD thesis

1.3.1 PhD general goals

The goal of this PhD research is to answer some fundamental questions regarding bubble formation in nuclear vitrification context linked to redox reactions. Thus, this work is rather a fundamental research and some of the basic questions are presented herein:

- Type of bubble nucleation. We aim to comprehend how bubbles nucleate in this type of oxide melt and describe the main parameters related to this nucleation process.
- Growth mechanism. Once bubbles are nucleated, how do they grow over time? We aim to distinguish their growth mechanism and characterize it with the physical laws described in the literature.
- Bubble behavior over time. How do bubble features (bubble mean density, bubble mean diameter and bubble fraction) evolve in the molten glass.
- Bubble behavior as function of temperature. Do these previous bubble features behave similarly with temperature? Is the governing mechanism the same at different temperatures?
- Computational modeling. Once the previous questions are answered, is that possible to apply computational models to the current system in order to make predictions? Do these models estimate well bubble behavior coupled with redox reaction in the researched melt system?

Therefore, one can generalize the goal of this PhD research as the "fundamental comprehension of oxygen bubble formation in a glass melt linked to a redox reaction of multivalent elements coming from nuclear waste".

1.3.2 Scientific approaches

In this doctorate work, we firstly simplified the melt system to study oxygen bubble formation in the aforementioned context. We chose a borosilicate glass doped with cerium oxide as the simplified glass system. A borosilicate composition has been selected due to its widely use as nuclear waste host matrix and cerium oxide due to its redox power, possible presence in different nuclear waste and influence on bubble formation.[13] Besides, one of the methods used to study bubbles in this thesis, camera *in-situ* imaging, requires light transmission, which is possible in the mentioned composition up to few percent of cerium.

Once the glass system was designated, we first studied an oxygen bubble immersed and rising in this borosilicate melt doped with cerium oxide. We focused on the mass transfer between a freely rising bubble and the mentioned melt containing different amounts of cerium (wt% $\mathrm{Ce_2O_3}$) and having different redox ratios $(\mathrm{Ce(III)/Ce_{total}})$. This study was carried out by experimental means, using *in-situ* camera approach, along with numerical simulations of mass transfer. Then, by enlarging the studied domain to a bubble population system, we carried out experiments and mass transfer numerical calculations to better understand the laws which govern this new system. Bubble visualization, in this expanded system, was investigated by *post-mortem* optical microscopic approach on solid samples. Several physical-chemical characterizations were carried out in order to acquire data to support the understanding of the system as well as to feed the numerical simulation codes. Lastly, due to the laborious and time-consuming characteristic of the experimental approach to study the bubble population system (optical microscopy), we proposed a novel *in-situ* method to infer bubble volume fraction based on the difference of ionic conductivity between a bubbled glass and its correspondent bubble-free glass.

In this thesis manuscript, it is first presented a state-of-art which contains redox phenomenon of the main relevant multivalent elements in nuclear waste vitrification context along with bubble nucleation and growth in molten glasses (chapter 2). Afterward, we present the studied material and the executed characterizations (chapter 3), they will be useful as input values for the computational modeling as well as to support the interpretation of the bubble observation results. The fourth and fifth chapters are dedicated, respectively, to the investigations of the oxygen single-bubble and the bubble population systems. In these two chapter both experimental and computer simulations are applied. Moreover, we dedicate the sixth chapter to describe the use of high-temperature impedance spectroscopy as a novel *in-situ* technique to infer bubble volume fraction in melts. It is validated by comparing with other well-established methods in the literature. Lastly, in the conclusion chapter we present the general insights obtained during this PhD thesis and also some perspectives for future works.

1.4 References

(1) Vernaz, E.; Gin, S.; C, V.; Elsevier: Amsterdam, **2012**; Vol. 5, p 451.

(2) Vernaz, É.; Bruezière, J. *Procedia Materials Science* **2014**, *7*, 3.

(3) Plodinec, M. J. *Glass Technology* **2000**, *41*, 186.

(4) Brow, R. K.; Kim, C. W.; Reis, S. T. *International Journal of Applied Glass Science* **2020**, *11*, 4.

(5) Pinet, O.; Hugon, I.; Mure, S. *Procedia Materials Science* **2014**, *7*, 124.

(6) Fournier, M.; Gin, S.; Frugier, P. *Journal of Nuclear Materials* **2014**, *448*, 348.

(7) Luksic, S. A.; Pokorny, R.; George, J.; Hrma, P.; Varga, T.; Reno, L. R.; Buchko, A. C.; Kruger, A. A. *Ceramics International* **2020**, *46*, 17176.

(8) Hujova, M.; Klouzek, J.; Cutforth, D.; Lee, S.; Miller, M.; Kruger, A.; Hrma, P.; Pokorny, R. *Ceramics International* **2020**, *46*, 9826.

(9) Lee, S.; Hrma, P.; Kloužek, J.; Pokorny, R.; Hujová, M.; Dixon, D. R.; Schweiger, M. J.; Kruger, A. A. *Ceramics International* **2017**, *43*, 13113.

(10) Jones, S. F.; Evans, G. M.; Galvin, K. P. *Advances in Colloid and Interface Science* **1999**, *80*, 27.

(11) Rüssel, C. *Journal of Non-Crystalline Solids* **1990**, *119*, 303.

(12) Russel, C. *Glastechnische Berichte* **1989**, *62*, 199.

(13) Pinet, O.; Phalippou, J.; Di Nardo, C. *Journal of Non-Crystalline Solids* **2006**, *352*, 5382.

(14) Pinet, O.; Mure, S. *Journal of Non-Crystalline Solids* **2009**, *355*, 221.

(15) Kress, V. C.; Carmichael, I. S. E. *Contributions to Mineralogy and Petrology* **1991**, *108*, 82.

(16) Kress, V. C.; Carmichael, I. S. E. *American Mineralogist* **1988**, *73*, 1267.

(17) Yamada, K.; Emori, H.; Nakazawa, K. *Earth, Planets and Space* **2008**, *60*, 661.

(18) Mourtada-Bonnefoi, C. C.; Laporte, D. *Journal of Geophysical Research: Solid Earth* **2002**, *107*, 2.

(19) Martel, C.; Bureau, H. *Earth and Planetary Science Letters* **2001**, *191*, 115.

(20) Parmigiani, A.; Faroughi, S.; Huber, C.; Bachmann, O.; Su, Y. *Nature* **2016**, *532*, 492.

(21) Boloré, D.; Pigeonneau, F. *Journal of the American Ceramic Society* **2018**, *101*, 1892.

(22) Pigeonneau, F.; Martin, D.; Mario, O. *Chemical Engineering Science* **2010**, *65*, 3158.

(23) Vernerová, M.; Kloužek, J.; Němec, L. *Journal of Non-Crystalline Solids* **2015**, *416*, 21.

Chapter 2

Literature Review

Chapitre 2

Étude Bibliographique

Résumé : Ce chapitre se focalise sur l’état de l’art autour de la problématique considérée. Nous présentons d'abord certaines réactions d’oxydo-réduction éventuellement présentes au cours de la vitrification et la production d’oxygène moléculaire qui en découle. Une fois formé, ce gaz est physiquement dissous dans la structure vitreuse fondue jusqu'à atteindre la limite de solubilité et au-delà, des bulles peuvent être nucléées. Aussi, une seconde partie est dédiée aux phénomènes de saturation et sursaturation gazeuses ainsi qu’aux différents types de nucléation et les lois les régissant. Après avoir été nucléées, les bulles évolueront dans la fonte. Par conséquent, le troisième et dernier point examiné concerne les mécanismes de croissance. Nous décrivons ici le transfert de masse, les lois qui le régissent et deux modèles utilisés dans la littérature. En plus du transfert de masse, une brève description de la coalescence et du mûrissement d'Ostwald est réalisée.

Chapter 2

Literature Review

In the introduction chapter, we mentioned that there is a hiatus of information in the literature in terms of redox reactions and O_2 bubble formation in glass melts. Therefore, in this literature review, we firstly expose some redox reactions possibly present in nuclear glass melts and molecular oxygen produced by them. Once O_2 is formed, it is physically solubilized in the melt structure until reaching the saturation threshold and beyond this point, bubbles may be nucleated. Different nucleation types may be observed depending on melt conditions and on the supersaturation of the present gases. Thus, the second approached point of this chapter is the different nucleation types and features of them. After being nucleated, bubbles will evolve in the melt. Therefore, the third and last reviewed point is the growth mechanisms. We describe herein mass transfer and its governing laws as well as a brief description of coalescence and Ostwald ripening.

Besides being important to help defining the simplified glass melt system, this bibliographic report supports the fundamental comprehension of O_2 bubble formation. Firstly, by understanding the thermodynamics of the system one can predict the oxygen gas concentration and tendencies of the system, in terms of nucleation and grow. Knowing the nucleation type one can understand different features and characteristics of the bubbled-melt, such as initial position of the formed bubbles and their size distribution can be also probed. Moreover, by studying the growth mechanisms present in the system, we can identify the major growth contributor and we will be able to make predictions about bubble and melt features over time. In terms of growth mechanism, knowing them well, one can develop mathematical models to forecast bubble(s) behavior over time.

2.1 Redox reactions in oxide melts

Redox state control is one of the keys for ruling several features in glass science. It is well known that most of the coloring species are multivalent elements and that the final color of the glass is determined by the position of the redox equilibrium.[1] These elements have been vastly used to enhance electrical conductivity and chemical durability of phosphate glasses.[2-4] In industrial glass melting tanks, chemical agents, which are oxide of polyvalent ions, are vastly used to enhance the so-called fining process.[5,6] Likewise, in the context of nuclear waste vitrification, redox control might be advantageous to increase the amount of final waste incorporated into the glass as well as to increase the solubility of certain species.[7,8] Besides, different studies have been carried out on redox influence on bubble behavior in glass melts, including its influence on mass transfer phenomenon.[9-12] Therefore, in this section we go through the redox phenomenon description, presenting the general equations and concepts. Afterward, we present the parameters which affect the redox equilibrium position. Finally, we present some key multivalent elements in nuclear waste vitrification context which might influence bubble formation and behavior in glass melt.

2.1.1 Redox phenomenon – general approach

Redox reactions are characterized by electron transfer between two different species of a given multivalent element, *e.g.* $\mathrm{Ce(IV)}$ and $\mathrm{Ce(III)}$. These species are called redox couple. The reaction involving them along with the concerned electrons is called half-reaction. While in oxidation reactions, the multivalent element loses electrons, in reduction reactions, this element gains. Eq. (2.1) and (2.2) display two half-equations of two general redox couples ($\mathrm{Ox_1/Red_1}$ and $\mathrm{Ox_2/Red_2}$). Eq. (2.3) represents the final redox equation.

$$\mathrm{Red_1} \rightarrow \mathrm{Ox_1} + \mathrm{ne^-}, \tag{2.1}$$

$$\mathrm{Ox_2} + \mathrm{ne^-} \rightarrow \mathrm{Red_2}, \tag{2.2}$$

$$\mathrm{Red_1} + \mathrm{Ox_2} \rightleftarrows \mathrm{Red_2} + \mathrm{Ox_1}. \tag{2.3}$$

In molten oxide glasses, $\mathrm{O_{2(g)}/O^{2-}}$ redox couple is involved in redox reactions. $\mathrm{O_{2(g)}}$ is the physically dissolved oxygen, while $\mathrm{O^{2-}}$ is the oxygen ion. This is also chosen as the reference redox couple for this type of liquid. Thus, its standard potential value, at 1 atm of pressure, is set as zero ($\mathrm{E_{O_{2(g)}/O^{2-}} = 0\,V}$). This half-reaction is presented in Eq. (2.4). Finally, a general redox equation for $\mathrm{M^{m+}/M^{(m-n)+}}$ redox couple in an oxide glass melt is displayed in Eq. (2.5).

$$\mathrm{2O^{2-}} \rightarrow \mathrm{O_{2(g)}} + \mathrm{4e^-}, \tag{2.4}$$

$$\mathrm{M^{m+}} + \frac{\mathrm{n}}{2}\mathrm{O^{2-}} \rightleftarrows \mathrm{M^{(m-n)+}} + \frac{\mathrm{n}}{4}\mathrm{O_{2(g)}}. \tag{2.5}$$

Eq. (2.6) presents the equilibrium constant for a general redox couple $\mathrm{M^{m+}/M^{(m-n)+}}$ in an oxide molten glass.

$$\mathrm{K(T)} = \frac{\mathrm{a_{M^{(m-n)+}}\,.\,a_{O_2}^{n/4}}}{\mathrm{a_{M^{m+}}\,.\,a_{O^{2-}}^{n/2}}}, \tag{2.6}$$

where $\mathrm{a_x^y}$ is the activity of the species x to the power of its stochiometric coefficients.

The activity of each of these species is equal to the activity coefficient (γ') times the respectively molar concentration. For molecular oxygen, its activity can be considered as its fugacity (f_{O_2}). Indeed, the amount of oxygen available to react with elements in a molten glass can be conveniently described by the oxygen fugacity.[13,14] Therefore, the equilibrium constant might be re-written as:

$$K'(T) = \frac{\gamma'_{M^{(m-n)+}} \left[M^{(m-n)+}\right] . f_{O_2}^{\frac{n}{4}}}{\gamma'_{M^{m+}} \left[M^{m+}\right] . a_{O^{2-}}^{n/2}}. \tag{2.7}$$

The ratio of the ions' activity coefficient is constant for any temperature and ion concentrations.[15] The activity coefficient of the oxygen ions ($a_{O^{2-}}$) is function of the glass optical basicity (Λ) and it is described afterward. Thus, the equilibrium constant of each of these species can be related to two thermodynamic entities as follows:

$$\frac{\left[M^{(m-n)+}\right] f_{O_2}^{1/4}}{\left[M^{m+}\right]} = \exp\left(-\frac{\Delta H_0 - T\Delta S_0}{RT}\right), \tag{2.8}$$

where ΔH_0, ΔS_0 are, respectively, the enthalpy and entropy of the species in the molten glass and R is the ideal gas constant. Therefore, knowing these two thermodynamic entities, one can relate the speciation of a given multivalent element to the oxygen fugacity. Some authors have investigated this type of equilibrium for some redox couples and thermodynamic models to reach multivalent speciation, in terms of oxygen fugacity, temperature and optical basicity, have been presented.[16-18]

2.1.2 Parameters influencing redox equilibrium

The redox equilibrium described by Eq. (2.8) is influenced by different parameters. In this section we present and define these parameters and also describe how they affect the equilibrium previously mentioned.

- Oxygen fugacity: ($f_{O_2}\uparrow$, $\mathrm{red/ox}\downarrow$)

As mentioned, oxygen fugacity can be understood as the amount of oxygen available to react with elements in a molten glass.[14,19] In ideal gas systems, oxygen fugacity can be considered as oxygen partial pressure and therefore it is linked to oxygen concentration by Henry's law. Schreiber *et al.*[20] verified that the plot $\log(\mathrm{red/ox})$ versus $\log(f_{O_2})$ has, generally, a straight line with slope equals to $\frac{n}{4}$, in which n is the number of exchanged electrons. Thus, one can observe that, generally, when oxygen fugacity increases, the amount of oxidized species also does following the mentioned slope. This relationship is observed for a fixed temperature and composition. This behavior has also been observed experimentally for cerium oxide.[16] For large total iron content, this observed behavior is still valid, meaning that increasing f_{O_2}, oxidized species are formed, but the slope in this latter situation is generally lower than 0.25.[18,19]

- Temperature: $(T\uparrow, \mathrm{red/ox}\uparrow)$

Temperature effect on redox equilibrium cannot be verified just by observing the redox equation. Experimentally,[21,22] it has been observed that higher temperatures shift the equilibrium favoring reduced states and consequently O_2 formation. This is explained by equilibrium law perturbation, since for most of the redox pairs, Eq. (2.5) is endothermic $(\Delta H_0 > 0)$. As mentioned in the introduction, the current studied borosilicate glass system is doped with cerium and this polyvalent element has also a similar behavior in terms of temperature as state herein.[16]

- Glass optical basicity: $(\Lambda\uparrow, \mathrm{red/ox}\downarrow)$

The term “basicity” is open to several interpretations. In glass science, it is defined as the “state” of oxygen ions and how they would react with their surrenders. The oxygen ability in donating negative charge is at a maximum when there is free O^{2-}. Thus, basicity, for glasses, is completely related to the oxygen ion activity $(a_{O^{2-}})$ in the melt. Basicity is complicated to measure in glasses and due to this, usually glass scientists use the concept of optical basicity (Λ) proposed by Duffy and Ingram in 1976.[23] **Table 2.1** displays some values of optical basicity found by Duffy and Ingram,[24] and it is usually calculated by considering the molar fraction of each oxide. Optical basicity values are based on optical absorption of probe ions such as Tl^{+}, Pb^{2+} and Bi^{3+}. This absorption is observed at ultra-violet region and the peak position is very sensitive to the O^{2-} polarisation level and consequently to the glass composition as well. Since possible modifications in the outer shell cause change in energy of core orbital electrons, this allows X-ray photoelectron spectroscopy (XPS) to be used as a technique to evaluate optical basicity in glasses. For most of the redox pairs, increasing glass optical basicity, the redox equilibrium shifts towards the oxidized species.[16,17,25] Some exceptions have been found, such as Cu^{2+}/Cu^{0}.[25]

Table 2.1: Optical basicity for main oxides studied in glass science.[24]

Oxide	Optical Basicity (Λ)
B_2O_3	0.42
SiO_2	0.48
Al_2O_3	0.60
MgO	0.78
ZnO	0.95
Li_2O	1.00
CaO	1.00
Na_2O	1.15

- Glass composition

Besides affecting glass basicity, glass composition may also influence the activity coefficient (γ') and solvation. Both of them play a role in redox equilibria. Solvation, may influence the enthalpy and entropy, since it is related to the local environment of the multivalent element.

2.1.3 Redox study of some key elements

In the context of nuclear waste vitrification, we describe herein some key elements linked to O_2 bubble formation. The choice of these elements is based on the abundance in the waste types as well as their redox power and solubility.[8,26] Hence, we present in this section cerium and iron.

I. Cerium (Ce)

In glasses, cerium may be present either as $\mathrm{Ce(IV)}$ or $\mathrm{Ce(III)}$.[7,16] Cerium presents elevated equilibrium constant values for lower temperatures and due to this, its reduction and consequently O_2 production may take place easier than for other elements.

Pinet *et al.*[16] developed a model to determine cerium speciation in different molten glasses. It was established by electrochemical measurements of four different glass compositions. This model takes into consideration temperature (T), optical basicity (Λ) and oxygen fugacity (f_{O_2}). The model is proposed for temperature range coming from 905 to 1250 °C. In terms of optical basicity, the model is proposed from 0.52 and 0.65, covering then, most of the nuclear waste glasses. The obtained equation is displayed in Eq. (2.9) and covers a wide range of nuclear waste melts.

$$\log\left(\frac{Ce^{3+}}{Ce^{4+}}\right) = 4.319 - \frac{3328}{T} - 3.631.\,\Lambda - \frac{1}{4}\log(f_{O_2}). \tag{2.9}$$

This last equation allows us to see that more reduced species increases with increasing temperature or with decreasing optical basicity and oxygen fugacity.

Figure 2.1, obtained from the aforementioned model, shows cerium-(III) over cerium total fraction evolution with temperatures ranging from 700 to 1400 °C. It gives an idea of the evolution of cerium speciation with temperature. This graph is built for a fixed oxygen fugacity (0.21 atm) basicity ($\Lambda = 0.53$).

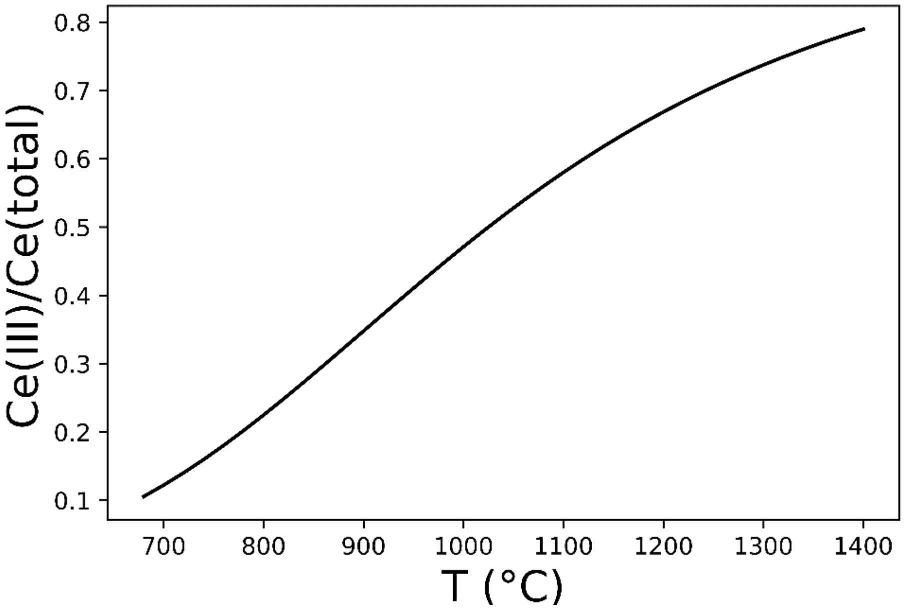

Figure 2.1: Cerium reduction fraction as function of temperature in the studied glass melt for a constant oxygen fugacity of 0.21 atm according to Pinet *et al.*[16]

II. Iron (Fe)

In nuclear waste conditioning context, iron may come from waste.[8,26] In some cases, iron may be also used to adjust the redox of some glass compositions. Additionally, in terms of bubble nucleation, this multivalent element is important since it may be present in an elevated amount in the final glass, being able then to affect O_2 production. In conventional glass industry, glasses doped with iron have been investigated.[10-12]

As well as cerium, the redox ratio of iron is determined by temperature, oxygen fugacity and melt composition. Le Losq *et al.*[19] also underlined the influence of total iron concentration on its speciation. Kress and Carmichael[18] developed a model that allows Fe-redox equilibrium calculation in natural silicate melts as function of these mentioned entities. These data have been proven to represent accurately iron-redox equilibrium in both natural and synthetic glass compositions. They proposed a model for different compositions, but in this bibliographic report we focus on a composition in the $CaO - Al_2O_3 - Fe_2O_3 - FeO - SiO_2$ glass system (CAFS). Their model was proposed ranging between 945 and 1530 °C. Eq. (2.10) presents the model for Fe redox pair as function of the oxygen fugacity, temperature and the molar fraction of each oxide (X_i). **Table 2.2** presents the values for each coefficient (K_i) for CAFS glass system.

$$\ln\left(\frac{X_{Fe_2O_3}}{X_{FeO}}\right) = 0.207.\ln\left(f_{O_2}\right) + \frac{12980\ (K)}{T} - 6.115 + \sum_i K_i X_i. \tag{2.10}$$

Table 2.2: Parameters for Eq. (2.10) for CAFS glass system.

Coefficient	CAFS	Units
$KSiO_2$	-2.368	-
KAl_2O_3	-1.622	-
KCaO	2.073	-

Eq. (2.10) establishes a relationship between iron redox ratio and oxygen fugacity. It can be observed that the slopes for this equation, considering f_{O_2} as independent variable, is different from the supposed value discussed in the section 2.1.2. This value was supposed to be $1/4$. When glasses are doped with large amounts of iron (up to around 25 wt% in that study), structural changes happen and it may affect optical basicity and activity coefficient. De Best,[15] in her PhD manuscript, discussed the effect of total concentration of a polyvalent element on the redox ratio. For soda-lime-silica and alkali disilicate melts, an increase of total iron content favors oxidized states. Reasoning in the same way, Le Losq *et al.*[19] stated the same for volcanic glasses and melts doped with iron.

2.1.4 Conclusion

In this section, we presented redox definition and some governing equations applied to glass science. Besides, it was also discussed the main parameters which may affect redox equilibrium in molten glasses and the main important polyvalent elements for the researched system. This section supports the understanding of multivalent elements in glass melts and it orientates the choice of the simplified glass system of this PhD work.

2.2 Bubble Nucleation

As mentioned, molecular oxygen is the main considered gas due to the presence of multivalent elements. Thus, after understanding redox reactions, and how these reactions influence molecular oxygen production, gas nucleation is presented. After being produced, molecular oxygen is physically dissolved[27] until it reaches a certain level of supersaturation, in which bubbles nucleate.[27]

Bubble nucleation has been studied in general glass melts[28] as well as in other research fields, such as geological melts,[29-32] beverages liquids[33] and even nitrogen bubbles which might be nucleated in divers' blood while surfacing due to external pressure release.[34]

Bubbles may be formed in three ways:[35]

- Cavitation,
- Boiling,
- Gas desorption.

Firstly, reducing external pressure below the vapor pressure of the pure liquid can cause bubble formation by cavitation. Secondly, increasing the temperature above the vapor temperature may cause boiling. Finally, when a gas is dissolved in a liquid and the system conditions are changed in a way to reach supersaturation conditions, gas bubble may be formed. This last type of bubble nucleation is the one studied in our investigated case, since there are dissolved gases in the glass melt. Somehow changing the synthesis and melt conditions, bubbles might be formed. Still considering this latter type of nucleation, gas supersaturation level is extremely important. Due to this, a section about saturation and supersaturation is dedicated herein. Besides this section, we go through the four nucleation types described in the literature.

2.1.1 Saturation ratio and Supersaturation

Gas supersaturation is used to quantify the tendency of a system to produce bubbles. As illustration, we use previous data from the literature[36] displaying the saturation threshold for dissolved CO_2 in water at 1.013×10^5 Pa (**Figure 2.2**).

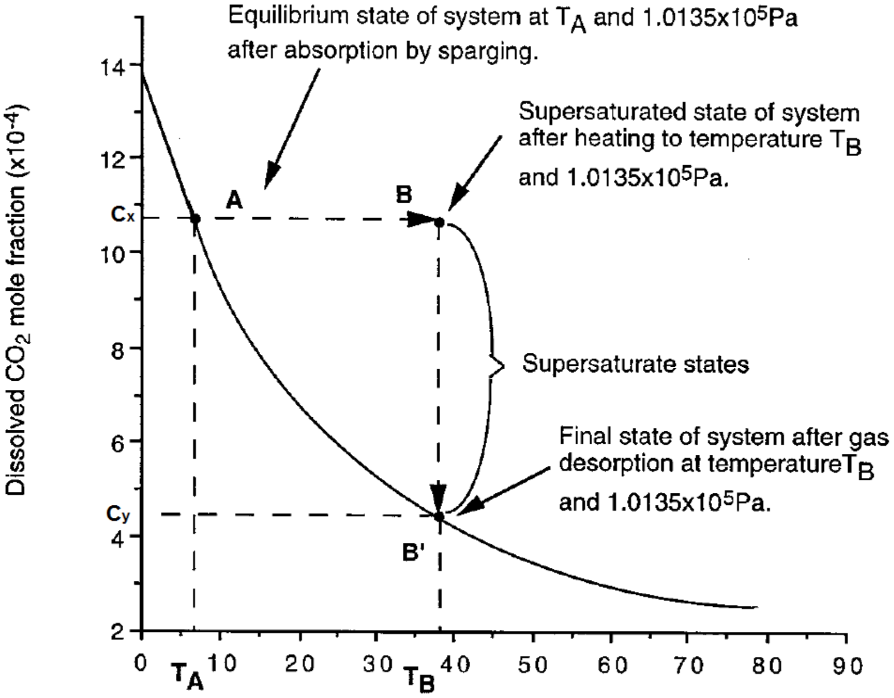

Figure 2.2: CO_2 solubility in water as function of the temperature at 1.013 x 10^5 Pa.[36]

In this system, when temperature rises, gas solubility is decreased following the tendency displayed in **Figure 2.2**. Point A represents a saturate solution for a given temperature ($\mathrm{T_A}$). If the temperature increases to $\mathrm{T_B}$, the amount of dissolved gas will be the same, but its solubility will decrease. The difference between the current concentration (C^x) and the solubility of the system in new temperature $\mathrm{T_B}$ (C^y) is considered the supersaturation of the system. It is displayed in **Figure 2.2** as "supersaturate states". Saturation ratio (Sa – Eq. 2.11) and supersaturation (S – Eq. 2.12) are defined as:

$$\mathrm{Sa} = \left(\frac{\mathrm{C}^x}{\mathrm{C}^y}\right)^{\beta \mathrm{i}}, \tag{2.11}$$

$$\mathrm{S} = \mathrm{Sa} - 1. \tag{2.12}$$

Eq. (2.13) presents Henry's law.

$$\mathrm{C_i} = \mathrm{L_i}.\mathrm{P_i}^{\beta \mathrm{i}}, \tag{2.13}$$

where $\mathrm{C_i}$ $(\mathrm{mol.m^{-3}})$, $\mathrm{L_i}$ $(\mathrm{mol.m^{-3}Pa^{-\beta i}})$, and $\mathrm{P_i}$ (Pa) are respectively the gas concentration, the Henry constant and the partial pressure for the dissolved gas i. The exponent β_{i} depends on the nature of gas solubilization. For instance, for the water vapor, this exponent is ½, while for most of the other gases, it is equal to 1. Considering these three previous equations along with no water in the system, the supersaturation pressure difference (ΔP_S) between the system at a current situation (P^x, C^x) and at its solubility situation (P^y, C^y) can be written as function of its supersaturation (S), as displayed in Eq. (2.14):

$$\Delta P_S = P^x - P^y = \frac{1}{L}(C^x - C^y) = P^y\left(\frac{C^x}{C^y} - 1\right) = P^y.S. \tag{2.14}$$

Thus, it can be observed that supersaturation (S) is linearly correlated to the pressure difference and both of them are related to the driving force for bubble nucleation. It is better explained latter in this section.

Boloré and Pigeonneau[37] studied, numerically, (**Figure 2.3**) the saturation ratio dependence with temperature for several gas species in a given float glass (molten). Their behaviors were obtained for a given the glass melt composition and redox state. It is important to stress that their system is different from the current studied system. In their system, reaction involving sulfur gives rise to SO_2 production when temperature is risen. On the other hand, for our investigated system, O_2 is the gas that is produced when temperature rises.

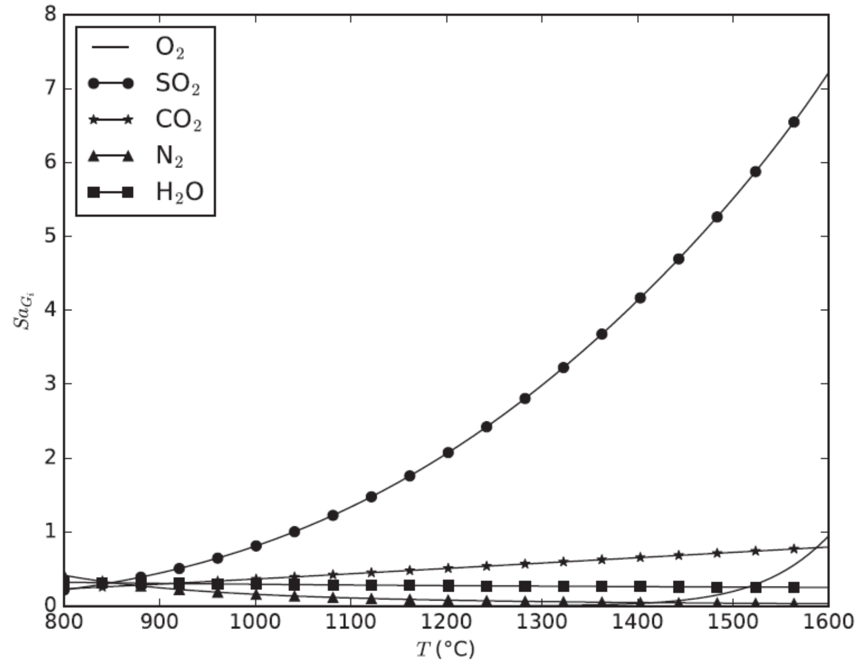

Figure 2.3: Saturation (Sa) for different gases as function of temperature. They were numerically obtained considering glass composition and redox.[37]

2.1.2 Nucleation theory applied to bubbles

Four possible types of nucleation are described in the literature (types I, II, III and IV).[27] The main practical difference between them is the level of supersaturation required to nucleate a bubble. The two first ones are based on the well-known classical nucleation theory (CNT) and the two other ones are non-classical models. This section is dedicated to present them, give an explanation about their theory and present some practical examples.

I. Nucleation type I: Classical homogeneous nucleation

Gibbs followed by Volmer and Weber[38] have begun to study nucleation theory in the last century and their theories are the bases of different theories nowadays. The four main bubble nucleation theories might be considered as particular variations of the classical homogeneous nucleation theory, which supposes the same nucleation probability in any given part of the system.[38]

In this theory, it is considered that nucleation takes place when a molecule or atom cluster pops up and its existence is governed by the aggregation or desegregation of new particles to the previously formed cluster. What will decide the cluster's future is the energy balance between bulk free energy per unit of volume and the surface energy between this new phase and the surrounding matrix. The new gas phase has lower bulk free energy per unit of volume than the supersaturated melt, which gives a negative ΔG_V and consequently is considered the driving force for nucleation. However, the creation of new bubbles results in the production of an interfacial free energy, which does not favor thermodynamically the system to keep nucleating. Considering spherical clusters, Eq. (2.15) describes the aforementioned energy balance.

$$\Delta G = \frac{4\pi}{3} a^3 \Delta G_v + 4\pi a^2 \sigma, \tag{2.15}$$

where ΔG is the total Gibbs free energy of the system, a is the cluster radius, ΔG_V is the Gibbs free energy difference between the supersaturate bulk and the new gas phase and σ is the surface tension. Considering the antagonism of the two last terms, an extremum point is presented in the plot ΔG vs a (**Figure 2.4**). Deriving Eq. (2.15), this required total Gibbs free energy, also called critical free energy for homogeneous nucleation (ΔG_{homo}– Eq. 2.16) and the critical radius (a_c – Eq. 2.17) for nucleation can be calculated. ΔG_V for bubble nucleation is equal to the supersaturation pressure difference (ΔP_s), which in fact is the driving force for nucleation. It is interesting to note that the critical radius does not depend on the type of nucleation and it is always expressed by Eq. (2.17).[39]

$$\Delta G_{homo} = \frac{16\pi\ \sigma^3}{3\Delta P_s^2}, \tag{2.16}$$

$$a_c = \frac{2\,\sigma}{\Delta P_s}. \tag{2.17}$$

Figure 2.4 illustrates the aforementioned energy balance related to nucleation. The critical free energy and the critical radius are pointed out. It is interesting to note that when dissolving other gases in the system, the supersaturation pressure difference (ΔP_s), in the Eq. (2.14), rises and consequently, the critical free energy for nucleating a bubble ($\Delta G_{\mathbf{homo}}$) is decreased as shown in Eq. (2.16). Therefore, dissolving different gases in a glass melt, bubble nucleation takes place more easily.

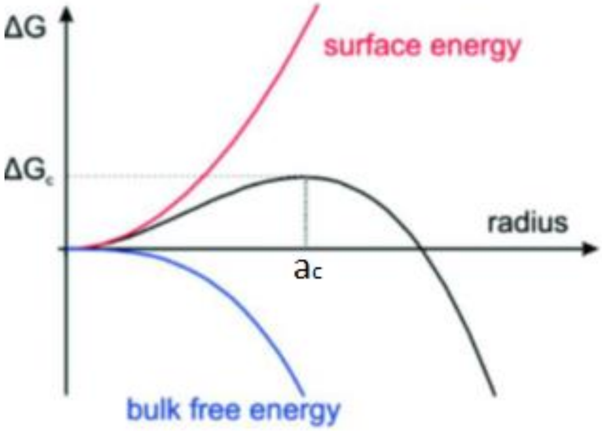

Figure 2.4: Energy balance versus radius development for nucleation.

In the previous case, in which there are more than one dissolved gas, the critical radius to form a nucleus may be calculated using Laplace's relation. Indeed, the basic concept is the same. Laplace's pressure is the pressure within a bubble that exceeds the liquid pressure on its surroundings.

$$a_c = \frac{2\,\sigma}{\left(\sum_{i=1}^{N_g} Sa_i^{\frac{1}{\beta_i}} - 1\right) P_L}, \tag{2.18}$$

where N_g is the number of dissolved species in the molten glass and P_L the pressure around the bubble in the liquid.

Classical homogeneous nucleation requires extremely high supersaturation levels to take place. It was stated by some authors, that this level might be about a hundred times or even higher than the saturated situation.[27,40] Due to this, once the system reaches this supersaturation level, too much gas is dissolved and the bubbles nucleate is an essentially explosive way.[40] This elevated supersaturation level is explained because the newly formed gas phase must tear apart the liquid and thus, overcome its enormous cohesive/tensile strength. This theory also considers that nucleation does not come from a previous gas cavity. These cavities may be also called pre-existing bubbles or even Harley nuclei.[41] They may facilitate future bubble nucleation. It is better discussed in the following sections.

Classical homogeneous nucleation was recognized in some systems under extremely care. Mourada-Bonnefoi and Laporte[30] observed this type of nucleation mechanism for a specific scenario where $\mathrm{CO_2}$ and $\mathrm{H_2O}$ bubbles were homogenously nucleated in rheolytic melts. Moreover, in terms of crystal nucleation, Zanotto and James[42] stated, for two oxide glasses, that the temperature dependence of nucleation rates was satisfactorily described by the classical nucleation theory. Besides, Hemmingsen,[43] taking extreme care to eliminate any gas cavities from his system, showed that bubble nucleation in glass capillaries required extremely high supersaturation level, as the nucleation type I states. Due to the extremely high required supersaturation for homogeneous nucleation, along with the difficulty to eliminate external subtracts and gas cavities, this type of nucleation is less likely to happen in laboratory tests.

II. Nucleation type II: Classical heterogeneous nucleation

In this current case, nucleation occurs on an external subtract that may be impurities, insoluble crystals, crucible wall or any other external surface. Just as nucleation type I, classical heterogeneous nucleation also considers no previous gas cavities in the bulk. Due to the aforementioned external surface used as nucleation site, the energy balance between nucleation driving force ($\Delta\mathrm{G_V}$) and surface energy is modified. In fact, this new term depends on the wettability of the gas on the substrate. This wettability is related to the so-called contact angle (**Figure 2.5**).

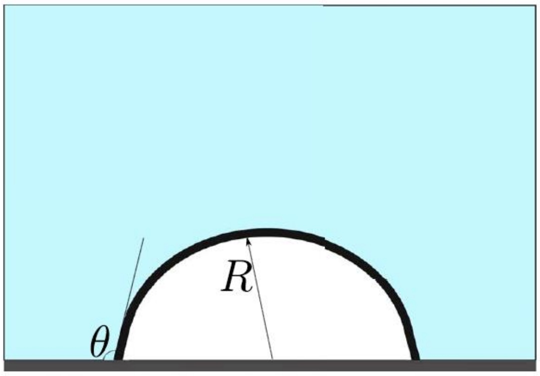

Figure 2.5: Contact angle (θ) during heterogeneous nucleation.

Contact angle (θ) depends on the nature of the involved entities: the gas, the glass melt and the substrate. After considering this interaction, a new term is added to Eq. (2.16). It was stated by Hurwitz and Navon[29] that not only the wetting angle of the crystal but also the crystal morphology is a critical parameter in determining the crystal efficiency as nucleating sites.

$$\Delta G_{\mathrm{hetero}} = \frac{16\pi\ \sigma^3}{3\Delta G_v^2}\frac{2+3\cos(\theta)-\cos^3(\theta)}{4}. \tag{2.19}$$

Considering the new surface for nucleation, when compared to the one from type I, the energy barrier decreases and consequently the required supersaturation level also does. Therefore, heterogeneously nucleated bubble takes place at lower temperature but it may be violent nevertheless.[40] It is interesting to emphasize that the level of supersaturation for nucleation type II is still considered high when compared to type III and IV.

In order to illustrate the energy barrier difference, we present in **Figure 2.6** a comparison between the nucleation energy barrier ratio for heterogeneous and homogeneous nucleation for varying contact angle.

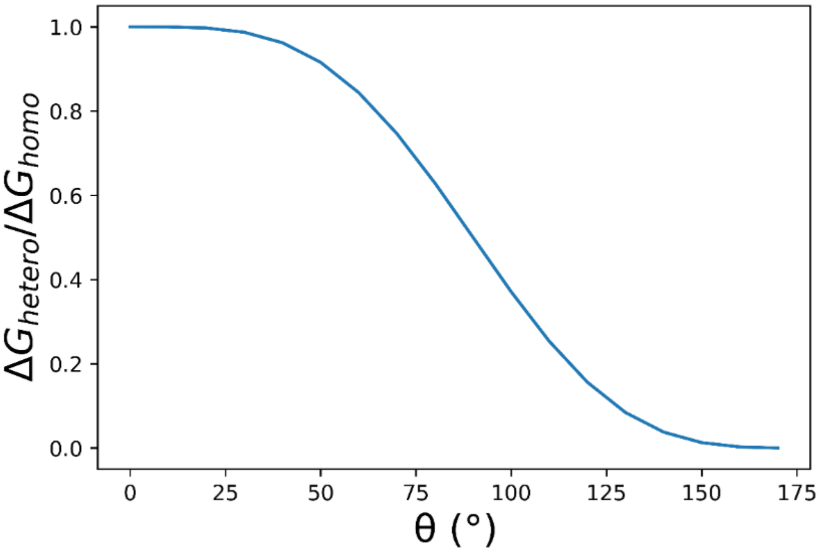

Figure 2.6: Comparison of the nucleation barrier ratio between heterogeneous and homogeneous nucleation for varying contact angle in degrees.

Figure 2.7 illustrates the energy balance of nucleation type I compared to type II. The energy barrier is decreased but the critical radii, in both cases, are the same.

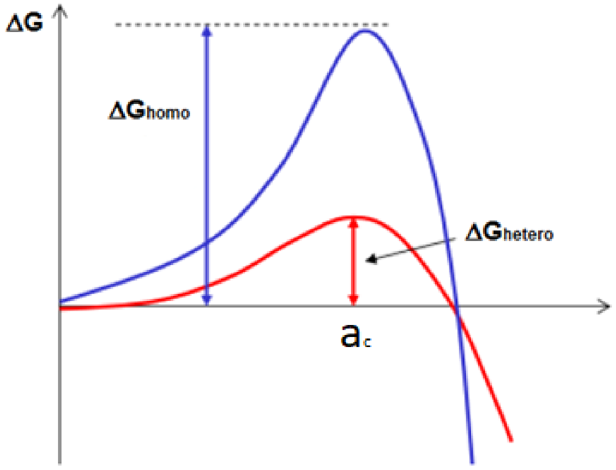

Figure 2.7: Homogeneous (type I) and heterogeneous (type II) critical energy for bubble nucleation.

It is important to highlight that the first nucleation event, when an external substrate is present is considered as type II. However, after this first event, the bubble nucleation rate drops significantly. It happens because the level of supersaturation decreases after the first nucleation event. Therefore, the following nucleation events might follow type III and IV,[27] which are presented in the following sections.

Classical heterogeneous nucleation has been recognized in different systems, such as magmas with insoluble crystals.[29,32] There are different sparingly soluble elements in the nuclear waste vitrification processes, they may work as a substrate for heterogeneous nucleation.[17,44] Thus, this is another similarity between nuclear waste glass melt and geological melts.

Jones *et al.*[27] have shown in their work an interesting scheme about nucleation type I and II. **Figure 2.8** presents nucleation type I, producing gas bubble in the bulk at high levels of supersaturation. On the bottom of this image, it is displayed nucleation type II, catalyzed by the presence of an insoluble particle in the liquid as well as by the crucible wall. As mentioned in the previous sections, nucleation type II takes place at lower supersaturation level.

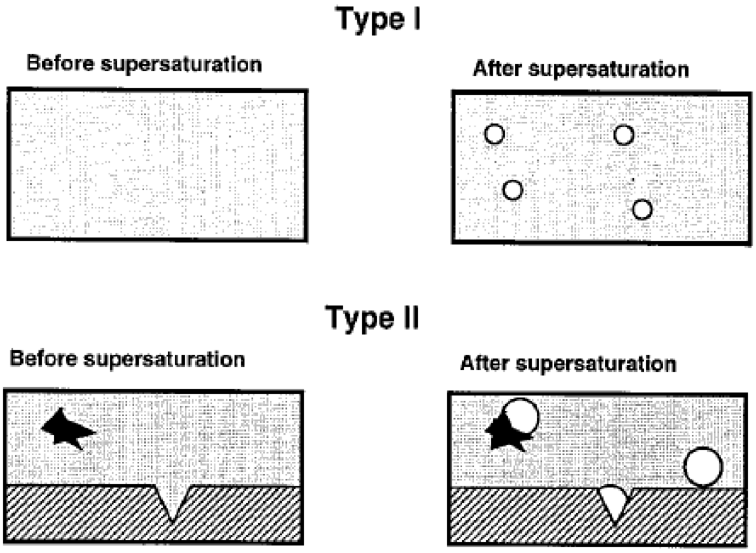

Figure 2.8: Scheme illustrating nucleation types I and II.[27]

Concerning industrial glasses, there are much less publications when compared to carbonated beverage. The team from Prague, headed by Jaroslav Kloužek, has published interesting articles about bubble nucleation in that field. Recently, they published an article (Vernerová *et al.*[28]) investigating bubble nucleation on a platinum wire in glass melts at high temperature – around 1500 °C (**Figure 2.9**). They varied temperature and SO_3 content in the melt to observe nucleation modifications. This investigation has been carried out using a special furnace coupled with a window that allows *in-situ* camera visualization. This equipment is used in this PhD work and, as mentioned in the introduction chapter (section 1.4), it requires light transmission through the glass, then limiting the composition in terms of coloring elements.

Vernerová *et al.*[28] found, for this heterogeneous bubble situation, a required supersaturation of 1.47. This is lower when compared to the ones from other fields, such as carbonated drinks and magmas.[30,31,45]

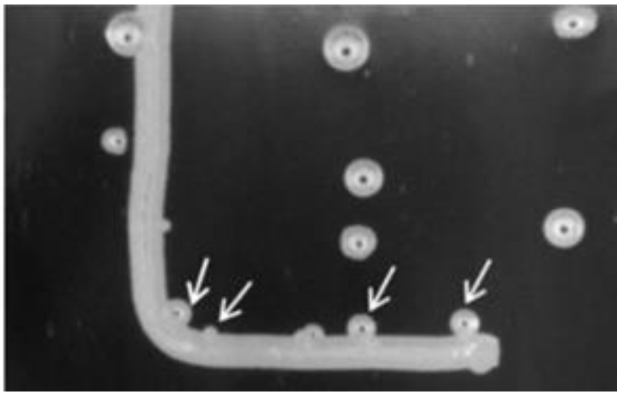

Figure 2.9: A typical observed image of bubble nucleation over Pt wire. Just the bubbles nucleated on the horizontal part were investigated.[28]

III. Nucleation type III: Pseudo-classical nucleation

Type III or pseudo-classical nucleation uses pre-existing gas bubbles, which have radii smaller than the critical radius predicted by the classical nucleation theory. At the moment the system is made supersaturated, the radius of curvature of each meniscus is lower than the critical radius. Thus, the system has to overcome a finite nucleation energy barrier. Consequently, pseudo-classical nucleation is achievable at lower supersaturation levels. Therefore, nucleation type III nucleates less violently than types I and II.[27,39] This current nucleation includes homogeneous and heterogeneous nucleation at pre-existing gas cavities at difference places. It may take place at the external surface of the crucible, at the surface of insoluble particles and at metastable micro-bubbles in the bulk solution.

Once it still depends on supersaturation level, gas cavities smaller than the critical radius ($a < a_c$) may or may not grow, depending on the local supersaturation fluctuations. Larger gas cavities demand lower supersaturation levels to nucleate and vice-versa. Due to the lower supersaturation, several bubble features are different from the ones nucleated by nucleation types I and II. **Figure 2.10** presents bubble nucleation following the three types already presented in this document. It can be seen that the higher is the required supersaturation (*e.g.* type I), the more intense and violent the nucleation will be. Consequently, bubbles will present narrower size distribution because they were nucleated at the same time. Considering the same point of view, bubbles nucleated by type III mechanism present lower maximum nucleation rate, but it lasts longer, giving rise then to a less violent nucleation and a broader size distribution.

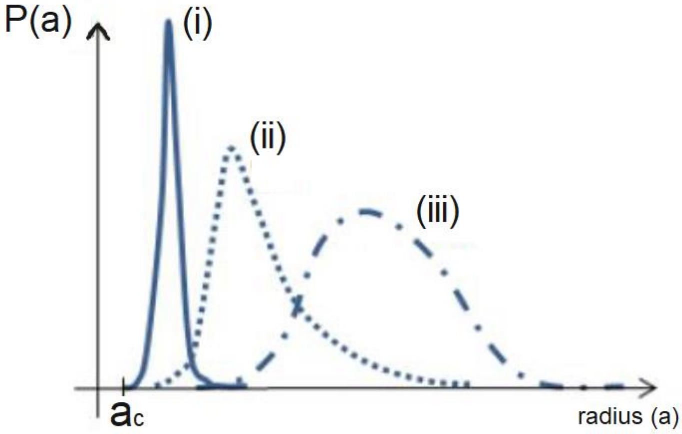

Figure 2.10: Bubble size distribution for nucleation models type I, II and III.[46]

An interesting experiment carried out by Dean,[47] in which solid glass pieces were broken in two different scenarios: in air and inside the supersaturated liquid. He concluded that the external glass particles broken in air have brought gases that worked as pre-existing bubbles, favoring then nucleation type III to take place. On the other hand, the glass particles broken inside the supersaturated liquid do not result in a source for nucleation.

Bolоré and Pigeonneau[37] have studied re-melted float glass in two different situations, one in contact with atmosphere and the other one with tin. They have argued that in their studied system, bubble nucleation follows type III as well. It is also concluded that pre-existing heterogeneities or pre-existing bubbles should be present at the interface between the molten glass and the crucible. It is important to state that, for their case, they stated that experimental proof of the existing cavities remains to be proven.

IV. Nucleation type IV: Non-classical nucleation

Like pseudo-nucleation theory, non-classical nucleation theory also considers that bubbles nucleate from pre-existing bubbles. On the other hand, in order to follow this latter theory, gas cavities radii must be larger than the critical radius predicted by CNT ($\mathrm{a} > \mathrm{a_c}$). Therefore, this nucleation is considered non-classical because there are no nucleation energy barriers to overcome.[39,48] Non-classical nucleation occurs at pre-existing gas cavities on the surface of the container or elsewhere in the liquid bulk. It may also come following nucleation type II and type III.

As nucleation type IV does not require an energy barrier,[39,48,49] bubbles will directly grow by diffusion of gas from the bulk liquid to the bubbles, based on mass transfer. Other growth mechanisms such as coalescence or Ostwald ripening might be observed as well.

In terms of supersaturation, nucleation type IV requires very low supersaturation levels to take place.[39] Consequently, this type of nucleation, generally, does not happen in a suddenly way, as types I and II. Therefore, nucleation type IV takes place more quietly and consequently it is less hazardous.

Shelby[5] mentioned in his book a type of bubble formation in which bubbles are also formed in a non-classical way. Granular glass medium when introduced into a heated furnace is submitted to a strong surface heating which causes fusion of glass layer on the surface. During this rapid fusion, portion of air, which initially occupies the spaces between glass particles, are entrapped and they give rise to bubbles. The rapid heating of such a melt can lead to expansion of these bubbles and foaming can occur. Bubbles formed by this process, generally, have size distribution imposed by the pre-melted glass grains.[50]

If we consider that the heat flux when the glass medium is introduced in the furnace is due to radiative transfer, the thickness (δ) over which the granular media is initially heated can be determined by the following equation:

$$\delta \simeq \frac{\lambda}{\epsilon(\sigma_{SB})(T_w^2 + T^2)(T_w + T)}, \tag{2.20}$$

where λ is the thermal conductivity of the granular glass medium ($\lambda = 0.25\frac{W}{m.K}$),[51] ϵ is the effective emissivity ($\epsilon \sim 1$), σ_{SB} is the Stefan-Boltzmann constant ($5.670374419 \ldots 10^{-8} \frac{W}{m^2K^4}$), T_w the wall temperature of the furnace in K and T the initial temperature of the granular medium, also in K. The scaling given by Eq. (2.20) results to the balance of the thermal flux in the granular media with the radioactive flux. The time to melt the granular medium over the aforementioned thickness δ is given by the following:

$$t \simeq \frac{(\rho_{gran})C_p\,\delta^2}{\lambda}, \tag{2.21}$$

where ρ_{gran} the effectivity density ($\rho \sim 1250\frac{Kg}{m^3}$) and C_p the effective heat capacity of the granular medium ($C_p = 1100\frac{J}{Kg.K}$). Hence, for granular glass systems this calculated melting time for a thickness of some millimeters is about some tens of seconds.

Nucleation type IV was evidenced in different systems. Effervescence in carbonated beverages is an awesome and a common example of bubble formation from pre-existing gas cavities. Liger-Belair *et al.*[49,52] present bubble nucleation in champagnes and use this system to illustrate and better understand bubble nucleation of type IV. In this previous system, when a bottle is opened, due to instantaneous pressure release, bubbles are nucleated. When poured in a glass, these nucleated bubbles fill the gas cavities, which in this case are mainly cellulose fibers coming from air surrounding the champagne glass. It is charming how these bubbles are nucleated from these cavities creating then the so-called, bubble train (**Figure 2.11**).

Liger-Belair *et al.*[49] detail the process of CO_2 bubble nucleation following type IV. It is interesting to note that the proposed cycle can be also observed in other systems that present a dissolved gas and gas cavity. **Figure 2.12** presents a schematic representation of a pre-existing gas cavity immerged in a supersaturated solution, CO_2 in their study case. The difference between the liquid bulk concentration and the bubble surface is the driving force for nucleating bubbles. **Figure 2.12** presents the involved forces during bubble detachment. They are the buoyancy force (F_B) and capillary force (F_C).

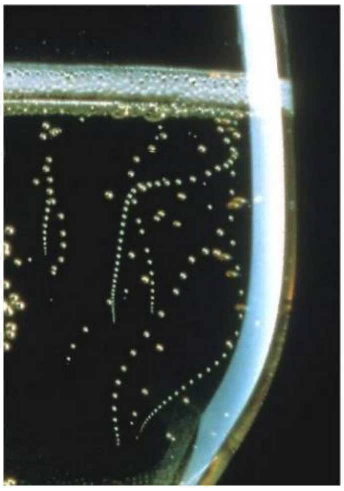

Figure 2.11: Bubble train nucleated from pre-existing gas cavities in champagne bubbles.[27]

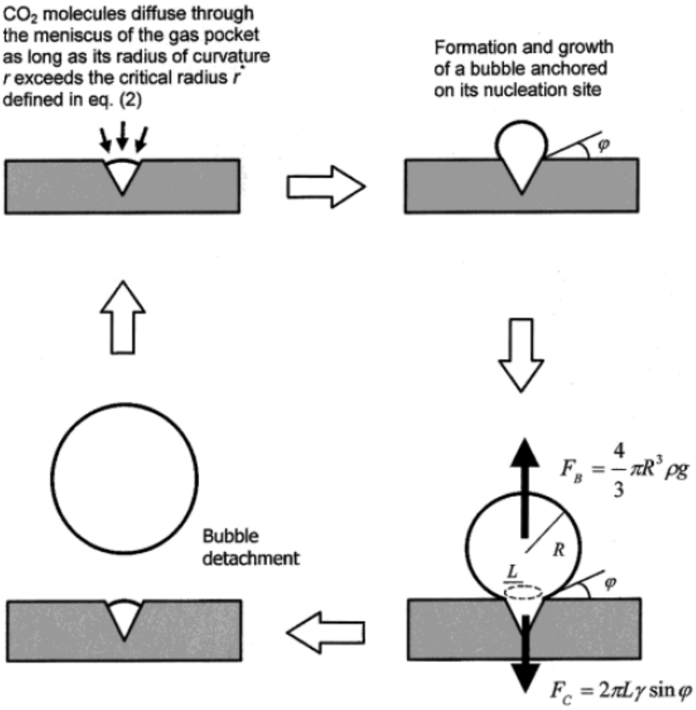

Figure 2.12: Schematic representation of bubble nucleation following type IV. Buoyancy force and capillary force are displayed as well.[49]

Another daily observation that illustrates this previous idea is that the presence of gas cavities explains the general increase on nucleation rates is the presence of either dirty or rough surface. Indeed, these external surfaces contains gas cavities, it favors nucleation types III or IV, requiring then lower or no supersaturation levels to start nucleation. Therefore, nucleation takes place in a large range of temperatures and lasts longer. It is important mentioning that types I and II present higher maximum nucleation and last less time. Another key point that affects nucleation rate is the number of cavities and the liquid-solid interface.[46]

2.2.3 Conclusion

Once molecular oxygen is formed through redox reaction, this gas is physically dissolved in the glassy matrix up to reach the saturation and supersaturation levels. In this section, we presented these two concepts as well as their governing equations. Besides, we presented the bubble nucleation models currently used in the literature (types I, II, III and IV). In each of these models, we exhibited some features, governing laws as well as some examples. Nucleation study is important to give us clues about the nucleation type in which bubbles are formed in our glass melt system. Once the nucleation type is known, different features and characteristics can be extracted, such as the saturation level required and the position in which they were nucleated. These acquired information would be important, for example, to feed the numerical calculation code.

2.3 Bubble Growth Mechanisms

Up to now, we understood how molecular oxygen forms due to redox reactions and also how bubble nucleation takes place. After being nucleated, bubbles might undergo different growth phenomena, such as mass transfer, coalescence and/or Oswald ripening. In a given system, more than one growth phenomena might occur simultaneously. Knowing these growth phenomena one can predict features of the melt system in a given moment of the future. We dedicate this section to present mass transfer phenomenon and its governing laws. We also describe globally coalescence and Ostwald ripening processes.

2.3.1 Mass transfer

Mass transfer is a growth mechanism present in natural and artificial systems. Its origin is the difference of gas concentration between the bubble and its vicinity. Mass transfer might happen in a static situation where there is no relative movement between the gas inclusion and the liquid (pure diffusive case).[53] Mass transfer also takes place when bubbles are moving and the mass transfer in this advection case is enhanced.[10-12] Due to the nature of the studied material, we are interested here in mass transfer of gaseous species in a liquid, more specifically viscous liquid (Stokes flow or creeping flow).

Throughout the last decades, mass transfer models between bubbles immersed in molten glasses have been enhanced and new conditions have been considered. In this report, we announce two mass transfer models developed for bubbles in molten glasses. The first one is the one published by Doremus,[53] in which he studied mass transfer between a molten glass and spherical bubbles based on diffusion-controlling process. The second model is the one developed by Pigeonneau[10] in which he considered a multicomponent rising bubble with a known initial composition immersed in a glass melt with instantaneous redox reaction. In the current thesis investigation, we used this latter method to study the mass transfer between oxygen bubbles and the borosilicate melt doped with cerium oxide.

I. Pure diffusion mass transfer – single gas bubble

Doremus[53] estimated mathematically the experimental data acquired by Greene and Gaffney.[54,55] They have carried out measurements to study the contraction of a static oxygen bubble in molten glasses at an isothermal condition.

Let's consider a bubble of initial radius a_0, surrounded by a large amount of molten glass that has just one dissolved gas (i) with uniform concentration over the bulk melt equals to C_i^{∞}. Under certain conditions, the bubble's radius may contract or expand with time, having then a radius "a" for the instant of time t. In his work, Doremus[53] followed some assumptions:

- Gas diffusion is the only process that affects the rate of the growth or contraction of the spherical bubble and advection is neglected,
- Gas concentration in the bubble (C_i^b) is uniform and constant with time,
- The gas concentration on the bubble surface (C_i^s) is uniform and constant with time
- The molten glass is large enough to not have its concentration changed over time due to mass transfer and this concentration is equal to C_i^{∞}
- The diffusion coefficient (D_i) is not function of the gas concentration or time.

Under these mentioned conditions, the diffusive flux (J) per unit of area and time ($\frac{Kg}{m^2.s}$) for a growing or shrinking sphere of initial radius a_0 , in (m) is given by:

$$J = \frac{(C_i^{\infty} - C_i^s)D_i}{a}\left(1 + \frac{a_0}{\sqrt{\pi\, D_i t}}\right), \tag{2.22}$$

where the concentrations (C_i^{∞}, C_i^s) are expressed in $\frac{Kg}{m^3}$, the radii in m, the diffusivity (D_i) in $\frac{m^2}{s}$ and the time in s. Since $J = (C_i^b - C_i^s)da/dt$, the integrated growth equation from Eq. (2.22) is:

$$a_0^2 - a^2 = 2D_i t\left(\frac{C_i^s - C_i^{\infty}}{C_i^b - C_i^s}\right)\left(1 + \frac{2a_0}{\sqrt{\pi\, D_i t}}\right). \tag{2.23}$$

The data obtained by Doremus[53] for the glass melt called "Glass no. 3" are presented in **Figure 2.13**. It displays the experimental values obtained by Greene and Gaffney[54,55] along with the calculated ones obtained by Doremus.[53] It shows the radius evolution of an oxygen bubble immersed in a borosilicate melt at different temperatures. This melt composition is similar to the current composition investigated in this PhD work, but instead of cerium, he has used arsenic as a multivalent element. It can be noticed a well estimation at the initial stages. However, for long duration or high temperatures experiments, the calculations underestimate the real diameter of the bubble.

As we can verify through **Figure 2.13,** this model does not well estimate the experimental values for long experimental durations. It can be accounted to the fact that it is considered just oxygen as gaseous species. Besides, as previously mentioned, the bubble gas concentration, the concentration on its surface and the melt bulk concentration are constant with time. Thus, this model does not take into account the decrease of mass transfer driving force and consequently the model overestimate the mass transfer exchange rate.

and besides, the redox reaction of the multivalent element is not taken into consideration neither. Therefore, the driving force for mass transfer, which is the gas concentration difference between the bubble surface and the melt bulk, is overestimated in the numerical modeling.

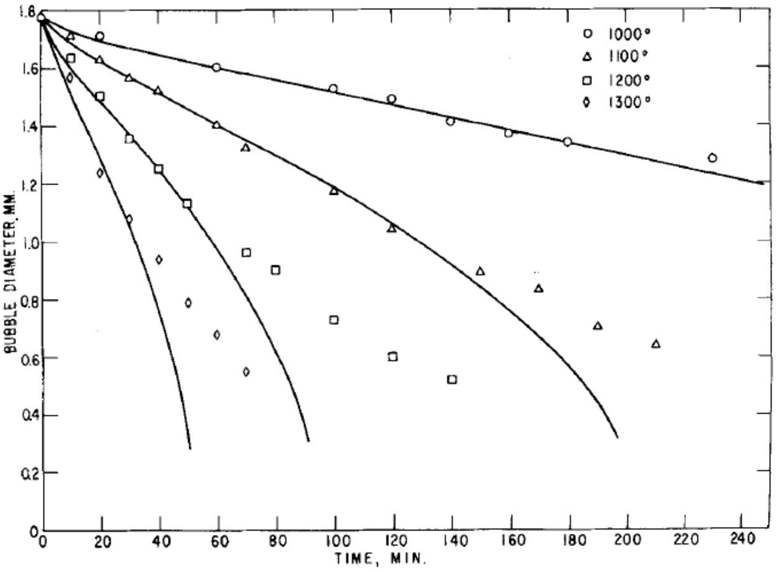

Figure 2.13: Oxygen bubble shrinkage in a molten borosilicate glass. Continuous lines were obtained from eq. (2.23),[53] while symbols from experimental data.[55]

II. Diffusion coupled with bubble movement – multicomponent bubble

We use information already provided in the redox section along with insights brought by Pigeonneau[10-12] to explain the mass transfer calculations herein. This calculation takes into consideration the mass transfer phenomenon between a freely rising bubble immersed in a molten glass with N_g gaseous species and having chemical equilibria well defined and instantaneous. Bubble's temporal evolution is done in terms of composition, radius, and vertical position. The molten glass is also temporally evaluated in terms of dissolved gas composition and redox state. This numerical computation might be applied to a bubble population system as well, under certain adaptations. In this calculations, ideal gas condition is considered and consequently, oxygen partial pressure (P_{O_2}) is taken into account instead of oxygen fugacity (f_{O_2}). Thus, Henry's law may be also applied to reach oxygen concentration.

This numerical model considers the rising bubble's interface as completely mobile. Consequently, the velocity value on the bubble surface is different from zero and there is a continuous interface renew, in terms of chemical compounds. Not only on the interface, but whole velocity field around the rising bubble is increased, being different than to a immobile interface (*e.g.* solid particles).[56] Therefore, it increase the Péclet number, which in turn, enhanced Sherwood number and mass transfer.[11] These dimensionless numbers are better explained in the following paragraphs.

Due to the mass transfer, the number of moles of each gaseous species in the studied bubble changes over time. The time derivative of the number of moles is defined by the equation:

$$\frac{dn_i}{dt} = 2\pi a Sh_i D_i (C_i^{\infty} - C_i^{s}). \tag{2.24}$$

As previously defined, a is the bubble radius at the instant of time t, D_i the diffusion coefficient of the gaseous i and C_i^{∞} the bulk molar concentration of gaseous species i. Sh_i is the Sherwood number that will be presented in the following paragraphs. Henry's law, as described previously in Eq. (2.13) is applied at the surface of the bubble.

Once the equation to reach the number of moles of each species is known, by taking ideal gas law along with hydrostatic and Laplace's pressures, the bubble radius can be determined by solving the following equation:

$$\frac{3RT\sum_{i=1}^{N_g} n_i}{4\pi a^3} = P_0 + \rho g(H - z) + \frac{2\sigma}{a}, \tag{2.25}$$

where R is the universal gas constant, T the temperature, P_0 the atmospheric pressure, g the gravity acceleration, H the liquid height and z the bubble's vertical position.

The Sherwood number (Sh_i) of a gaseous species i is defined as the ratio of the mass transfer coefficient with motion to the mass transfer coefficient without motion. By definition it is therefore presented as:

$$\mathrm{Sh_i} = \frac{\mathrm{h_i}\,2\mathrm{a}}{\mathrm{D_i}}, \tag{2.26}$$

where $\mathrm{h_i}$ is the mass transfer coefficient (by convection). Sherwood number can also translate the effect of bubble motion on mass transfer, meaning that mass transfer of a rising bubble is enhanced when compared to a mass transfer of a static one. This dimensionless number is also defined, as function of Péclet number, according to Clift *et al.,*[56] by the relationship:

$$\mathrm{Sh_i} = 1 + (1 + 0.564\mathrm{Pe}^{\frac{2}{3}})^{\frac{3}{4}}, \tag{2.27}$$

where Pe is the Péclet number. This latter dimensionless number quantifies the effect of advection transport over diffusional transport of a chemical compound. Thus, it is defined as:

$$\mathrm{Pe_i} = \frac{2\mathrm{a}\mathrm{V_T}}{\mathrm{D_i}}. \tag{2.28}$$

In this calculation, bubble inertia is neglected meaning that bubble rising velocity is given by its terminal velocity ($\mathrm{V_T}$), which is function of melt density (ρ) and dynamic viscosity (η) was proposed, independently, by Hadamard and Rybczynski[57,58] as:

$$\mathrm{V_T} = \frac{\mathrm{g}\mathrm{a}^2\,\rho}{3\,\eta}. \tag{2.29}$$

Pigeonneau[10] suggested the use of the aforementioned Péclet number for non-refining gases, such as $\mathrm{N_2}$ and $\mathrm{CO_2}$. For refining gases, such as $\mathrm{O_2}$, which is related to a redox reaction, he proposed the use of a modified Péclet number ($\mathrm{Pe_i'}$). Physically, this novel dimensionless number translates the idea that a gas involved in a chemical reaction enhances the mass transfer. In the current studied case, it enhances the mass transfer because the cerium presence, nearby the bubble, helps to pump molecular oxygen from the bubble to the melt, making the bubble shrinkage faster. This proposed dimensionless number is given by the relationship:

$$\mathrm{Pe'_{O_2}} = \mathrm{Pe_{O_2}}[1 + \alpha\,(\mathrm{Sa_{O_2}})\mathrm{N_{Ce}}], \tag{2.30}$$

where $\alpha\,(\mathrm{Sa_{O_2}})$ is numerically fitted for different cases[10] and is defined as:

$$\frac{1}{\alpha} = \frac{1}{3.05\mathrm{Sa_{O_2}^{-0.375}}} + \frac{1}{1.28\mathrm{Sa_{O_2}^{-1}}}. \tag{2.31}$$

The oxygen saturation, $\mathrm{Sa_{O_2}}$, is given by:

$$\mathrm{Sa_{O_2}} = \frac{\mathrm{C_{O_2}^{\infty}}}{\mathrm{C_{O_2}^{s}}}, \tag{2.32}$$

where $C_{O_2}^{\infty}$ and $C_{O_2}^{s}$ are the bulk and bubble surface oxygen concentration, respectively. The dimensionless number, N_{Ce}, is defined as follows:

$$N_{Ce} = \frac{C_{Ce^{3+}}^{\infty}(1 - R^{\infty})Sa_{O_2}^{1/4}}{16C_{O_2}^{s}}, \tag{2.33}$$

in which R^{∞} is the cerium redox state defined by:

$$R^{\infty} = \frac{C_{Ce^{3+}}^{\infty}}{C_{Ce^{3+}}^{\infty} + C_{Ce^{4+}}^{\infty}}. \tag{2.34}$$

Through analyzing this series of equations, besides observing the influence of the oxygen partial pressure on mass transfer, it can be also concluded that through increasing the total amount of the multivalent species, the modified Péclet number enhances, making Sherwood number greater and consequently mass transfer is also increased.[10]

To conclude, we present a published result[11] showing the bubble size as function of time for a bubble initially composed by oxygen. This bubble was immersed in a silicate melt doped with iron oxide and the mass transfer was studied experimentally and by numerical simulations using this mass transfer model just presented in this work. The authors in this work validated the use of the “modified Péclet” for a silicate melt doped with iron oxide, showing that iron redox reaction enhances mass transfer coefficient due to its total amount and iron reduced ratio.

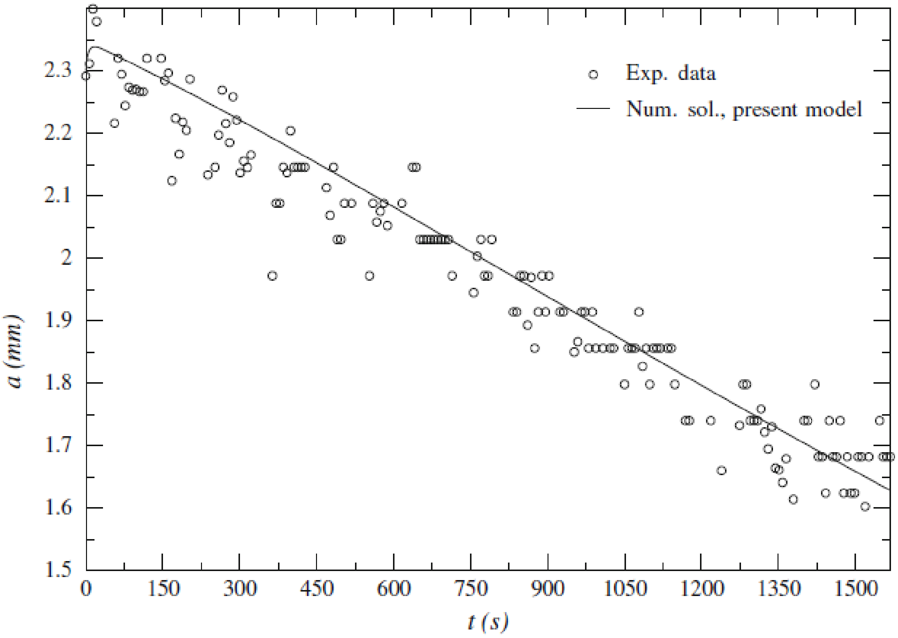

Figure 2.14: Bubble size as function of time for a silicate melt doped with iron oxide at 1300 °C. A comparison between values obtained by the presented model and by experimental data is presented.[11]

2.3.2 Coalescence

Bubble coalescence is an important phenomenon which is vastly present in different fields of science, such as secondary refining process in steel making industry,[59,60] liquid-liquid extraction employed in nuclear recycling industry[61] and geological degassing processes.[62,63] This is a process in which two inclusions (*e.g.* bubbles or droplets) collide and merge becoming a large one. Therefore, the process of coalescence is another growth mechanism which makes bubble mean diameter increase while total number of inclusions decreases. It was firstly applied to glass science by Ungan *et al.*[64]

One can characterize bubble coalescence by different events. Firstly, bubbles might get close and collide with each other in order to allow coalescence to take place.[65] It generates and thinning of the film between the involved bubbles which might cause bending, stretching and dimpling.[62] Finally, as the liquid film thickness reduces below a certain value, it breaks, leading to coalescence. Boshenyatov[66] mentions in his book that not all of the collision events result in coalescence. Therefore, one considers also the probability of film rupture and consequently, coalescence process is characterized by two main events: bubble collision and the probability of film rupture. Thus, the coalescence rate of bubbles x and y is expressed as:

$$\Omega_{\mathrm{xy}} = \omega_{\mathrm{xy}}.\mathrm{P}_{\mathrm{xy}}, \tag{2.35}$$

where Ω_{xy} is the coalescence rate expressed by the number coalescence events per unit of time (s^{-1}), ω_{xy} is the collision frequency also expressed by (s^{-1}) and P_{xy} is the probability of rupture, that is also called coalescence efficiency which is dimensionless. Collision frequency is a complex function of the amount of bubbles, size distribution and flow properties. Due to the dependency on bubble number density, coalescence is more likely to happen in the initial stages, where this density is more elevated.[67] The probability of rupture is defined based on the contact time between two bubbles. If this contact time is greater than the required draining time, bubbles undergo coalescence, otherwise they do not.[66]

By way of illustration, we present some results obtained by Martel and Iacono-Marziano.[62] They investigated, through decompression-induced degassing experiments, the roles of some parameters such as melt composition, crystallization, pressure and temperature on the mechanism and timescales of bubble coalescence and outgassing. According to them, due to the elevated viscosity of the system, bubbles hardly move and they stay roughly where they were nucleated.[63] They observed an increase of bubble mean diameter and a general decrease of bubble mean density. However, for this type of system, bubble coalescence might eventually generate gas channels leading to an interconnection of bubbles. At this point of high fluid permeability, the magma either stays as a foam or the gas escapes leading to a foam collapse.[62] Outgassing and foam collapse imply a strong decrease in bubble surface fraction accompanied by a drastic decrease in bubble mean density and bubble mean diameter. In a presence of insoluble crystals, these phenomena also seem to take place for glass melts.

2.3.3 Ostwald ripening

Ostwald ripening is an observed phenomenon in different industrial and daily events. One can highlight different systems in which it can be observed, such as $\mathbf{RuO_2}$ particles in high-level waste glass melts[68] and even salad dressing solution containing oil and vinegar. Ostwald ripening named after Wilhelm Ostwald, also called “coarsening”, and is a thermodynamic growth mechanism of particle (*e.g.* crystal, bubbles and droplets) in which larger particles grow at the expenses of smaller ones. It takes place by small particles dissolution and re-deposition, by diffusion, onto larger ones.[69]

Ostwald ripening is driven by surface energy reduction. It is well known that atoms in the surface of particles are less energetically stable than atoms in the bulk. Large particles, when compared to smaller ones, have relatively more atoms in the bulk than in the surface. Therefore, it makes the former more energetically stable then the latter. Hence, the idea behind Ostwald ripening mechanism is to decrease the thermodynamic energy of the system by dissolving smaller particles and redepositing then onto large ones.

Lifshitz and Slyozov[70] and Wagner[71] described, theoretically, Ostwald ripening phenomenon by considering the interaction of dispersed particles of various size with a mean concentration field, rather than with one other particle directly. This is the so-called LSW approach for Ostwald ripening. It might be either limited by diffusion processes or by attachment/detachment of molecules. These two different limiting processes have different physical laws governing the final growth mechanism. Particle radius increases with $\mathrm{t}^{-1/3}$ for the former process and with $\mathrm{t}^{-1/2}$ for the latter one. It is displayed by the following equations respectively:

$$\langle \mathrm{a} \rangle^3 + \langle \mathrm{a} \rangle_0^3 = \frac{8\,\sigma\,\mathrm{C_i^{\infty}}\,\vartheta^2 \mathrm{D_i}}{9\mathrm{RT}}\mathrm{t} \tag{2.36}$$

$$\langle \mathrm{a} \rangle^2 = \frac{64\,\sigma\,\mathrm{C_i^{\infty}}\,\vartheta^2 \mathrm{k_s}}{81\mathrm{RT}}\mathrm{t} \tag{2.37}$$

In which $\langle \mathrm{a} \rangle$ is the average radius of all particles of the system, ϑ the molar volume of the particle material and $\mathrm{k_s}$ the reaction rate constant of attachment (m/s).

Bubble growth by Ostwald ripening are intimately related to gas permeability (which is proportional to the product of diffusion and solubility coefficients) and distance between particles.[37] Usually, this growth mechanism is observed in systems that present higher gas permeability and low mean distance between particles. Bolorė and Pigeonneau,[37] for example, did not observe bubble ripening in their system. It is probably due to the lower permeability of the dissolved gases. The product between diffusivity ($\mathrm{D_i}$) and gas solubility ($\mathrm{L_i}$) characterizes the gas permeability of gaseous species i.[12] Lautze *et al.*[50] have studied $\mathrm{H_2O}$ and $\mathrm{H_2O-CO_2}$ bubbles in natural magmas. Concerning to gas permeability, they have concluded that samples containing $\mathrm{CO_2}$ undergone this phenomenon slower than the theoretical rates for the steady state ripening. It is believed to be due to the lower permeability of carbon dioxide when compared to water vapor. **Figure 2.15** exhibits an interesting behavior of particles undergoing Ostwald ripening phenomenon. This figure displays water bubbles in rhyolite obsidian samples at 750 °C and 100 MPa. It can be seen the cross-section areas for different times, starting from 1 day until 4 months.

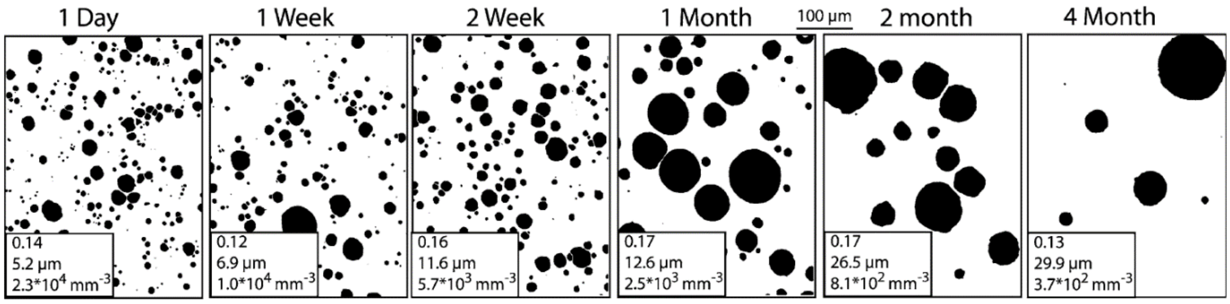

Figure 2.15: Bubbles undergone coarsening (black) in rhyolite obsidian melt (white).[50]

2.3.4. Conclusion

In this section, we presented bubble growth mechanisms in molten glasses. It was firstly discussed mass transfer between bubble and molten glass. In this subsection we presented two models. Coalescence mechanism was presented and practical examples were given. Lastly, Ostwald ripening, also called coarsening, was featured and examples were presented and discussed. Growth mechanism investigation is important because well understanding their contributions, we can make predictions about different features and characteristics of the bubbled-melt. Furthermore, knowing the growing mechanism along with properties of the melt system, mathematical models can be developed to forecast bubble(s) behavior over time.

2.4 Conclusion

In this chapter we described the current state of art in terms of oxygen bubble formation linked to redox reaction in nuclear waste vitrification context. We firstly went through redox reactions in glass melts, which are the source of molecular oxygen in the system. We presented their fundamental laws as well as the role of each parameter along with some key elements in nuclear waste vitrification context. After understanding how molecular oxygen might be produced in the melt, gas saturation and supersaturation were described along with nucleation types. The latter are intrinsically related to the formers. Finally, after being nucleated, these bubbles may undergo different growth mechanism. Thus, we dedicated the last part of this literature review to describe mass transfer and its governing laws as well as coalescence and Ostwald ripening descriptions.

Thus, understanding well redox reactions in oxide melts helps us to understand how these reactions affect bubble nucleation and behavior in melts. The comprehension of the bubble nucleation type gives different information about the system itself, such as the level of supersaturation preceding the nucleation event, as well as clues about nucleation position. Growth mechanism are extremely important to be understood since they govern bubble behavior over time. Understanding well the major growth mechanism present in the system, one can make predictions. To conclude, understanding well these three big fields of this thesis, we can make numerical calculations in order to forecast bubble(s) and melt properties over time.

In this bibliographic chapter, we highlighted the importance of different physical-chemical properties of the melt (viscosity, density, surface tension, gas diffusivity) and showed how they affect bubble and melt features. Moreover, we presented two mass transfer models, which needs these physical-chemical properties are useful as input values. In this way, we use the next chapter to present the studied glass melt, presenting the compositions, the executed physical-chemical characterizations as well as some redox and fining characteristics.

2.5 References

(1) Parker, J. M. *Review of Progress in Coloration and Related Topics* **2004**, *34*, 26.

(2) Pereira, L. F. P.; Bodiang, K.; Nunes, E. H. M.; Mear, F. O.; Delevoye, L.; Montagne, L. *Journal of Physical Chemistry C* **2018**, *122*, 15886.

(3) Möncke, D.; Jiusti, J.; Silva, L. D.; Rodrigues, A. C. M. *Journal of Non-Crystalline Solids* **2018**, *498*, 401.

(4) Abbas, L.; Bih, L.; Nadiri, A.; El Amraoui, Y.; Mezzane, D.; Elouadi, B. *Journal of Molecular Structure* **2008**, *876*, 194.

(5) Shelby, J. E. *Introduction to glass science and technology*; The Royal Society of Chemistry: Cambridge, **2005**.

(6) Cable, M. *Journal of the American Ceramic Society* **1998**, *81*, 1083.

(7) Cachia, J. N.; Deschanels, X.; Den Auwer, C.; Pinet, O.; Phalippou, J.; Hennig, C.; Scheinost, A. *Journal of Nuclear Materials* **2006**, *352*, 182.

(8) Pinet, O.; Hugon, I.; Mure, S. *Procedia Materials Science* **2014**, *7*, 124.

(9) Pigeonneau, F. *Glass Technology: European Journal of Glass Science and Technology Part A* **2007**, *48*, 66.

(10) Pigeonneau, F. *Chemical Engineering Science* **2009**, *64*, 3120.

(11) Pigeonneau, F.; Martin, D.; Mario, O. *Chemical Engineering Science* **2010**, *65*, 3158.

(12) Pigeonneau, F. *International Journal of Heat and Mass Transfer* **2011**, *54*, 1448.

(13) Cicconi, M. R.; Moretti, R.; Neuville, D. *Elements* **2020**, *16*, 157.

(14) Cicconi, M. R.; Le Losq, C.; Moretti, R.; Neuville, D. *Elements* **2020**, *16*, 173.

(15) de Best, A. W. M., Technische Universiteit Eindhoven, **1994**.

(16) Pinet, O.; Phalippou, J.; Di Nardo, C. *Journal of Non-Crystalline Solids* **2006**, *352*, 5382.

(17) Pinet, O.; Mure, S. *Journal of Non-Crystalline Solids* **2009**, *355*, 221.

(18) Kress, V. C.; Carmichael, I. S. E. *Contributions to Mineralogy and Petrology* **1991**, *108*, 82.

(19) Le Losq, C.; Cicconi, M. R.; Neuville, D. *Earth and Space Science Open Archive* **2020**, *1*.

(20) Schreiber, H. D.; Balazs, G. B.; Carpenter, B. E.; Kirkley, J. E.; Minnix, L. M.; Jamison, P. L.; Mason, T. O. *Journal of the American Ceramic Society* **1984**, *67*, C.

(21) Rüssel, C. *Journal of Non-Crystalline Solids* **1990**, *119*, 303.

(22) Russel, C. *Glastechnische Berichte* **1989**, *62*, 199.

(23) Duffy, J. A.; Ingram, M. D. *Journal of Non-Crystalline Solids* **1976**, *21*, 373.

(24) Duffy, J. A.; Ingram, M. D. *The American Ceramic Society* **1991**, 159.

(25) Pye, D. L.; Montenero, A.; Joseph, I. *Properties of Glass-Forming Melts*; Taylor & Francis Group: 6000 Broken Sound Parkway NW, Suite 300 Boca Raton, FL 33487-2742, **2005**.

(26) Vernaz, E.; Gin, S.; Veyer, C. *Waste Glass. In: Konings R.J.M., (ed.) Comprehensive Nuclear Materials*; Elsevier: Amsterdam, **2012**; Vol. 5.

(27) Jones, S. F.; Evans, G. M.; Galvin, K. P. *Advances in Colloid and Interface Science* **1999**, *80*, 27.

(28) Vernerová, M.; Cincibusová, P.; Kloužek, J.; Maehara, T.; Němec, L. *Journal of Non-Crystalline Solids* **2015**, *411*, 59.

(29) Hurwitz, S.; Navon, O. *Earth and Planetary Science Letters* **1994**, *122*, 267.

(30) Mourtada-Bonnefoi, C. C.; Laporte, D. *Journal of Geophysical Research: Solid Earth* **2002**, *107*, 2.

(31) Mourtada-Bonnefoi, C. C.; Laporte, D. *Geophysical Research Letters* **1999**, *26*, 3505.

(32) Gardner, J. E.; Hajimirza, S.; Webster, J. D.; Gonnermann, H. M. *Geochimica et Cosmochimica Acta* **2018**, *226*, 174.

(33) Bisperink, C. G. J.; Prins, A. *Colloids and Surfaces A: Physicochemical and Engineering Aspects* **1994**, *85*, 237.

(34) Energy, U. S. D.; Scientific diving, **2015**, 1.

(35) Lubetkin, S. D. *Langmuir* **2003**, *19*, 2575.

(36) Puhl, H. *Chemie Ingenieur Technik* **1991**, *63*, 1272.

(37) Boloré, D.; Pigeonneau, F. *Journal of the American Ceramic Society* **2018**, *101*, 1892.

(38) Volmer, M.; Weber, A. *Zeitschrift fur Physikalische Chemie* **1926**, 277.

(39) Vachaparambil, K. J.; Einarsrud, K. E. *Journal of the Electrochemical Society* **2018**, *165*, E504.

(40) Blander, M.; Katz, J. L. *AIChE Journal* **1975**, *21*, 833.

(41) Harvey, E. N.; Barnes, D. K.; McElroy, W. D.; Whiteley, A. H.; Pease, D. C.; Cooper, K. W. *Journal of Cellular and Comparative Physiology* **1944**, *24*, 1.

(42) Zanotto, E. D.; James, P. F. *Journal of Non-Crystalline Solids* **1985**, *74*, 373.

(43) Hemmingsen, E. A. *Journal of Applied Physics* **1975**, *46*, 213.

(44) Rose, P. B.; Woodward, D. I.; Ojovan, M. I.; Hyatt, N. C.; Lee, W. E. *Journal of Non-Crystalline Solids* **2011**, *357*, 2989.

(45) Gonnermann, H. M.; Gardner, J. E. *Geochemistry, Geophysics, Geosystems* **2013**, *14*, 4758.

(46) Bolore, D., Universite Pierre et Marie Curie, **2017**.

(47) Dean, R. B. *Journal of applied physics* **1944**, *15*, 446.

(48) Rakhimov, R. R.; Turney, V. J.; Jones, D. E.; Dobryakov, S. N.; Borisov, Y. A.; Prokof'ev, A. I.; Aleksandrov, A. I. *Journal of Chemical Physics* **2003**, *118*, 6017.

(49) Liger-Belair, G.; Vignes-Adler, M.; Voisin, C.; Robillard, B.; Jeandet, P. *Langmuir* **2002**, *18*, 1294.

(50) Lautze, N. C.; Sisson, T. W.; Mangan, M. T.; Grove, T. L. *Contributions to Mineralogy and Petrology* **2011**, *161*, 331.

(51) Reuss, A. *ZAMM - Journal of Applied Mathematics and Mechanics / Zeitschrift für Angewandte Mathematik und Mechanik* **1929**, *9*, 49.

(52) Liger-Belair, G. *The European Physical Journal Special Topics* **2012**, *201*, 1.

(53) Doremus, R. H. *Journal of the American Ceramic Society* **1960**, *43*, 655.

(54) Greene, C. H.; Gaffney, R. F. *Journal of the American Ceramic Society* **1959**, *42*, 271.

(55) Greene, C. H.; Kitano, I. *Glastech. Ber* **1959**, *32K*, 44

(56) Clift, R.; Grace, J.; Weber, M.; Dover Publications: New York, **1978**.

(57) Hadamard, J. S. *C. R. Acad. Sci.* **1911**, *152*, 1735.

(58) Rybczynski, W. *Bull. Acad. Sci. Cracovie* **1911**, *A*, 40.

(59) Liu, W.; Lee, J.; Guo, X.; Silaen, A. K.; Zhou, C. Q. *steel research international* **2019**, *90*, 1800396.

(60) Barnes, R. S.; Mazey, D. J.; Cottrell, A. H. *Proceedings of the Royal Society of London. Series A. Mathematical and Physical Sciences* **1963**, *275*, 47.

(61) Castellano, S., Universite Claude Bernard (Lyon), **2019**.

(62) Martel, C.; Iacono-Marziano, G. *Earth and Planetary Science Letters* **2015**, *412*, 173.

(63) Martel, C.; Bureau, H. *Earth and Planetary Science Letters* **2001**, *191*, 115.

(64) Ungan, A.; Turner, W. H.; Viskanta, R. *Glastechn. Ber.* **1983**, *56*, 125.

(65) Vrij, A. *Discussions of the Faraday Society* **1966**, *42*, 23.

(66) Boshenyatov, B.; New-York: Nova Science Publishers: New York, **2012**, p 211.

(67) Cable, M. *Glass Technol.* **1961**, *2*, 60.

(68) Boucetta, H.; Podor, R.; Stievano, L.; Ravaux, J.; Carrier, X.; Casale, S.; Gossé, S.; Monteiro, A.; Schuller, S. *Inorganic Chemistry* **2012**, *51*, 3478.

(69) Ostwald, W. *Lehrbuch der allgemeinen chemie*; W. Engelmann: Leipzig, **1896**.

(70) Lifshitz, I. M.; Slyozov, V. V. *Journal of Physics and Chemistry of Solids* **1961**, *19*, 35.

(71) Wagner, C. *Zeitschrift für Elektrochemie, Berichte der Bunsengesellschaft für physikalische Chemie* **1961**, *65*, 581.

Chapter 3

Materials and Properties

Chapitre 3

Matériaux et Propriétés

Résumé : Ce chapitre est consacré à la présentation des échantillons de verre et verres fondus utilisés au cours de cette thèse ainsi que leurs propriétés physico-chimiques. Tout d'abord, nous exposons leurs compositions chimiques, ainsi que les précurseurs utilisés. Ensuite, nous présentons les caractéristiques physiques des échantillons, telles que la viscosité, la tension superficielle et la densité à haute température. Enfin, des caractéristiques thermochimiques et d'affinage, telles que la fugacité d'oxygène, la spéciation du cérium et la composition des bulles sont présentées. Les caractéristiques obtenues ici permettent de mieux comprendre la formation et le comportement des bulles dans le contexte de cette thèse. De plus, ces propriétés sont également importantes pour l'interprétation des principaux résultats, ainsi que pour alimenter la modélisation numérique qui sera appliquée par la suite.

Chapter 3

Materials and Properties

As previously mentioned, we simplified the nuclear waste glass by selecting a borosilicate glass matrix doped with a polyvalent element (cerium) to study oxygen bubble formation linked to redox reaction coming from nuclear waste.

This chapter is dedicated to present the specimens used during this PhD thesis to study bubble formation and behavior in this mentioned melt. Firstly, we present the glass and respective melt compositions, as well as the used precursors and some of their features. After, we present the physical properties, such as surface tension and high-temperature density. Lastly, redox and fining characterizations of the system, such as oxygen fugacity (f_{O_2}), cerium speciation and bubble gas composition are exhibited. These characterizations as well as the bibliographic report supports the comprehension of the effect of redox reactions on bubble formation, as well as how the system behaves in terms of bubble nucleation and growth. Thus, the scientific knowledge acquired in the bibliographic review along with the characterizations obtained here allow us to quantify bubble formation in these mentioned fields. Besides, these characterizations are also important to the main results interpretation, as well as to feed the computational modeling of mass transfer.

It is important to stress that this section contains the materials and characterization used during the PhD thesis and they are useful to support the main results of bubble observation techniques. These observation techniques to study bubbles are described in each of the results chapters.

3.1 Glass melt composition

In this PhD work, four glass compositions are used to investigate bubble formation linked to redox reactions in nuclear waste vitrification context. These compositions are based on a glass matrix (generally called “glass frit” in nuclear vitrification), doped with different amounts of the multivalent element (cerium). A borosilicate frit composition is selected due to its widely use as nuclear waste host matrix.[1,2] This glass frit is produced by an external company (FERRO). It is previously synthesized at 1450 °C in a combustion furnace powered by CH_4/O_2 (gas ratio = 1.9) and quenched between rolls which are continuously cooled, internally, by water. Hence, the glass production is made at a dry condition and the atmosphere humidity is the only source of water that the glass is subjected to. Cerium is selected as a polyvalent element due to its redox power, possible presence in different nuclear waste and influence on bubble formation.[3] CeO_2 powder is chosen as cerium oxide precursor and is manufactured by Aldrich (chemical purity > 99.9%). The difference between these four compositions is the cerium loading, which is displayed in terms of Ce_2O_3.

Table 3.1 displays these four compositions containing cerium oxide along with the glass frit composition.

Table 3.1: Glass composition in wt % for varying Ce_2O_3 loading. (Composition is not dependent on multivalent speciation).

Oxide	**Glass frit**	**Glass + 0.1 wt% Ce_2O_3**	**Glass + 0.5 wt% Ce_2O_3**	**Glass + 1.0 wt% Ce_2O_3**	**Glass + 1.5 wt% Ce_2O_3**
SiO_2	58.47	58.41	58.17	57.87	57.58
B_2O_3	18.58	18.56	18.49	18.39	18.30
Na_2O	7.01	7.00	6.97	6.94	6.90
CaO	5.17	5.16	5.14	5.11	5.09
Al_2O_3	3.99	3.99	3.97	3.95	3.93
ZnO	3.24	3.24	3.23	3.21	3.19
Li_2O	2.50	2.50	2.49	2.48	2.46
ZrO_2	0.62	0.62	0.62	0.61	0.61
K_2O	0.21	0.21	0.21	0.21	0.21
Ce_2O_3	**0.00**	**0.10**	**0.50**	**1.00**	**1.50**
BaO	0.10	0.10	0.10	0.10	0.10
TiO_2	0.08	0.08	0.08	0.08	0.08
Fe_2O_3	0.04	0.04	0.04	0.04	0.04
Total	100.0	100.0	100.0	100.0	100.0

These four investigated glasses are synthesized using the same borosilicate glass precursor but presenting different granulometries. The ones containing 0.1 wt% Ce_2O_3 are synthesized using glass powder. Since it is used to study "bubble population" system and in this study there is no pre-synthesis stage, the granulometry affects enormously bubble formation and its control must be carefully done.[4] This powder is obtained by sieving the borosilicate glass between 250 and 500 μm and this gives rise to a unimodal distribution (**Figure 3.1**). The other glass compositions (0.5, 1.0 and 1.5 wt% Ce_2O_3) are synthesized using the glass flake shape, same as the one manufactured by FERRO. These latter compositions are used in the study of "single-bubble" and in this investigation there is a pre-synthesis stage, making the influence of initial particle size not important. A typical glass flake has a thickness of about 1.5 mm and surface of about 50 mm^2. The cerium precursor is CeO_2 powder with its particle size distribution (PSD) displayed in **Figure 3.1**. The multimodal behavior of the CeO_2 PSD (**Figure 3.1**) is believed to be due to particle agglomeration. Thus, the peak, centered between 10^{-2} and 10^{-1} μm, is the real particle size distribution and the two large ones are due to particle agglomeration due to humidity. This cerium oxide precursor is used for all the studied samples.

These mentioned particle size distributions are obtained through laser granulometry (Malvern Mastersizer 3000) experiment and **Figure 3.1** presents the PSD for the borosilicate glass powder and for the CeO_2 powder. Glass powder, represented in semi-log scale in x-axis, presents roughly a mono-modal log-normal distribution in terms of size, while CeO_2 powder presents a multimodal distribution. The glass flakes are not evaluated since the particles are much larger than the equipment allowed dimensions.

For all of these studied samples, the specimens are synthesized in an isothermal condition during different durations. The ones containing 0.1 wt% Ce_2O_3 (bubble population study) are synthesized from 800 to 1100 °C while the other ones (single-bubble study) are pre-synthesized at 1200, 1300 and 1400 °C. The choice of these temperatures and durations depend on the goals of each of these investigations and they are described in each of these sections.

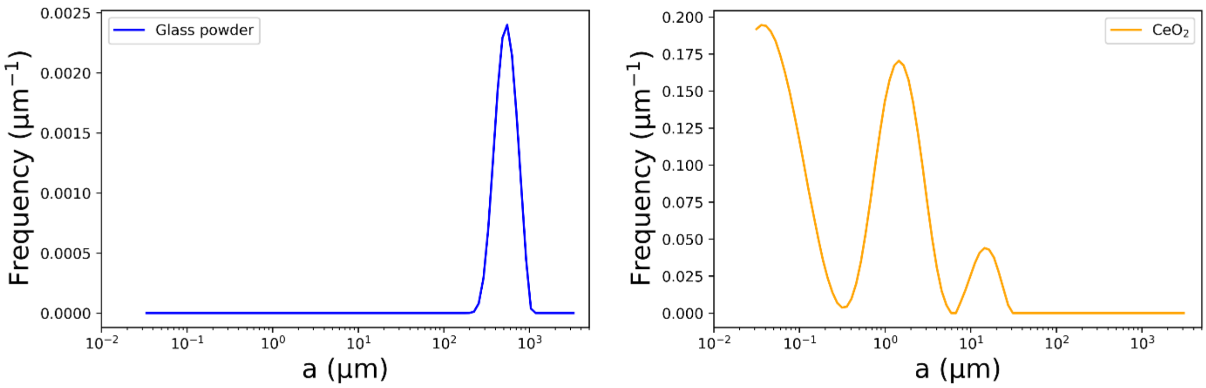

Figure 3.1: PSD for borosilicate glass and CeO_2 powders obtained by laser granulometry.

Density measurement on the bulk glass is performed at room temperature using the Archimedean method with water as an immersion fluid and a Metter AT200 scale. The bubbled-free borosilicate glass density at room temperature is 2486 Kg.m^{-3}. The glass powder packing factor is determined experimentally considering the apparent and bulk densities. It corresponds to 50 % in volume, meaning that 50 % of a fulfilled reservoir is composed of air.

Differential thermal analysis (DTA) is carried out using a Setaram TGA 92 – 16 thermal analyzer. It is executed in air at a constant heating rate of 10 °C/min. This technique makes it possible to determine the transformations of the material by measuring the temperature difference in relation to a reference sample. In this work, we are mainly focused on the glass transition temperature (T_g), which is equal to 531 °C (804 K).

3.2 Physical characterizations

As previously described in the bibliographic chapter, several parameters of the system are function of physical properties. Thus, we dedicate this section to describe some physical properties which are used in the following chapters to help the results interpretation. These obtained parameters are also important to feed the numerical simulation code. The mentioned results and mathematical computations are described in the sections "single-bubble" and "bubble population". Thus, in this section we go through viscosity, surface tension and high-temperature density measurements. Besides, we also present some parameters extracted from the literature, such as diffusivity and solubility, which are useful during the numerical computations.

3.2.1 Viscosity

Viscosity measurements on the melts are carried out by the technical team from our laboratory in CEA Marcoule. These measurements are performed with Searle coaxial cylinder viscometer coupled to a resistance furnace.[5] There are a stationary crucible and the rotor which are made of platinum-rhodium. The former has internal diameter of 27 mm and the latter has a diameter of 9 mm and is driven in rotation by a scientific rheometer to measure the applied torque by the glass melt. 27 cm^3 of melt are necessary for this type of measurement. The four different glass melts with different cerium oxide loading ($\mathrm{Ce_2O_3}$ = 0.1 0.5, 1.0 and 1.5 wt%) are analyzed and viscosity values are equal within the experimental error.

The experimental results are interpolated using three viscosity models proposed for glass forming liquids. The tested viscosity models are the Vogel-Fulcher-Tammann (VFT),[6-8] the Mauro-Yue-Ellison-Gupta-Allan (MYEGA)[9] and the Avramov-Milchev (AM).[10] Within the studied temperature range considered in this doctorate study, these three models well estimate viscosity values for the experimental data with $R^2 > 0.99$. Therefore, in this work, we use the parameters obtained using the well-known VFT law as follows:

$$\eta = 8.39 \cdot 10^{-3} \exp\left(\frac{6026.88}{\mathrm{T} - 610.16}\right), \tag{3.1}$$

with T in Kelvin and the dynamic viscosity (η) in $\mathrm{Pa.s.}$ **Figure 3.2** displays the aforementioned models, which are all overlapped, along with the experimental data for the studied glass melt system. Besides, we present in **Table 3.2** useful values, obtained from the VFT fitting, at some key temperatures of this work. These values are essential for the understanding of bubble behavior in the single-bubble and bubble population study. Viscosity values are also used in the interpretation of results, through normalization of bubble features. This feature is one of the most important features in terms of bubble dynamics in melts, controlling several phenomena, such as rising velocity and bubble residence time.

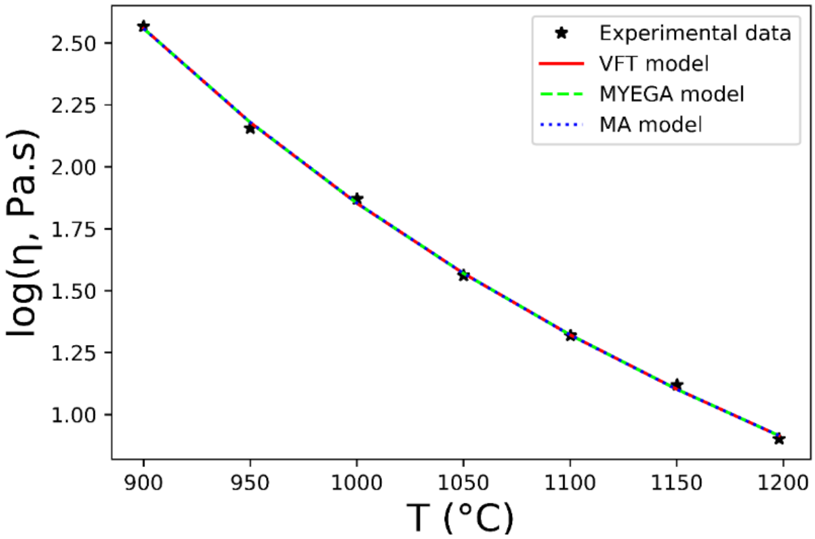

Figure 3.2: Viscosity obtained by VFT regression as function of temperature for the studied molten glass.

Table 3.2: Viscosity obtained by VFT regression as function of temperature for the studied molten glass at some key temperatures.

Temperature (°C)	Viscosity (Pa.s)
900	373.52
950	156.02
1000	74.34
1050	39.30
1100	22.59
1150	13.90

3.2.2 Surface tension

Surface tension experiments are carried out between an O_2 bubble and the borosilicate melt at the *Stazione Sperimentale del Vetro* (SSV), in Murano, Italy. It is performed using the ”maximum bubble pressure method” (MBPM) following the methodology presented by

Yamashita *et al.*[11] This method consists of blowing a bubble at the end of a tube that is vertically immersed in a molten glass. As the blown bubble is being formed, the internal pressure increases until the bubble and tube radii are equal. Beyond this size, the bubble pressure decreases with an increase of bubble radius. Therefore, when bubble and tube radii are equal, bubble internal pressure gets its maximum value (**Figure 3.3**). Hence, surface tension may be calculated, at that point, by applying Laplace's relationship.

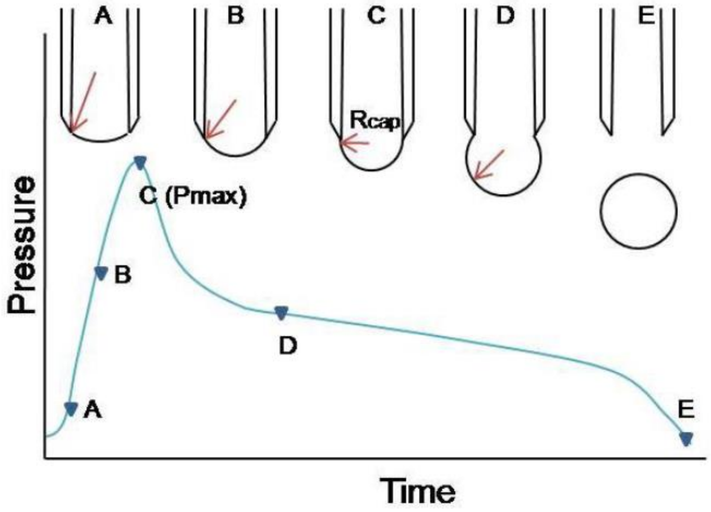

Figure 3.3: Pressure evolution in a growing bubble as function of time showing the maximum pressure in the MBPM.

$$\sigma = \frac{p.a}{2}, \qquad (3.2)$$

with p as the maximum bubble pressure in Pa, a as the radius in m and σ in N/m.

The measurements are carried out from 1000 to 1250 °C for different compositions. Surface tension measurements are performed in molten glasses without and with 1.0 wt% Ce_2O_3. The values for 0.1 and 0.5 wt% are obtained by interpolation of the previous experimental values, while the ones for 1.5 wt% are obtained by extrapolation. **Figure 3.4** and **Table 3.3** display surface tension values for the four compositions in the studied temperature range. Surface tension values obtained by this technique might be useful to calculate some bubble/melt features and it also plays a role in mass transfer, for example.

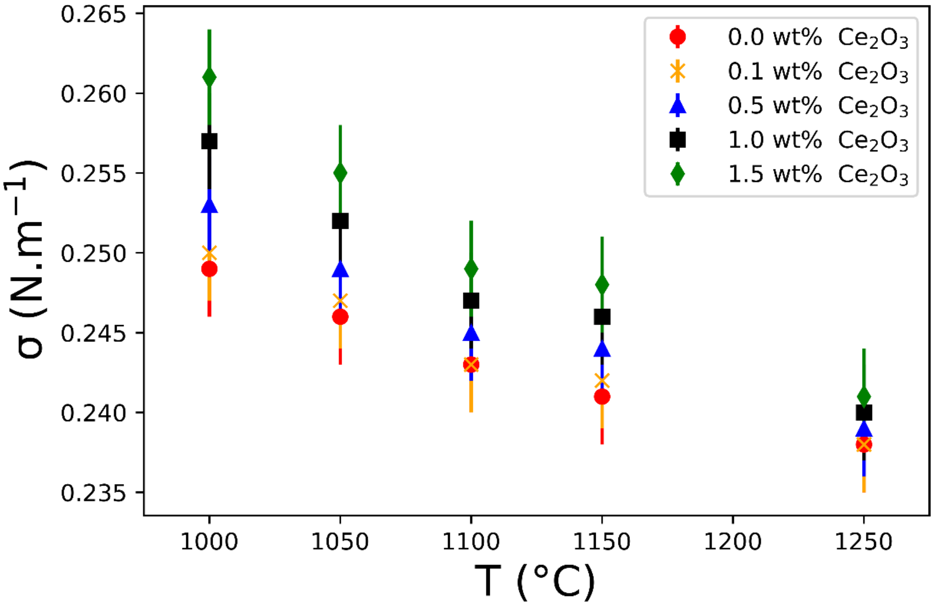

Figure 3.4: Surface tension (σ) acquired, interpolated and extrapolated for melts doped with 0.1, 0.5, 1.0 and 1.5 wt% of Ce_2O_3 from 1000 to 1250 °C.

Table 3.3: Surface tension (σ) values acquired, interpolated and extrapolated for melts doped with 0.1, 0.5, 1.0 and 1.5 wt% of Ce_2O_3 from 1000 to 1250 °C.

Surface tension (σ, N/m) $\pm$ 0.003					
Temperature (°C)	**Glass frit**	**Glass + 0.1 wt% Ce_2O_3**	**Glass + 0.5 wt% Ce_2O_3**	**Glass + 1.0 wt% Ce_2O_3**	**Glass + 1.5 wt% Ce_2O_3**
1000	0.249	0.250	0.253	0.257	0.261
1050	0.246	0.247	0.249	0.252	0.255
1100	0.243	0.243	0.245	0.247	0.249
1150	0.241	0.242	0.244	0.246	0.248
1250	0.238	0.238	0.239	0.240	0.241

3.2.3. Melt density

As for surface tension measurements, high-temperature density experiments are also performed at the *Stazione Sperimentale del Vetro* (SSV), in Murano, Italy. These measurements are carried using the Archimedean method using the molten glass as immersion fluid, a platinum sphere as immersed material and an A&D GF200 scale. High-temperature density of molten glasses are calculated by measuring the weight difference between a platinum sphere, with known volume and mass, suspended in air and in the tested melt.

High-temperature density measurements are performed from 1000 to 1300 °C for glass melts without and with 1.0 wt% of Ce_2O_3. As previously done for surface tension, the values for 0.1 and 0.5 wt% Ce_2O_3 are obtained by interpolation and the ones for 1.5 wt% of Ce_2O_3 by extrapolation of the experimental data. **Figure 3.5** and **Table 3.4** display the high-temperature density results obtained experimentally and calculated. The obtained density values might be practical for investigating some of the bubble/melt features. As presented in the bibliographic chapter, one can highlight, for example, the effect of density as on mass transfer as well as on bubble rising velocity. Density values are also used in the interpretation of results, through normalization of bubble features.

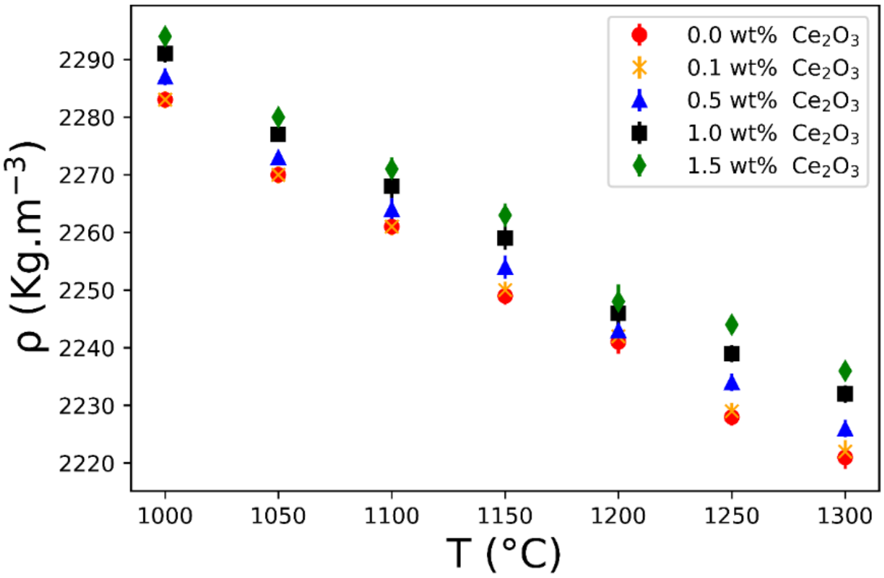

Figure 3.5: Glass melt density (ρ) acquired, interpolated and extrapolated for melts doped with 0.1, 0.5, 1.0 and 1.5 wt% of Ce_2O_3 from 1000 to 1300 °C.

Table 3.4: Glass melt density (ρ) acquired, interpolated and extrapolated for melts doped with 0.1, 0.5, 1.0 and 1.5 wt% of Ce_2O_3 from 1000 to 1300 °C.

Density (ρ, Kg/m³) $\underline{+}$ 2					
Temperature (°C)	**Glass frit**	**Glass + 0.1 wt% Ce_2O_3**	**Glass + 0.5 wt% Ce_2O_3**	**Glass + 1.0 wt% Ce_2O_3**	**Glass + 1.5 wt% Ce_2O_3**
1000	2283	2283	2287	2291	2294
1050	2270	2270	2273	2277	2280
1100	2261	2261	2264	2268	2271
1150	2249	2250	2254	2259	2263
1200	2241	2242	2243	2246	2248
1250	2228	2229	2234	2239	2244
1300	2221	2222	2226	2232	2236

3.2.4. Diffusivity and solubility

Besides the values obtained experimentally, to apply the numerical model of mass transfer to the samples of this PhD, we still need values of diffusivity and solubility. We adopt, therefore, these values for similar melt system previously published by Domerus[12] and Beerkens *et al.*[13]

Diffusivity (D_i) of each gas (oxygen, nitrogen, and carbon dioxide) is determined as a function of temperature, as presented in Eq. (3.3):

$$D_i = A_i^{diff} \exp\left(\frac{-B_i^{diff}}{T}\right), \tag{3.3}$$

where A_i^{diff} and B_i^{diff} are the diffusion constants. The constants for oxygen are adopted from Doremus,[12] for a borosilicate melt doped with a multivalent element (arsenic), and the ones for the non-fining gases (nitrogen and carbon dioxide) are adopted from Beerkens,[13] for a silicate melt. These constants are displayed in **Table 3.5**.

Table 3.5: Constants to determine the diffusion coefficients.

Gas species	Oxygen	Nitrogen	Carbon dioxide
A_i^{diff} ($m^2.s^{-1}$)	3.20×10^{-5}	4.30×10^{-5}	1.90×10^{-5}
B_i^{diff}(K)	1.61×10^{4}	1.94×10^{4}	2.15×10^{4}

Solubility coefficients (L_i) for each of the involved species (oxygen, nitrogen, and carbon dioxide) are determined as functions of temperature, as presented in Eq. (3.4):

$$L_i = A_i^{sol} \exp\left(\frac{B_i^{sol}}{T}\right), \tag{3.4}$$

where A_i^{sol} and B_i^{sol} are the constants obtained by Beerkens[14] and they are displayed in **Table 3.6**. For solubility, all of them were obtained from a silicate melt.

Table 3.6: Constants to determine the solubility coefficients.

Gas species	Oxygen	Nitrogen	Carbon dioxide
A_i^{sol} ($mol.m^{-3}.Pa^{-1}$)	1.37×10^{-5}	1.10×10^{-5}	5.60×10^{-7}
B_i^{sol}(K)	-6.63×10^{3}	-6.63×10^{3}	3.12×10^{3}

3.3 Redox and fining

We dedicate this section to describe the techniques used to characterize the glass melt system in terms of redox and fining properties. In this section we present cerium speciation, indirectly, reached via potentiometry measurements and directly reached *via* X-ray absorption near-edge structure (XANES) spectroscopy. Besides, bubble gas analysis is presented.

3.3.1 Oxygen fugacity

Oxygen fugacity measurements on the melts are carried out by the technical team from our laboratory in CEA Marcoule. Oxygen fugacity can be interpreted as the molecular oxygen activity in a given liquid. It can be also seen as the oxygen availability in this liquid.

Potentiometry measurements are executed to determine the oxygen fugacity in the melt at a given temperature. The experimental furnace device, a GS Rapidox II™ analyzer,[15] is designed by Glass Service and requires, in our configuration, about 350 g of glass. A potential difference ($\Delta\mathrm{E}$) is measured between an iridium working electrode and a reference electrode, made of Ni/NiO mixture. The electrodes are separated by a zirconia solid electrolyte doped with MgO. This doping procedure creates vacancies which allow oxygen ions to diffuse. The mentioned potential difference ($\Delta\mathrm{E}$) is linked to the temperature ($\mathrm{T_{glass}}$) and to the oxygen fugacity in the glass melt, $\mathrm{f(o_2)_{glass}}$,by Nernst equation as follows:

$$\Delta\mathrm{E} = \frac{\mathrm{RT_{glass}}}{4\mathrm{F}}\ln\left(\frac{\mathrm{f(o_2)_{glass}}}{\mathrm{f(o_2)_{ref}}}\right), \tag{3.5}$$

Measurements are performed after 25 min of stabilization at the studied temperature. The crucible is rotated at 6 rpm to avoid local concentration effect.

As previously explained in the bibliographic section, in this thesis manuscript, we considered ideal gases. Thus, oxygen fugacity is replaced by oxygen partial pressure and consequently, Henry's law can be applied to the system. This conversion is mainly done in order to be able to apply this acquired values in the mass transfer model, which will be used in the following chapters.

Here, we present therefore an example of $\mathrm{P_{O_2}}$ output obtained during a pre-defined thermal cycle. The studied melt (already doped with cerium) has been synthesized previously at 1400 °C. Afterward, the thermal equilibrium with the furnace atmosphere at 1100 °C is reached and subsequently the system is submitted to a thermal cycle of 25 minutes at two different temperatures (1125 and 1150 °C). **Figure 3.6** shows $\mathrm{P_{O_2}}$ values for a typical borosilicate glass melt doped with cerium oxide. In this figure, the black arrows point out the position in which the $\mathrm{P_{O_2}}$ values are obtained from the plot. The complete potentiometry measurement results will be presented in the single-bubble section (chapter 4) and it allows us to reach indirectly cerium speciation as presented in the bibliographic chapter.

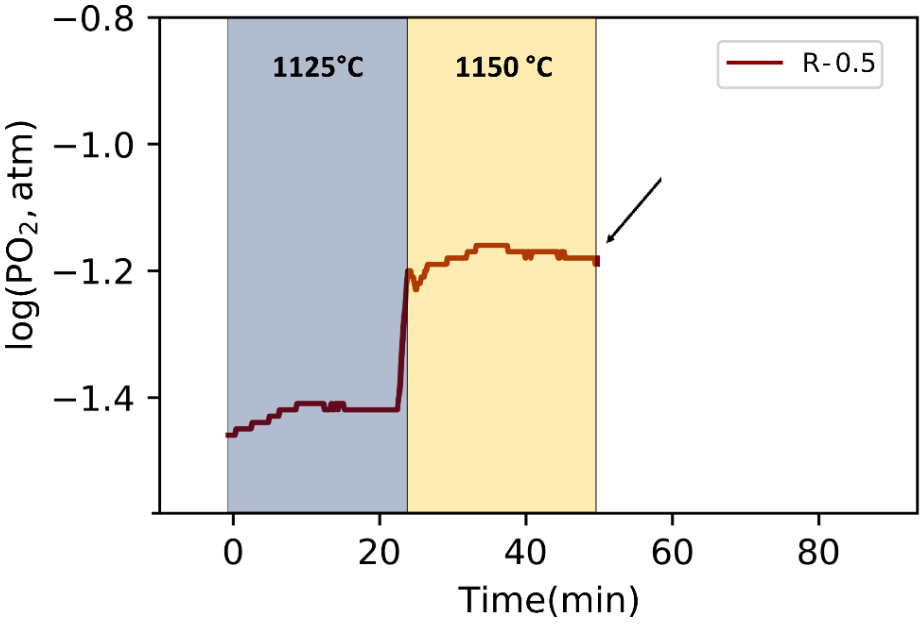

Figure 3.6: A typical log (f_{O_2}) values versus time at 1125 and 1150 °C for a borosilicate glass doped with 0.5 wt% of cerium oxide.

3.3.2 Cerium speciation by XANES spectroscopy

XANES spectroscopy measurements are carried out on the SAMBA beamline of the French National synchrotron facility (SOLEIL) and allow to reach $\mathrm{Ce(III)/Ce_{total}}$ ratio.

Experimentally, $\mathrm{CePO_4}$ and $\mathrm{CeO_2}$ powders are used, respectively, to obtain $\mathrm{Ce(III)}$ and $\mathrm{Ce(IV)}$ reference. 40 mg of glass powder, are mixed and compressed (2-3 bars) with 120 mg of cellulose to create pellets of 10 mm in diameter. Reference sample preparation is the same but using just 2.5 mg of each reference and 30 mg of cellulose.

The experiments are carried out at room temperature by Ce L_3-edge X-ray absorption spectroscopy. A fixed-exit double crystal monochromatic is used to scan the incident X-ray energy around the Ce-L_3 absorption edge, between 5.65 and 5.85 keV. A Canberra multi-elements fluorescence detector is used to record the X-ray fluorescence signal. For each sample, five spectra are collected and summed. Post-processing is performed using ATHENA software for spectra normalization and linear combination fitting.

In order to illustrate, we present in **Figure 3.7** a typical XANES plot along with the deconvoluted curves related to $\mathrm{Ce(III)}$ and $\mathrm{Ce(IV)}$ references. The complete cerium speciation results are presented in the bubble population section.

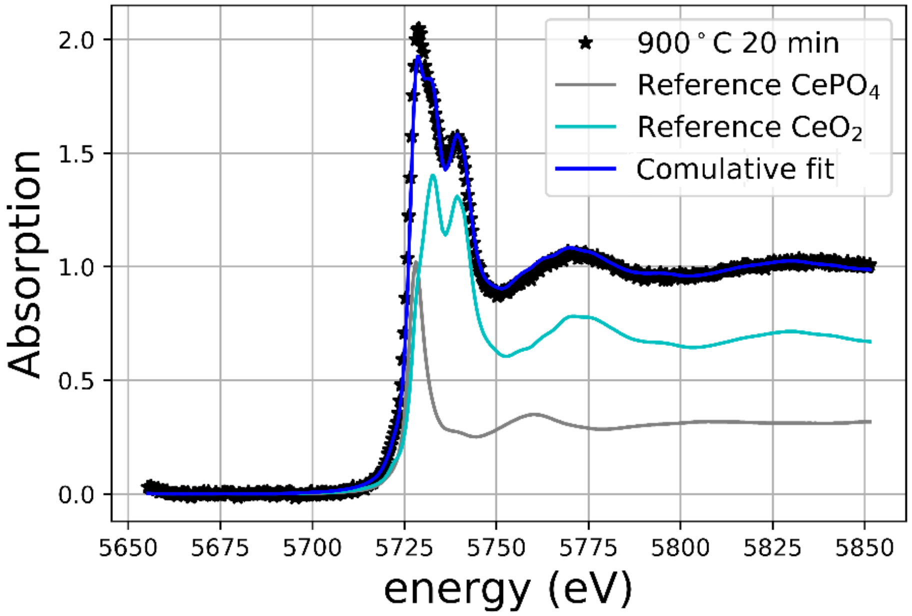

Figure 3.7: A typical XANES plot along with the deconvoluted curves related to Ce(III) and Ce(IV) references and the cumulative fit.

3.3.3. Bubble gas analysis

Bubble gas composition experiments are executed using a vacuum chamber coupled with a mass spectrometer at Eurofins EAG facilities, in The Netherlands.

Bubbled melts are quenched into solid bubbled-glass pieces, which are cut to produce glass sheets. They are cleaned with water and stored in a drying furnace (70 °C) for 24 h. Bubble gas composition is determined by an IPI LGA 407 mass spectrometer system coupled to a vacuum chamber. After pumping down the chamber, the background is measured and bubbled glass sheets are broken. Thus, the residual gas is analyzed by the mass spectrometer. During this breakage operation, several bubbles are broken and therefore the gas present in them is released at once. Hence, an average composition of bubbles is obtained in terms of non-condensed gases. The relative error of this mentioned approach is estimated at 5 %.

Figure 3.8 illustrates a typical output spectrum from the aforementioned technique to investigate gas bubble composition. It presents the electric current intensity, in Ampère (A), related to each gas species as function of time. This sample is broken at around 30 s after starting to record and the first peak intensity is used to calculate the partial pressure of each gas. For calculations, gaseous mixtures with known compositions are previously used to setup the equipment. Considering the amount of each gas species in these mixtures, each of the measured current can be related to one species and finally each gas partial pressure can be found. The sum of the partial pressures gives the final gas composition, in terms of the non-condensed gaseous species.

The samples have several bubbles and when broken, the gas is released giving rise to a peak signal. This peak is fitted using Quadstar32 software from Inficon/Pfeiffer-vacuum. The complete bubble gas analysis results will be presented in the bubble population section.

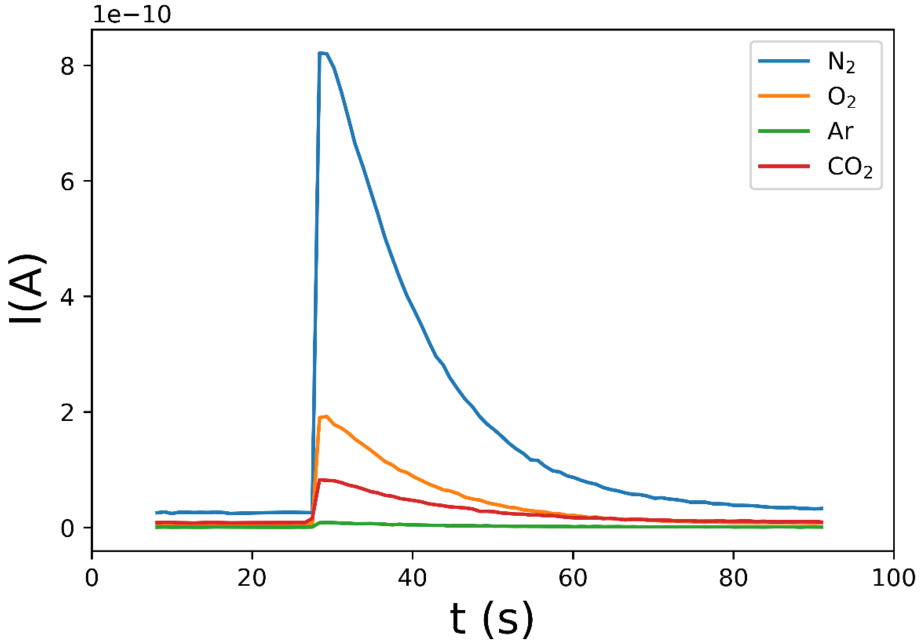

Figure 3.8: Typical gas analysis output showing intensity for each of the present gases (N_2, O_2, Ar and CO_2) over time.

3.4 Conclusion

We dedicated this chapter to present the studied glass system used to investigate bubble formation in nuclear waste vitrification context. Glass compositions and the used precursors were presented and their features were given. Besides, we dedicated this section to present physical and fining characterizations of the system.

These characterizations, as well as the bibliographic report, support the comprehension of the effect of redox reactions, nucleation and growth mechanisms of bubbles in this investigated system. Therefore, the theories and knowledge acquired in the bibliographic report along with the collected and obtained data from this chapter are extremely important to quantify bubble formation phenomena in the aforementioned fields. The values obtained here are useful for the interpretation of bubble results. We also use them as input for the mass transfer computational modeling stage.

The following sections are to present the main results of this PhD thesis. Initially (chapter 4), we study a simplified system containing just one bubble, in which we investigate the mass transfer between this single rising bubble and the melt at varying different features of the system. This mass transfer study is executed by experimental (*in-situ* camera imaging) and numerical means. Besides, an expansion to a bubble population scenario is done. By means of experimental (*post-mortem* optical microscopy) and computational modeling approach, we study the thermodynamic of the system as well as how some bubble features change over time (chapter 5). Lastly, in chapter 6, due to the laborious characteristic of the employed experimental technique used in chapter 5, we propose a novel technique to infer bubble volume fraction in a melt. Thus, in this last chapter we present this technique and a validation is done by comparing it with some well-established techniques.

3.5 References

(1) Vernaz, E.; Gin, S.; C, V.; Elsevier: Amsterdam, **2012**; Vol. 5, p 451.

(2) Plodinec, J. *Glass Technology - European Journal of Glass Science and Technology Part A* **2000**, *41*, 186.

(3) Pinet, O.; Phalippou, J.; Di Nardo, C. *Journal of Non-Crystalline Solids* **2006**, *352*, 5382.

(4) Lautze, N. C.; Sisson, T. W.; Mangan, M. T.; Grove, T. L. *Contributions to Mineralogy and Petrology* **2011**, *161*, 331.

(5) Pinet, O.; Hollebecque, J. F.; Hugon, I.; Debono, V.; Campayo, L.; Vallat, C.; Lemaitre, V. *Journal of Nuclear Materials* **2019**, *519*, 121.

(6) Vogel, H. *Phys. Z.* **1921**, *22*, 645

(7) Fulcher, G. S. *Journal of American Ceramics Society* **1925**, *8*, 339

(8) Tammann, G.; Hesse, W. *Z. Für Anorg. Allg. Chem.* **1926**, *156*, 245.

(9) Mauro, J. C.; Yue, Y.; Ellison, A. J.; Gupta, P. K.; Allan, D. C. *Proceedings of the National Academy of Sciences* **2009**, *106*, 19780.

(10) Avramov, I.; Milchev, A. *Journal of Non-Crystalline Solids* **1988**, *104*, 253.

(11) Yamashita, M.; Suzuki, M.; Yamanaka, H.; Takahashi, K. *Glass Science and Technology: Glastechnische Berichte* **2000**, *73*, 337.

(12) Doremus, R. H. *Journal of the American Ceramic Society* **1960**, *43*, 655.

(13) Beerkens, R. G. C. In *Advances in Fusion and Processing of Glass III*; John Wiley & Sons, Inc.: **2006**, p 1.

(14) Beerkens, R. G. C. *American Ceramic Society* **2003**, 3.

(15) Plessers, J.; Laimbock, P.; Faber, A. J.; Tonthat, T. *Ceramic Engineering and Science Proceedings* **1998**, *19*, 145.

Chapter 4

Single-Bubble Study

Chapitre 4

Étude d'une Bulle Unique

Résumé : Ce chapitre est dédié à l'étude du transfert de masse entre une bulle d'oxygène et le verre fondu simplifié (borosilicate + cérium). Cette étude est réalisée à l'aide de moyens expérimentaux et numériques, pour différentes teneurs en cérium (% Ce_2O_3) et différentes fugacités en oxygène (f_{O_2}). Dans un premier temps, nous présentons les échantillons et certaines de leurs propriétés. Par la suite, la méthode expérimentale pour observer l'évolution d'une bulle au sein d'une fonte verrière (observation par caméra *in-situ*) est décrite. Par ailleurs, un des modèles de transferts de masse, précédemment décrit dans le chapitre bibliographique, est rappelé. Les résultats expérimentaux et numériques confirment que le transfert de masse augmente de façon significative avec la réaction de réduction du cérium ainsi qu'avec la teneur en multivalent. Un modèle théorique considérant les réactions d'oxydo-réduction comme instantanées et une diffusion dominée par celle de l'oxygène permet de retrouver la plupart des résultats expérimentaux.

Chapter 4

Single-Bubble Study

This current chapter is dedicated to the study of a single-bubble in a cerium-doped borosilicate melt, at a constant temperature (T = 1150 °C), focusing mainly on the mass transfer between them. We have as goal here to validate this mass transfer model for our single-bubble melt system as well as the physical-chemical properties used in the calculations.

We aim to investigate in this chapter, by experimental and numerical means, the shrinkage of an oxygen bubble in the mentioned melt containing three different amounts of cerium (wt% $\mathrm{Ce_2O_3}$) at three different redox ratios ($\mathrm{Ce(III)/Ce_{total}}$). In this chapter, we first present a description of the samples, exhibiting how they are synthesized and the different redox ratios. Further, the experimental approach to observe bubbles at high-temperature (*in-situ* camera imaging technique) is described. The numerical calculations are, afterward, recalled, since the complete description is presented in chapter 2 (section 2.3.1), and a brief portrait of this model is given. Lastly, we present the experimental and numerical results of mass transfer between an oxygen rising bubble and the studied melt.

4.1 Samples

To study the mass transfer between an oxygen rising bubble and a borosilicate melt, a borosilicate glass composition doped with 0.5, 1.0 and 1.5 wt% of $\mathrm{Ce_2O_3}$, added in $\mathrm{CeO_2}$ form, is chosen. These cerium amounts are chosen based on the amount found in a nuclear waste glass, the cerium solubility limit and the transparence of the final glass.[1,2] This last factor is important due to the observation technique used in this part of the study – the camera *in-situ* technique. These glasses are pre-synthesized by mixing borosilicate glass beads, with size of ~1.5mm and surface ~ 50mm^2, with cerium-IV oxide powder ($\mathrm{CeO_2}$/Aldrich, > 99.9%). More information about these precursors, as well as the final composition of the glasses are displayed in chapter 3 (section 3.1).

Around 200 g of this mixed material is placed in a platinum crucible and pre-synthesized at different temperatures (1200, 1300 and 1400 °C), for different durations (90, 60 and 60 min), respectively. These temperatures are chosen in order to have three different redox ratios ($\mathrm{Ce(III)/Ce_{total}}$) as well as increase the temperature range used for camera imaging. The last temperature must be below the minimum pre-synthesis temperature to avoid bubble formation due to redox. These temperatures give rise to three different redox states, namely oxidized (O), intermediate (I) and reduced (R), respectively. The durations at each temperature are selected, considering the bubble rising velocity proposed Hadamard and Rybczynski[3,4] in order to have a bubbled-free melt at the end of the experiment and minimize volatilization. After being pre-synthesized, the aforementioned samples are split into two groups. The first half is used for camera imaging and the second used for subsequent analyses, such as potentiometry measurements to infer their redox states and scanning electron microscopy (SEM) analyses.

These potentiometry measurements are conducted to determine the oxygen fugacity values ($\mathrm{fo_2}$) imposed by the pre-synthesis temperature. These experiments are executed at the same temperature as the single-bubble observation (T = 1150 °C). This temperature is chosen based on three facts. Firstly, this temperature is within the temperature range of nuclear waste vitrification processes.[5] Besides, at this temperature, the melt has physical properties, which give a single-bubble residence time in the range of some minutes, in this way we avoid extremely short or long experiments.[3,4] Lastly, it is lower than the pre-synthesis temperature, avoiding in this way bubble formation during the single-bubble observation experiment. After obtaining these $\mathrm{f_{O_2}}$ values of the nine melts, the thermodynamic model, proposed by Pinet *et al.*,[1] is applied to determine the cerium speciation of the studied melts (optical basicity, Λ = 0.53). In this work, we also convert $\mathrm{f_{O_2}}$ into oxygen partial pressure ($\mathrm{P_{O_2}}$) in order to be able to use Henry's law and consequently apply the mass transfer code.[6] This conversion can be done if the gases are considered ideal and it has been done previously in the literature.[7,8]

Table 4.1 presents the nine melts, used in this research, which are named according to the redox states (O, I or R) and their $\mathrm{Ce_2O_3}$ wt% loadings. This table also contains the pre-synthesis temperature used to impose the redox state along with their respective log ($\mathrm{Po_2}$) and $\mathrm{Ce(III)}$ percentage values.

Table 4.1: P_{O_2} and the respective $Ce(III)$ percentage of each studied glass melt, at $1150\ °C$.

Glass melts (wt% Ce_2O_3)	Pre-synthesis temperatures (°C)	log (Po_2, atm) $\pm$ 0.1	% $Ce(III)$ (%)
O-0.5	1200	0.0	52.8
O-1.0	1200	0.1	52.4
O-1.5	1200	–0.1	54.2
I-0.5	1300	–0.7	62.5
I-1.0	1300	–0.6	61.2
I-1.5	1300	–0.8	63.9
R-0.5	1400	–1.2	69.3
R-1.0	1400	–1.1	67.7
R-1.5	1400	–1.3	70.5

As it can be seen in **Table 4.1**, the oxygen partial pressure is strongly controlled by the pre-synthesis temperature. The samples, containing different cerium loading, but pre-synthesized at the same temperature, have the roughly the same Po_2 value, as expected. By analyzing the samples using Energy-dispersive X-ray spectroscopy (EDS), it was observed that all these samples presented overall compositions consistent with the nominal ones. It means that all the added cerium was indeed incorporated into the glass matrix. However, in part of the samples of the O-group (synthesized at 1200 °C), it can be observed small regions enriched and depleted in cerium. For this specific study, in which bubble is moving and exchanging mass with different regions of the glass bath, these enriched and depleted areas do not cause a problem. In order to homogenize the molten glass, higher temperatures or longer melting durations could be applied.

4.2 Method to study a single-bubble

In this part, we present the methodology used to observe bubbles at high temperature. In the 1970s, Žlutický and Němec[9] started the development of an apparatus to observe glass melts, at high temperatures, especially during the fining process. Later, in this same research group, Němec and Kloužek [10] designed and setup a device, in which a single-bubble could be released in a transparent silica crucible, filled with molten glass, and the radius of the bubble (a) could be recorded with time, through camera imaging. Today, Glass Service® commercializes this type of equipment and the furnace along with the observation system cost around 130 K€. Besides bubble observation in molten glasses, other different studies can be carried out using this type of equipment, such as feed-to-glass conversion, feed volume expansion and reactivity of glasses during nuclear waste vitrification.[11,12]

Likewise, using this equipment, one could be able to execute experiments such as *in-situ* optical dilatometry and observation of insoluble particles, depending on the total amount.

This type of equipment is a well-established technique, which has been vastly used in glass science, especially for bubble observation.[8,13,14] This apparatus consists of an electrical furnace coupled with a porthole, which geometrically links the glass melt sample to the charge-coupled device (CDD) in the camera (**Figure 4.1**). Glass pieces (~50 g) are beforehand, placed in a transparent crucible (height H = 65mm, depth, K = 15 mm, and width, L = 35 mm), which is displayed in **Figure 4.2**. This assembled apparatus is placed then in the observation furnace, which is already heated at the bubble study temperature (T = 1150 °C). After melting the glass sample (~180 s), a silica tube, connected to an oxygen gas cylinder, is introduced in the melt. Pigeonneau *et al.*[8] calculated, for a similar system, the silica diffusion, from the silica tube to the melt, and it can be neglected. The temperature around the sample was monitored with a thermocouple and the thermal inhomogeneity did not exceed 5 °C.

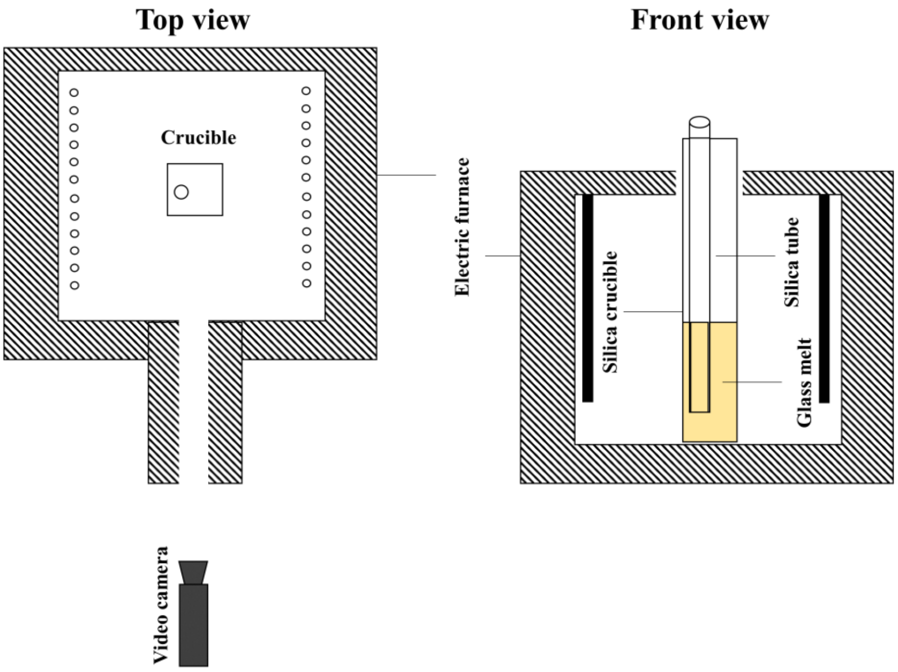

Figure 4.1: Scheme of the top and front views of the high-temperature *in-situ* observation apparatus.

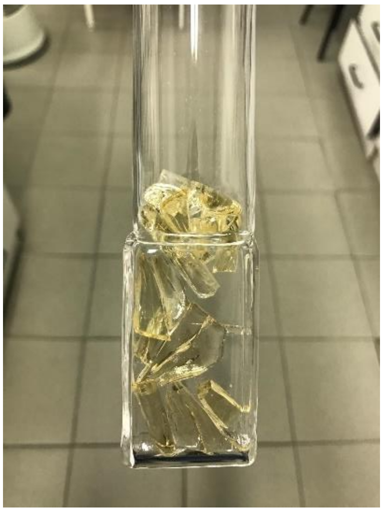

Figure 4.2: Glass samples placed in a silica crucible just before being place in the *in-situ* observation apparatus.

At the completion of the experimental setup, an oxygen bubble is inflated and injected into the glass melt through the silica tube. The tube is kept in the melt to avoid fluid turbulence during its removal procedure. In this research, the initial bubble radii $(\mathrm{a_0})$ varied from 0.3 to 1.6 mm. After releasing the bubble, it rises because of the buoyancy in the crucible and the radius is monitored over time, by camera recordings. An example of output image from these records is exhibited in **Figure 4.3**. In this figure, we can see the studied bubble rising freely in the right, the silica tube filled up to a certain point with oxygen gas and some small bubble attached to the crucible wall. As the studied single-bubble does not interact neither with the crucible nor with the attached bubbles, they do not disturb this current mass transfer study.

In this investigation, the injected oxygen bubble rise freely, up to the melt surface, where it escapes from the melt. The residence time of the bubble is strongly affected by its radius and the melt viscosity.[3,4] Due to the fact that bubbles escape from the melt, the observation time here is reduced and in this study, we observe bubbles up to 10 minutes of experiment. For each melt situation, five different bubbles are produced and the total experimental time is around 2 h.

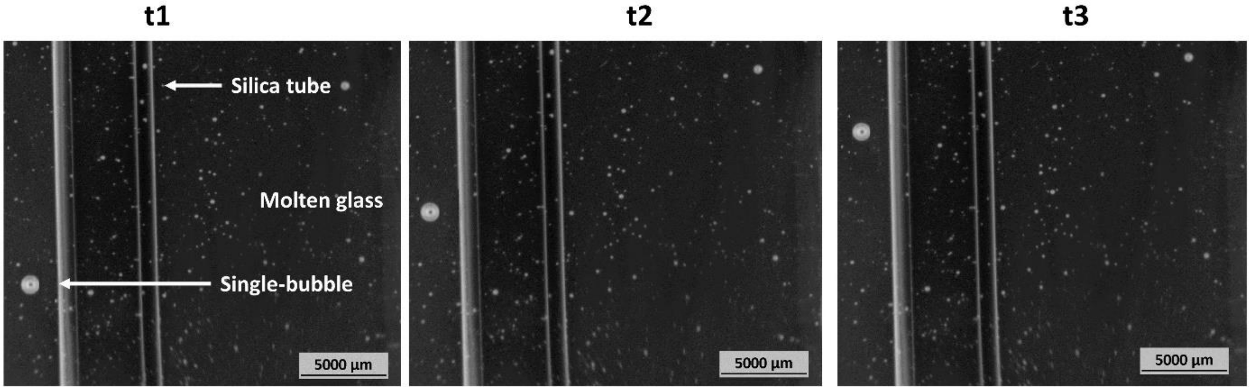

Figure 4.3: Example of an image acquired by *in-situ* camera observation technique showing the rising bubble for three different durations of experiment (t1, t2 and t3).

Bubble radius is recorded and computed using the LUCIA imaging software. Afterward, the obtained images are treated with the NIS-Elements® software (Laboratory Imaging, Czech Republic), by counting the number of pixels, representing the bubble, and comparing them to a known object, which had been previously employed for calibration (silica tube, in the current case). Since we are studying just one bubble at time, no image treatment automation is needed. The uncertainties of radius are equal to one pixel and consequently, the absolute uncertainty is 20 μm.

The aforementioned experiments were carried out by myself, under Jaroslav Kloužek supervision, during my training period (January 2020) at the University Chemistry Technology (UCT) Prague, Czech Republic. This was the result of a collaboration between CEA Marcoule and UCT Prague.

4.3 Mass transfer modeling of the multicomponent bubble

Besides by the mentioned experimental approach, we also investigate, by numerical calculations, how bubble radius evolves in different melts. This numerical model, developed by Pigeonneau,[6] takes into consideration the mass transfer phenomenon between a freely rising bubble immersed in a molten glass with $\mathrm{N_g}$ gaseous species and having chemical equilibria well defined. Details of this mass transfer model is already presented in chapter 2 of this PhD manuscript (2.3.1), but in this section, we portray it, describing the main scientific considerations. Afterward, we detail the utilization of the code, in practical ways.

Due to the difference of gas concentration on the bubble surface and dissolved in the melt, mass transfer, through diffusion, tends to take place in order to decrease this difference and consequently decrease the Gibbs free energy of the system.[15,16] This mathematical model considers bubble ascension by considering its terminal rising velocity. This velocity is found as the solution of a balance of forces (buoyancy and drag). For molten glasses, two main solutions have been proposed in the literature: the Stokes and Hadamard-Rybczynski.[3,4] Hornyak *et al.*[17] tested, experimentally, these two solutions, considering bubbles rising in a soda-lime silicate melt at 1200 °C. It is concluded, by this latter work, that the steady-state buoyant rise of a gas inclusion in silicate melts follows Hadamard-Rybczynski.[3,4] This is in agreement with bubble ascension in borate melts as well.[18] Hornyak *et al.*[17] suggests that the non-agreement with Hadamard-Rybczynski[3,4] solution might be related to impurities in the glass melt. It is important to mention that, since mass transfer is taking place, bubble radius changes throughout the experiment and as consequence, the bubble terminal rising velocity also does.

This model also considers the presence of more than one gaseous species. More specifically, it considers three species: $\mathrm{O_2}$, $\mathrm{N_2}$ and $\mathrm{CO_2}$. The former, in the presence of a multivalent element, is considered as finning gas, while the two latter ones are non-finning species. In the model, these two types of gases are treated differently. While for a finning gases, we use the "modified Péclet number" ($\mathrm{Pe_i'}$), for a non-fining species, we use the Péclet number ($\mathrm{Pe_i}$). Briefly, "modified Péclet number", is a dimensionless number that takes into consideration the influence of multivalent elements, through redox reactions, on mass transfer. The related redox reaction is considered in equilibrium in the numerical calculations used in this PhD work.

Practically, the numerical model is fed with the melt properties, as well as with the bubble characteristics at the initial time ($\mathrm{t} = 0$). The former one is composed by the redox state of the melt, previously reached by potentiometry measurements, as well as the physical properties described in chapter 3. The latter one is mainly composed by the initial bubble composition ($\mathrm{O_2}$) and by the initial bubble radius.

4.4 Results

This section contains both experimental and numerical results. We first present the studied region, in terms of time, showing that long experiments are limited due to the crucible height. Afterward, we present a general overview of all the studied samples. A typical plot of bubble shrinkage rate as function of the initial bubble size is presented and a physical and a mathematical explanations are given. Subsequently, a comparison of two numerical models is presented in order to show the importance of taking the redox reactions into consideration as well as the use of the "modified Péclet number" in the model. Lastly, we master the bubble shrinkage behavior by normalizing the experimental data using a characteristic time for mass transfer.

4.4.1 Studied region

Because of the limitation of the molten glass height (H), due to the crucible height (65mm), along with the applied experimental methodology, the studied region is based on ~10 min of observation. **Figure 4.4** shows the numerical and experimental results of one bubble, immersed in R-1.0 glass melt. It is necessary to emphasize that the experimental data ceases when the studied bubble escapes from the molten glass. At the initial stages, the bubble size decreased, almost linearly with time, on both the experimental and numerical data and in this current research, we are focused on this mentioned region.

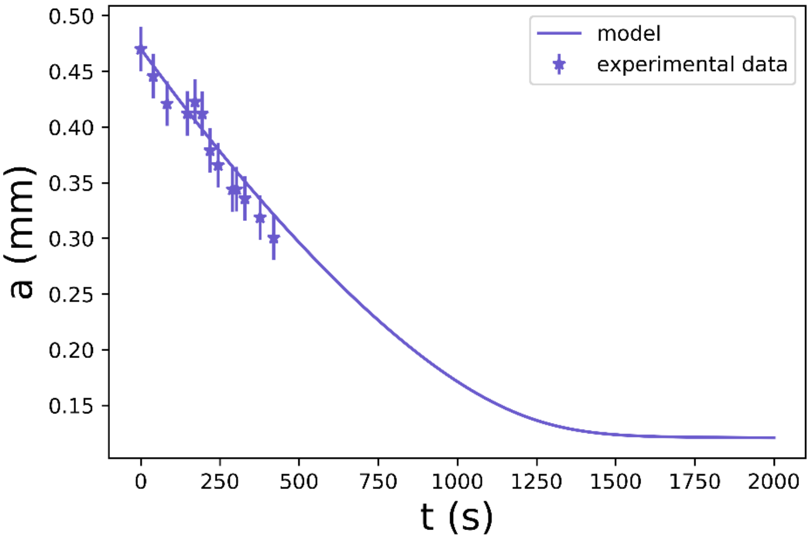

Figure 4.4: Numerical and experimental results of a bubble, which was immersed in an R-1.0 glass melt, to demonstrate the studied region for ~10 min.

4.4.2 General overview of bubble size versus time

Taking this studied region into consideration, **Figure 4.5** displays an overview of oxygen bubble size, as a function of time, for the nine different melts, at $T = 1150$ °C. Five bubbles are investigated for each of them. The symbols represent the experimental results, while the continuous lines represent the results obtained by numerical computations. Considering the isolated experimental data, it can be confirmed that increasing the redox ratio of the molten glass, bubble shrinkage rate (da/dt) is enhanced. This can be explained by the increase in the driving force of oxygen mass transfer, which is the difference between the oxygen concentration on the bubble and its concentration in the molten glass ($C_{O_2}^{s}$ and $C_{O_2}^{\infty}$). Hence, the bubbles in O-melts hardly shrink while the others, shrink more readily. This enhancement is also observed in terms of the cerium content of the melt. The melts, with high cerium contents, demonstrate higher exchange rates, compared to those with low cerium contents. Qualitatively, $Ce(III)$ can be considered, in our case, as an oxygen sinkhole. It consumes oxygen from the bubble and facilitate its absorption. These influences are better explained through mathematical means in the following paragraphs.

The O-group samples, shown in **Figure 4.5**, as A), B), and C), exhibit log $(\mathrm{Po_2})$ ~ 0. For these samples, it is noticeable that the numerical simulation does not adequately represent their bubble shrinkage behavior with time. This mismatch is due to the proximity of the $\mathrm{Po_2}$ of the melt to the $\mathrm{Po_2}$ of the bubble, which the natural logarithmic value is zero (since it is initially composed of pure oxygen). In this way, oxygen concentrations in both of them are really similar and slight variations of $\mathrm{Po_2}$, experimentally measured by potentiometry technique, may completely distort the numerical output of the bubble evolution, thereby resulting in its growth instead of its shrinkage.

Still analyzing **Figure 4.5,** with the exception of the O-samples, the numerical computations applied to I- and R-melts adequately estimates their mass transfer processes and bubble shrinkage rates. Thus, the mathematical law, along with the considered model fits adequately the experimental results. Indeed, a comparison of the correlation coefficient (R^2), obtained from the linear regression of both the numerical and experimental data, confirmed that all the investigated bubbles, in the I- and R-melts, exhibited $\mathrm{R}^2 > 0.95$.

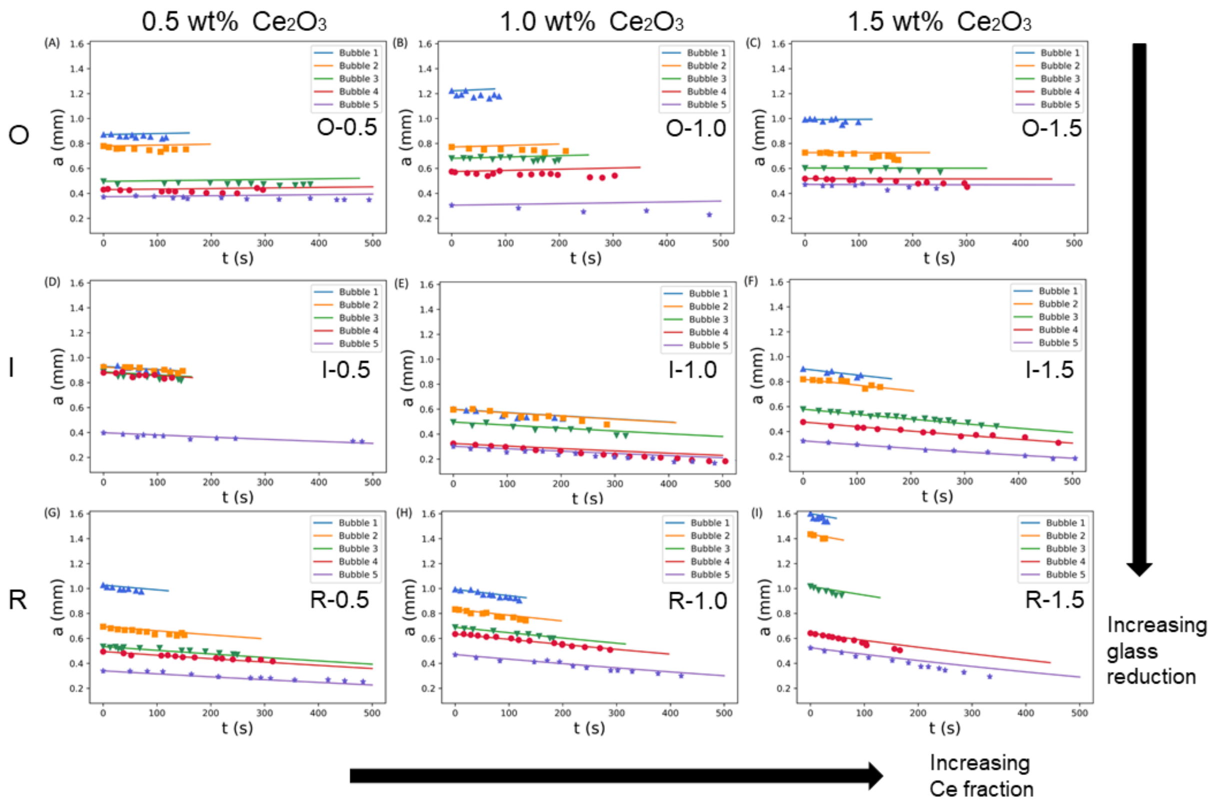

Figure 4.5: Oxygen bubble radius (a) as a function of time for the nine studied melts. A) O-0.5, B) O-1.0, C) O-1.5, D) I-0.5, E) I-1.0, F) I-1.5, G) R-0.5, H) R-1.0, and I) R-1.5 wt% Ce_2O_3. Symbols are the experimental results and continuous lines are the numerical simulation ones.

4.4.3 Shrinkage rate

Figure 4.6 exhibits an example of shrinkage rate (da/dt), as a function of the initial radius (a_o). The values are obtained from the studied region (for up to 10 minutes of the experiment) and da/dt is constant in this domain. Since, in the initial stages, the gas concentration difference between the bubble surface and the bulk melt is almost constant over time, the mass exchange between them is also constant, giving rise then to a constant shrinkage rate. However, for long durations, this concentration difference may get small and the mass transfer would drop, flattening then the curve (radius versus time plot) at the end. Nevertheless, it is worth mentioning that, experimentally, we have not observed this mentioned behavior because bubbles escape before this flattening stage.

Figure 4.6 is obtained by plotting the slope (da/dt) versus the interception (a_o) of each of the bubbles previously presented. It is obtained by linear regression of both experimental (symbols) and theoretical (continuous line) data. For the experimental data, it is interesting to note that the presence of large bubbles generally results in an increased margin for error, because large bubbles exhibit lower residence time and consequently lower the amount of experimental data. By observing **Figure 4.5** along with **Figure 4.6**, it can be verified that, for the same melt and initial composition of the bubble, the initial bubble radius determines da/dt, which is constant with time, in the studied region.

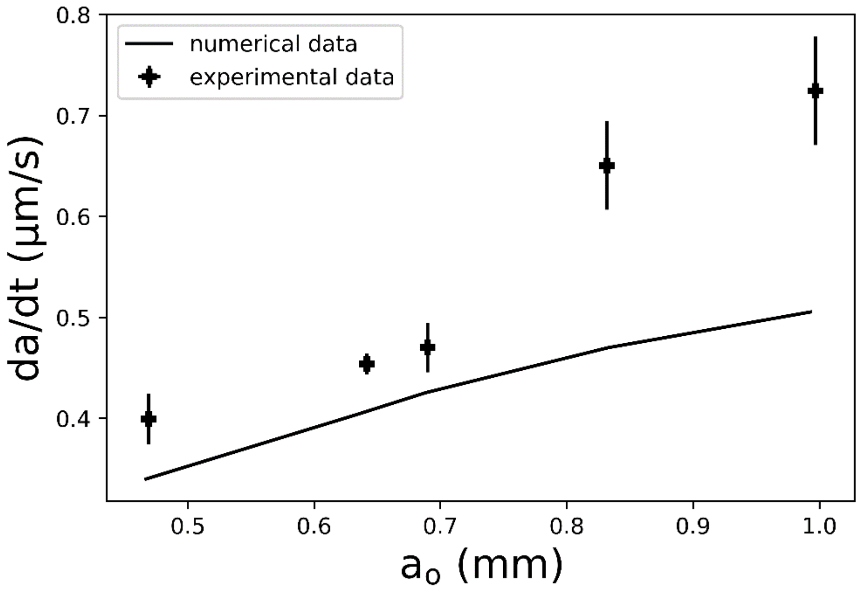

Figure 4.6: Bubble shrinkage rate (da/dt) as a function of the initial bubble size (a_o) for sample R-1.0 wt% Ce_2O_3.

Large bubbles will generally shrink faster than smaller ones, under freely rising conditions.[8] By increasing the initial radius, terminal rise velocity is also enhanced, and this contributes to the decrease of chemical boundary layer thickness around the rising bubble, which in turn, enhances the mass transfer because gas concentration varies more intensely. **Figure 4.7** illustrates this previous idea by showing two bubble situations, obtained by finite element simulation. The bubble displayed in A) is a quasi-static one (Pe <<1), in which diffusive regime is predominant. The second bubble, exhibited in B), is a rising bubble (Pe >>1), in which convective regime is dominating. By analyzing the difference of colors, one can notice that oxygen concentration varies from red (more concentrated) to blue (less concentrated). This variation, in more intense for the case of the rising bubble (B). Then, it explains the higher mass transfer intensity (da/dt) for larger radius, because it has higher rising velocities and consequently higher Péclet number. This figure is not part of this current work and is done based on the data and ideas published by Pigeonneau *et al.*[19] Mathematically, it can be quantified through the increment of Pe, which enhances mass transfer through the increase of Sh_i.[6]

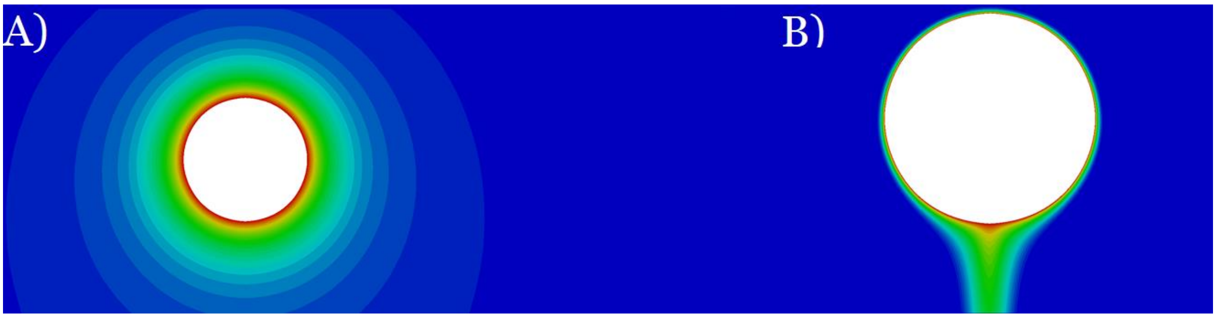

Figure 4.7: O_2 concentration around a rising bubble obtained by solving advection-diffusion-reaction equation with a finite element method. A) Diffusive regime occurring at small rising velocity, *i.e.* Pe<<1; B) Convective regime for large rising velocity, *i.e.* Pe>>1.

4.4.4 Enhancing the mathematical model

In this work, as experimentally shown, mass transfer between the rising bubble and the melt, in the presence of a multivalent element, is enhanced.[6,8] **Figure 4.8** shows the acquired experimental data (stars), along with two different numerical models (continuous lines). Model A does not consider that the multivalent element enhanced the mass transfer. It, therefore, considers all gases, as non-fining species and thus considered Pe in the theoretical calculations. Conversely, model B, which is the current model adopted in this study, considers molecular oxygen, as a fining gas, which, therefore adopts Pe_i' in the calculations. Hence, it enhances Sh_i, which in turn, enhances mass transfer. It can be clearly seen in **Figure 4.8** that model B estimates within the experimental error while model A underestimated the magnitude of mass transfer. It is important to emphasize that similar behaviors are also observed in the I- and R-melts, demonstrating then that the utilization of Pe_i' must be taken into consideration. Pe_i' considers the redox state of the glass melt, which is quantified by the concentration of the physically dissolved oxygen which is in equilibrium with the multivalent elements in the melt (in this case, cerium). The bubble shrinking rate is increased with increasing redox ratio.

Thence, by observing the radius evolution, acquired experimentally with time, and by considering the two numerical models, it is important to note that the increase in the cerium content increases the mass transfer coefficient in the borosilicate melt system, just as iron oxide can achieve in a silicate melt. It is demonstrated, therefore, that the application of Pe_i', proposed by Pigeonneau[6], adequately estimated the bubble shrinkage in a different melt system, doped with a different multivalent element.

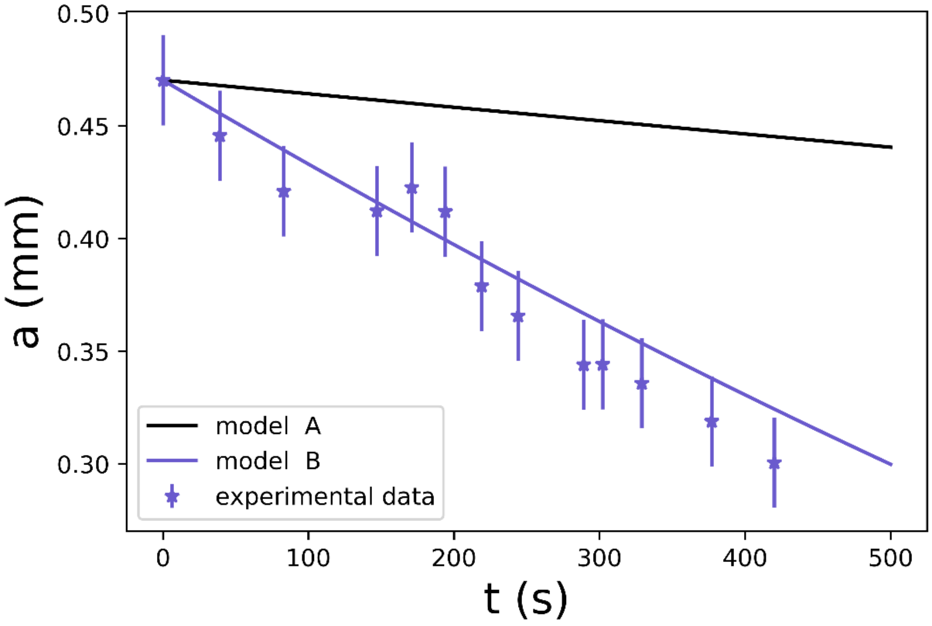

Figure 4.8: Bubble radius as a function of time, obtained experimentally and by two numerical models: A and B. The former considers Péclet number and latter considers the modified Péclet number. The displayed results are obtained from bubble 5, immersed in the sample, R-1.0 wt% Ce_2O_3.

Therefore, because the mass transfer code well estimates the experimental data, for the O and R-melts, we can conclude also that the physical properties taken from the literature, such as diffusivity and solubility, are adapted to our melt system. Likewise, the use of this numerical model is validated, allowing us to apply this numerical model to a bubble population system, as it is presented in the following section (5.4.2).

4.4.5 Normalization of experimental data

The normalization of a single-bubble behavior, according to Pigeonneau,[7] enabled us to define the characteristic time for mass transfer (τ) as follows:

$$\tau = \frac{2a_0^2}{Sh_{O_2}(Pe'_{O_2,0})D_{O_2}L_{O_2}RT}. \tag{4.1}$$

Where a_0 is the initial bubble radius; Sh_{O_2} is the Sherwood number, which is a function of Pe'_i under the initial condition, and the product, $D_{O_2}L_{O_2}RT$, is the oxygen permeability.

τ considers the mass transfer, by advection, but also considers the redox reaction of cerium. This characteristic time for the nine melts, possessing three different amounts of Ce_2O_3, and three different redox states are computed for a typical initial radius of 1 mm. **Table 4.2** summarizes the values of τ, in h, for these nine samples. As expected, τ decreases when the amount of cerium increases. Moreover, R-melts exhibited a shrinkage time scale, which is shorter than that of the O groups.

Table 4.2: Characteristic time of mass transfer (τ) in hours, given by equation (4.1) for the studied samples.

Redox state/ Ce_2O_3 loading	**Glass + 0.5 wt% Ce_2O_3**	**Glass + 1.0 wt% Ce_2O_3**	**Glass + 1.5 wt% Ce_2O_3**
O	3.24	2.34	1.76
I	2.27	1.62	1.26
R	1.92	1.40	1.08

The dimensionless shrinkage rate $\mathrm{d}\bar{a}/\mathrm{d}t$ was defined by Pigeonneau[7] and is given by:

$$\frac{\mathrm{d}\bar{a}}{\mathrm{d}\bar{t}} = -\frac{1}{\bar{a}}\sum_{i=1}^{N_g} \frac{\overline{Sh_i}}{\overline{\tau_i}}\left(x_i - Sa_{i,0}\right), \tag{4.2}$$

where the bars, over the variables, indicate that they are dimensionless. The driving force, for the bubble evolution over time, is determined by the difference of the molar fraction (x_i) and the saturation state ($Sa_{i,0}$) of each gaseous species. To solve this equation, the exchange rate of each species is also required.[7] This development is not detailed in the present work. Nevertheless, it should be noted that since advection and redox reaction facilitated the mass transfer, Sh_i is expected to behave as a function of $(\bar{a})^{3/2}$. Reporting this estimation in Eq. (4.2), for short durations, $\sqrt{\bar{a}}$ should behave as follows:

$$\sqrt{\bar{a}} = 1 - \beta\,\bar{t}, \tag{4.3}$$

where β is the integration constant.

Figure 4.9 assembles all the data collected experimentally in this work. The square root of the dimensionless radius ($\sqrt{\bar{a}}$) is plotted, as a function of the dimensionless time ($\bar{t}$), which is obtained by dividing the experimental time (t) by τ. A unique behavior appears clearly: the data are largely scattered, even after a long time. The solid line is a fitted curve, corresponding to Eq. (4.3) with $\beta' = 1.25$, found by numerical fit. This result demonstrates the relevance of considering the role of redox reaction in mass transfer. It is relevant to emphasize that bubble radius, evolving over time, as aforementioned, is a feature of the mass transfer processes in the presence of advection.

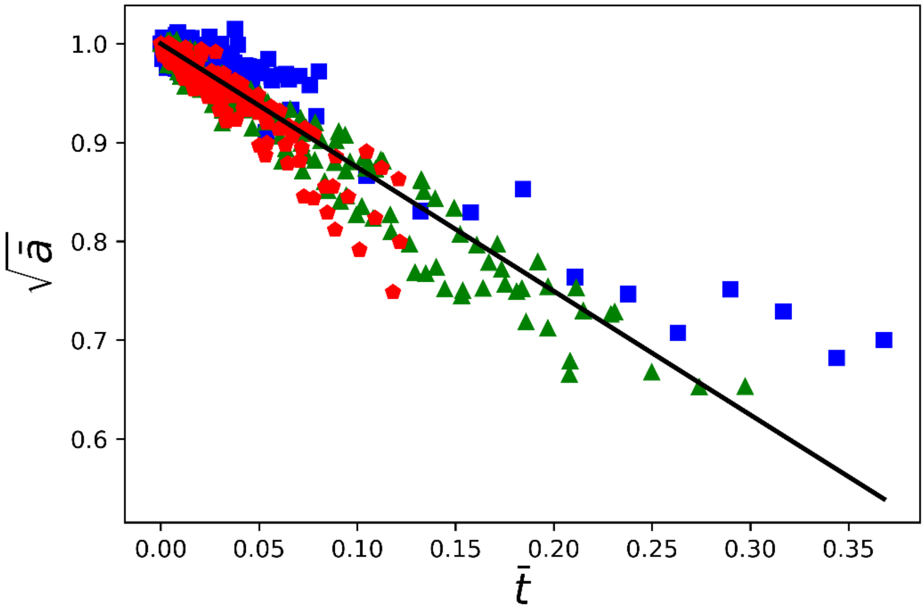

Figure 4.9: $\sqrt{\bar{\mathbf{a}}}$, as a function of $\bar{\mathbf{t}}$, is obtained for all the experiments with the nine glass samples. The blue squares, green triangles and red pentagons correspond, respectively, to the results obtained for the O-,I- and R-melts.

4.5 Conclusion

This chapter was dedicated to the study of a simplified glass melt system, doped with cerium oxide, and composed by just one oxygen bubble. We investigated, by experimental and computational modeling, the mass transfer between a freely-rising bubble and the borosilicate melt. Experimentally, the data were obtained by *in-situ* camera imaging, while the numerical calculations are proposed by Pigeonneau's model[6] and described in the bibliographic chapter 2 (section 2.3.1). This research was carried out at a constant temperature and nine different scenarios, for varying cerium contents and speciations. We validated the use of this model for this current melt system for most of the studied samples. An explanation for the ones, which it does not well estimate, is presented and it is based on the similar values of oxygen partial pressure in the bubble and in the bulk melt. The influence and importance of initial radius were presented and an explanation was given based on the increment of Sherwood number, which can also be seen as a decrease of the chemical boundary layer around the rising bubble. Moreover, we confirmed the application of the "modified Péclet number" to model the mass transfer between an oxygen bubble and the borosilicate melt, in a presence of fining gases and redox reactions. Finally, a normalization of the experimental results using a characteristic time for mass transfer was performed and a general behavior was confirmed.

Thus, important insights were obtained in this chapter and we could also validate the use of the numerical model of mass transfer to simulate bubble shrinkage in a borosilicate melt, in some specific situations. We also concluded that the melt/gas properties extracted from the literature, such as gas diffusivity and solubility are coherent with the studied case. It allow us, therefore, to enlarge this computer modeling study to a bubble population scenario, which is one of the topic of the following chapter.

4.6 References

(1) Pinet, O.; Phalippou, J.; Di Nardo, C. *Journal of Non-Crystalline Solids* **2006**, *352*, 5382.

(2) Cachia, J. N.; Deschanels, X.; Den Auwer, C.; Pinet, O.; Phalippou, J.; Hennig, C.; Scheinost, A. *Journal of Nuclear Materials* **2006**, *352*, 182.

(3) Hadamard, J. S. *Compt. Rend. Acad. Sci.* **1911**, *152*, 1735.

(4) Rybczynski, W. *Bull. Acad. Sci.* **1911**, *A*, 40.

(5) Vernaz, E.; Gin, S.; C, V.; Elsevier: Amsterdam, **2012**; Vol. 5, p 451.

(6) Pigeonneau, F. *Chemical Engineering Science* **2009**, *64*, 3120.

(7) Pigeonneau, F. *International Journal of Heat and Mass Transfer* **2011**, *54*, 1448.

(8) Pigeonneau, F.; Martin, D.; Mario, O. *Chemical Engineering Science* **2010**, *65*, 3158.

(9) Zluticky, J.; Nemec, L. *Glastech Ber* **1977**, *50*, 57.

(10) Kloužek, J.; Němec, L. *Ceramics - Silikaty* **2003**, *47*, 155.

(11) Pokorný, R.; Hrma, P.; Lee, S.; Klouzek, J.; Choudhary, M. K.; Kruger, A. A. *Journal of the American Ceramic Society* **2020**, *103*, 701.

(12) Hujova, M.; Pokorny, R.; Klouzek, J.; Lee, S.; Traverso, J. J.; Schweiger, M. J.; Kruger, A. A.; Hrma, P. *International Journal of Applied Glass Science* **2018**, *9*, 487.

(13) Vernerová, M.; Němec, L.; Kloužek, J.; Hujová, M. *Journal of Non-Crystalline Solids* **2018**, *500*, 158.

(14) Vernerova, M.; Cincibusova, P.; Klouzek, J.; Maehara, T.; Nemec, L. *Journal of Non-Crystalline Solids* **2015**, *411*, 59.

(15) Jones, S. F.; Evans, G. M.; Galvin, K. P. *Advances in Colloid and Interface Science* **1999**, *80*, 27.

(16) Cussler, E. L. *Diffusion: Mass Transfer in Fluid Systems*; 3 ed.; Cambridge University Press: Cambridge, **2009**.

(17) Hornyak, E. J.; Weinberg, M. C. *Journal of the American Ceramic Society* **1984**, *67*, c244.

(18) Jucha, R. B.; Powers, D.; McNeil, T.; Subramanian, R. S.; Cole, R. *Journal of the American Ceramic Society* **1982**, *65*, 289.

(19) Pigeonneau, F.; Perrodin, M.; Climent, E. *Aiche Journal* **2014**, *60*, 3376.

Chapter 5

Bubble Population Study

Chapitre 5

Étude d’une Population de Bulles

Résumé : Ce chapitre est consacré à l’étude d’une population de bulles dans le verre fondu d’intérêt (borosilicaté + cérium). Cette étude est également réalisée à l’aide de moyens à la fois expérimentaux et numériques. Dans un premier temps, nous présentons les échantillons et leurs caractéristiques ainsi que la méthode expérimentale pour observer les bulles (microscopie *post-mortem*). L’adaptation du modèle numérique d’une seule bulle à une population de bulles est alors décrite. Les résultats expérimentaux montrent qu’en faisant fondre un milieu granulaire, constitué de grains de verre, la nucléation des bulles se déroule principalement d’une façon non classique et est liée à l'emprisonnement de l'air entre les grains. En considérant que la dynamique des bulles est pilotée par leurs temps de résidence dans le creuset, le comportement des bulles à différentes températures se révèle équivalent. Le modèle numérique basé sur le simple transfert de masse ne permet pas d'estimer le comportement des bulles, aussi la coalescence des bulles devrait-elle être prise en compte.

Chapter 5

Bubble Population Study

After investigating the mass transfer of a simplified melt system that contains just an oxygen single-bubble, we expand the system to a bubble population scenario. We have studied, experimentally and numerically, how an oxygen single-bubble exchanges mass with the studied borosilicate melt. Now, we aim to study a more complex system, in which we are able to study the bubble formation, the dynamic of these formed bubbles and the major growth mechanism. Here, we study a simplified nuclear waste glass melt, focusing on the interaction of a multivalent element (cerium) with a borosilicate glass frit, at different isothermal scenarios.

In this chapter, we first present the studied samples, detailing how they are synthesized along with the experimental approach to observe bubbles: the *post-mortem* optical microscopic technique. Afterward, we present the numerical computations and the modifications used to expand this model, previously used for the single-bubble system, to a bubble population scenario. In this computational simulation section, we use the initial experimental sample along with physical-chemical properties of the melt as input for the calculations. We present the experimental results, which contains some specific characterizations of the bubbled-glass system, such as cerium speciation and bubble composition as well as some bubble features, obtained by optical microscopy. Lastly, the numerical results are presented and compared to the experimental ones. A conclusion with the insights acquired herein and the limitations of the experimental procedure and numerical approach are presented at the end.

5.1 Samples

To study a population of bubbles in this thesis context, a simplified system composed by a borosilicate glass powder (250 – 500 μm) doped with 0.1 wt% of Ce_2O_3, added as CeO_2 powder (< 5 μm), is chosen. This latter is lower than the amount in a typical nuclear waste glass and is chosen to have a reasonable bubble density and size, avoiding bubble percolation and allowing us to execute the study. The final glass composition as well as the particle size distribution of the precursors are presented in chapter 3 (section 3.1). In the current section, we present the synthesis procedure along with the sample preparation. Differently from the single-bubble investigation, here, we do not vary cerium content, since bubble population study is a laborious and time-consuming task.

For each sample, 20 g of glass are synthesized. The borosilicate glass powder is initially mixed, mechanically, with cerium-IV oxide and then both are placed in a cylindrical alumina crucible (CeraQuest AC20 material AF997), which has chemical purity above 99.5 %. The crucible has an outer diameter, a height, and a wall thickness equal to 30, 40, and 2 mm respectively. The samples are introduced to the previously heated furnace and are melted at different isothermal situations (900, 950, 1000, 1050, and 1100 °C), for different durations (*e.g.* 20, 30, 40, 60, 120, and 240 min). This first residence time (20 min) was previously selected based on the thermal equilibrium time (~3 min). This latter duration was empirically obtained using a thermocouple in a similar system.

The samples are subsequently removed from the furnace and are allowed to cool down to room temperature in the air. During this cooling stage, bubble motion can be neglected. In order to illustrate this previous statement, we take a bubble of radius a = 100 μm and a temperature T = 800 °C. This temperature is around the middle temperature between T_g (531 °C) and the maximum studied temperature (1100 °C). Thus, this bubble would take around 250 h to rise a glass melt column of 20 mm height.[1,2] The melt system takes, on the other hand, less than 2 min to cool down from 1100 to 800 °C,[3] proving that bubble motion can be ignored during this cooling stage.

However, even having a really low mobility during the cooling stage, bubbles might change their size during this cooling step. Indeed, it would affect then bubble mean diameter and bubble fraction. These contraction/expansion phenomenon is outlined in chapter 6 (section 6.3).

Figure 5.1 displays the sample after the cooling procedure. The samples are filled with epoxy resin (in red) and are cut into two halves. The first half is mounted in epoxy resin and polished for optical microscopy imaging and the second one is used for subsequent characterizations, such as XANES and mass spectroscopies, to reach respectively cerium speciation and gas composition.

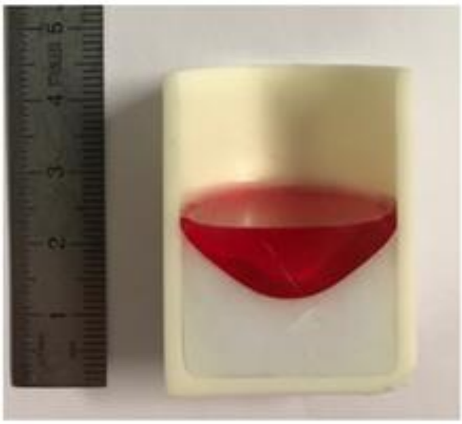

Figure 5.1: Half of a cut crucible containing the bubbled-glass (white) and the epoxy resin (red). Sample synthesized at 1000 °C during 20 min.

5.2 Method to study a population of bubbles

Volcanologists have applied microscopic techniques to observe bubbles on a cross-sectional area of solidified magmas.[4-6] Similarly to them, crystallization in glasses and supercooled liquids has also been investigated for several years by microscopic technique.[7,8] In this PhD work, *post-mortem* optical microscopic technique is applied to observe bubbles on the surface of the cut glass. Zeiss AXIO coupled with Axiocam 305 color high speed camera is used to rebuild the whole cross-sectional area of the sample by mapping technique. This procedure is based on an assembly of 144 images, overlapping them in a way to rebuild the aimed surface. The image scale is obtained from a known distance in the image. Each micrometer of the acquired images has 0.277 pixels, thus the resolution of the images obtained by this technique in this study is around 3.6 μm, which is in agreement with the ones mentioned in the literature.[9] **Figure 5.2** presents an example of image acquired by this previous methodology for the sample synthesized at 1000 °C during 20 min.

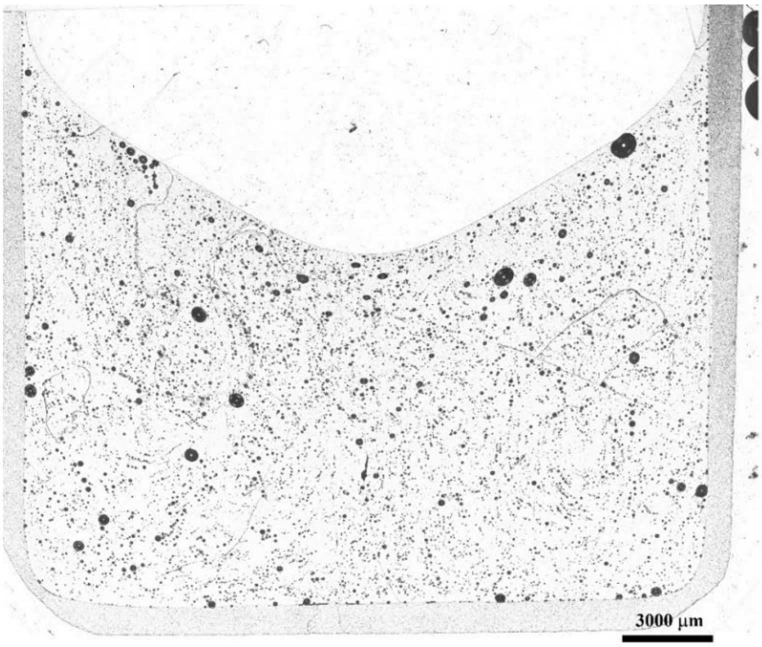

Figure 5.2: Example of a rebuilt image acquired by *post-mortem* optical microscopy. Sample synthesized at 1000 °C during 20 min.

Acquired images are treated using NIH (National Institute of Health) software to obtain the number of bubbles in a cross-sectional area, the cross-sectional area itself and a list of all bubbles' diameter. We detail below the sequence of operations used to carry out the image treatment used in this work.

- Defining the scale based on the known distance previously obtained: Analyze > Set scale > Set value as 0.277 pixels/μm,
- Enhancing the contrast between bubble and matrix: Process > Enhance contrast > Set value as 0.4 %,
- Turn it into binary: Process > Binary > Make it binary,
- Removing manually the crucible edges, cracks, noises and pixels connecting the bubbles. Close manually the bubbles that are not closed in the previous step,
- Fulfilling bubbles: Process > Binary > Fill Holes
- Analyze particles: Analyze > Analyze particles:
  - Bubble area: 706.858 μm^2 – infinity (corresponding to a diameter of 30 μm to infinity).
  - Circularity: 0.2 – 1.0 (allowing to take sufficiently spherical particles)

The aforementioned procedure takes into consideration bubbles larger than 30 μm of diameter. This value is equal to around ten times the resolution of the optical microscope in these working conditions.

Now that we have all the bubble diameters and the surface occupied by them, in relation to the total image area, we can reach the occupied area by bubbles in the crucible, what is called here “bubble surface fraction”. To reach this feature, we fulfill just the crucible, as an enormous black particle, and its total area is measured. Then the bubble surface fraction on the crucible surface is obtained by proportionality. Each measurement at 1000 °C has been replicated five times, in five different cross-sectional areas, in order to validate the good reproducibility of the procedure and to have the standard errors related to the measurement.

Figure 5.3 displays the same image of the previous example, but after the mentioned image treatment. This treatment output contains a list of all considered bubbles with their respective diameter, as well as the total area of the crucible. Therefore, using these previous data, one can obtain different bubble features; such as 2D bubble mean density ($\langle N_b^{2D} \rangle$), which is defined as the number of bubbles on the observed cross-sectional area of the material, 2D bubble mean diameter ($\langle d^{2D} \rangle$), which is the mean diameter of the studied population of bubble and bubble surface fraction or 2D bubble fraction (ϕ_b^{2D}), which is defined as the fraction of the observed area occupied by bubbles.

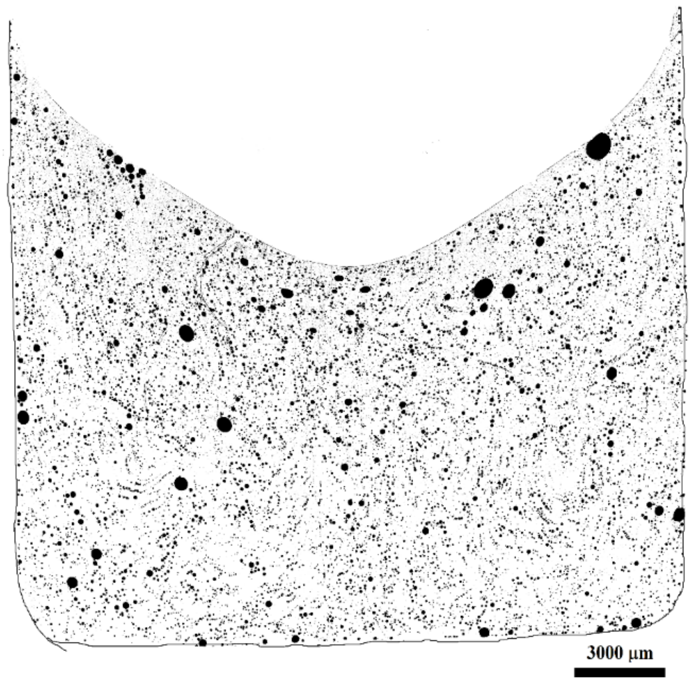

Figure 5.3: Example of a treated image acquired by *post-mortem* optical microscopy and treated by NIH. Sample synthesized at 1000 °C during 20 min.

It is important to highlight that using this experimental methodology, we analyze a two-dimension (2D) space, giving an output of the same dimension. For some works, the 2D bubble features are enough and there is no need to do a 3D estimation. However, in certain researches, the conversion is necessary and it can be done through stereological techniques.[10-12]

Bubble population, in this work, has also been investigated by scanning electron microscopy (SEM). Due to the considerable saving of time during image acquisition along with a much easier image treatment procedure, we adopted the optical microscopic technique to study a bubble population in this thesis. Although this saving of time comes at the expense of a loss of quality of the images, this quality remains sufficient for our study. Even saving time when compared to SEM procedure, optical microscopic technique is still considered a laborious methodology to study bubbles in glasses when compared to others.

Optical microscopic approach would have some discrepancies with the reality as well. In the chapter 6, we outline some of them when we compare this technique with other techniques to study bubbles in glasses and melts. The first is related to the material contraction/expansion during the cooling stage and the second related to the type of image acquired using optical microscopic approach. However, even having these two drawbacks, the use of this technique is plausible and sufficient for this current study.

5.3 Mass transfer modeling – adaptation to a bubble population scenario

After acquiring the experimental data for the bubbled-melt (800 – 1200 °C), we aim here to model some bubble features as well as the thermodynamic state of the melt. As shown in the chapter 4, we validated the mass transfer model for an oxygen single-bubble rising in a borosilicate melt. In this section, we aim to adapt this mass transfer model to be used for a population of bubbles for an isothermal study at 1000 °C. Thus, we use in the numerical model the melt properties at this temperature, along with the bubble features at the initial stage, which was experimentally acquired at 20 min (1000 °C 20min). This mass transfer model has been firstly developed by Pigeonneau[13] and it is described in this manuscript in chapter 2 (section 2.3.1).

Since this numerical model was published for a single-bubble system, in this section we present, for the first time, the adaptations used to apply this numerical code to a bubble population system. The current bubble population system contains an enormous amount of bubbles, $\langle \mathrm{N_b^{2D}} \rangle$ ~2400 cm^{-2} (~ 10000 bubbles in total). Hence, in order to model it, a simplification of the system must be done. In this section, we present the modifications used to adapt the single-bubble model to the bubble population system. This adaptation is composed by three main parts. A partition of the system according to bubble sizes is firstly done by grouping them in histograms. After, we estimate the 3D bubble features from the 2D ones. Finally, a system partition in terms of spatial initial position of the bubbles is done. Therefore, we use this section to present these three modifications. It is important to emphasize that both, single-bubble and bubble population models, consider just mass transfer as the growth mechanism.

5.3.1 Partition of bubble size

A partition of the system, according to bubble size, is done by analyzing the bubble diameter distribution through a histogram of bubble sizes. A histogram is a graphical representation composed by bars (also called classes) whose height is the frequency of appearance of a given variable (*e.g.* diameter) and width is equal to the class size. In general, the number of classes in a histogram can be chosen based on the total number of particles,[11,14,15] or depending on how the histogram will be used, it can be fixed as a constant. Since the current system has a large total number of bubbles (10000 bubbles), it would give a large number of classes (*e.g.* 100 using the square root rule, 26 using Doane’s rule and 18 using Sturges’ rule).[14,15] Thus, in our case, we set the number of classes as constant and we work with two different histograms, one composed by 5 and another one by 15 classes. This choice is made in order to save numerical computational time in the following step, which is the mass transfer calculation. While in the first situation (5 classes) we save a considerable computational time, in the second one (15 classes) we are closer to the real particle size distribution. The real system, which is composed by thousands of bubbles, is reduced to a system composed by 5 or 15 classes of bubbles. This reduced system is composed by few parameters, such as the midpoint, the width and the frequency of appearance each class. They are defined by taking the smallest and the largest bubbles, along with the number of class and the distribution of bubbles.

Figure 5.4 presents the bubble diameter histogram, for the 2D optical microscope image, showing the bubble population partitioned into 5 and 15 classes, for the input sample (1000 °C 20min). In these histograms, one can obtain the bubble density in each of the bubble classes as well as their midpoints. All the diameters which belong to a certain bubble class are converted to the midpoint value of this class and all the numerical calculations are based on this latter value. This midpoint is just a graphical representation and is the mean value between the right and left edges of each bubble class.

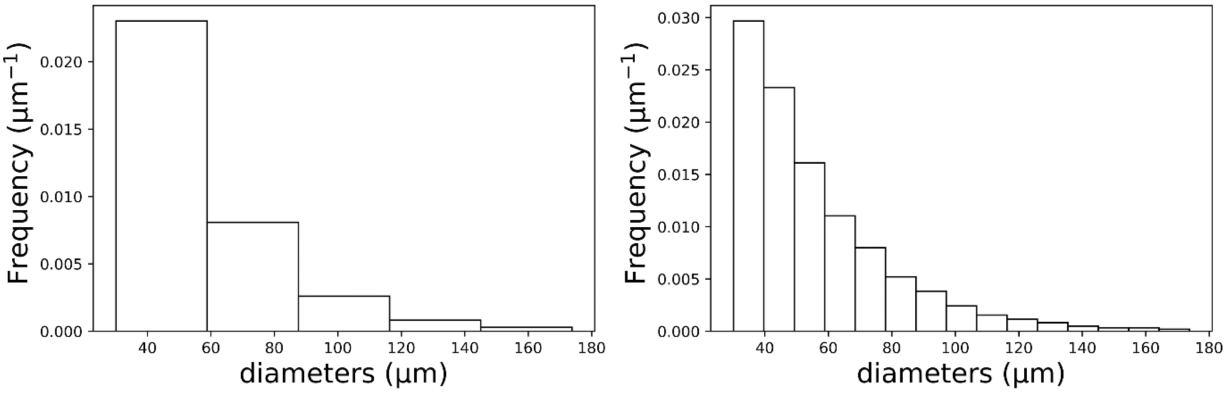

Figure 5.4: Histograms containing 5 (left) and 15 (right) classes displaying the 2D bubble distribution of the sample synthesized at 1000 °C during 20 min.

Since we have portioned the system into classes, we have to consider now this change into the numerical model. Thus, we modify the time derivative of the number of moles from a single-bubble scenario to a bubble population one. The equation for the single-bubble situation is given by:

$$\frac{dn_i}{dt} = 2\,\pi\, aSh_iD_i(C_i^\infty - C_i^s). \tag{5.1}$$

Since now we are dealing with a population of bubbles, we have to consider the bubble density of each class. Indeed, it can be reached by multiplying the total 3D bubble mean density, $\langle N_b^{3D} \rangle$, by the fraction occupied of each class, which is obtained through the histogram of diameters. The exponent "3D" of the bubble mean density is explained in the following section. Therefore, the time derivative of the number of moles for a given class "m" is given by:

$$(N_{b\_m}^{3D})\frac{dn_i}{dt} = 2\,\pi\, aSh_iD_i(C_i^\infty - C_i^s)\,(N_{b\_m}^{3D}). \tag{5.2}$$

Thus, by summing the contribution of all 5 or 15 classes, it is expressed by:

$$\langle N_b^{3D} \rangle \frac{dn_i}{dt} = 2\,\pi \sum_{m=1}^{5\text{ or }15} aSh_iD_i(C_i^\infty - C_i^s)\, N_b^{3D}. \tag{5.3}$$

For a single-bubble, due to the small amount of mass exchanged with the liquid, the thermodynamic state of the melt is almost constant with time. So, almost no variation of gas concentration in the bulk (C_i^∞) is noticed. However, when the bubble density is taken into consideration, the total mass exchanged between the bubble population and the melt is much more pronounced and consequently it may affect the thermodynamic state of the bulk material. In the current study, the results in terms of thermodynamic state of the glass melt is displayed latter in this chapter (section 5.4.2). Pigeonneau[16] described in details how the population of bubbles changes the redox state of the melt. He considered the produced or consumed gases by the bubbles shift the equilibrium of the chemical reactions. In these computations, it takes into account ions, fining and non-fining species.

Still considering the bubble partitioning into classes, one may state that the diameters displayed in **Figure 5.4** are log-normally distributed as some other events observed in material science.[17,18] It is a continuous probability distribution of a variable whose logarithm is normally distributed. In order to verify if these diameters are log-normally distributed, a quantile-quantile (Q-Q) plot may be a simple and fast initial option. A quantile is a cutting value that splits the data into groups with the same cumulative probability (area under the curve). Technically, the median is a quantile because it splits the data into two groups that contain 0.5 as cumulative probability. Q-Q probability plot is a graph method for comparing two probability distributions and to check if they follow the same type of distribution, based on the comparison of their quantiles. The first one is a theoretical distribution with well-defined normal parameters. The second one is the logarithmic value of the experimental diameters. Thus, if the quantiles from these distributions are arranged in a straight line, the logarithmic of the diameters are normally distributed and consequently, the diameters follow a lognormal distribution.

Figure 5.5 presents a Q-Q plot showing that the observed bubble diameters of the sample synthesized at 1000 °C during 20 min, at a first look, are log-normally distributed. The points on the bottom left of the plot do not follow the straight line because the employed experimental methodology (optical microscopy) has a detection limit of 30 μm, which common logarithm is around 3.4. Thus, values lower than 3.4 are not computed in the plot, which results in a flattening of the curve for these values, in such a way that bubble diameters seem to follow a truncated log-normal distribution in this researched case.

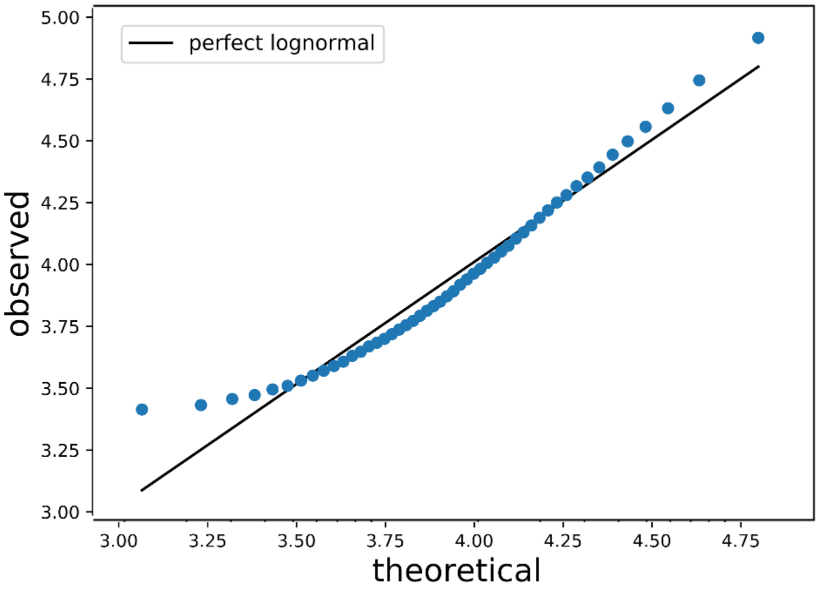

Figure 5.5: Q-Q plot displaying that bubble diameters obtained experimentally are log-normally distributed for most of the values of the sample synthesized at 1000 °C during 20 min.

5.3.2 2D – 3D estimation of bubble size

When spheres are dispersed in a given volume and this latter is cut, in the cutting plan, we can see a distribution of spheres with different diameters from the original one. These observed diameters on the cutting plan are called apparent (2D) diameters. However, these mentioned diameters are not the real ones from the 3D spheres, which are called actual (3D) diameters. **Figure 5.6** displays a scheme of a cutting plan, presenting the apparent diameters and the actual diameters. As it can be observed, the maximum value that an apparent (2D) diameters can have, is the actual one, which makes a 2D observation, in terms of individual bubbles, an underestimation of the reality. On the other hand, as large spheres are more likely to be cut, the 2D mean diameter is an overestimation of the 3D one.[19] It is important to underline that, for a homogeneously dispersed phase, surface fraction, linear fraction and point fraction are statistically unbiased estimations for the volume fraction.[9]

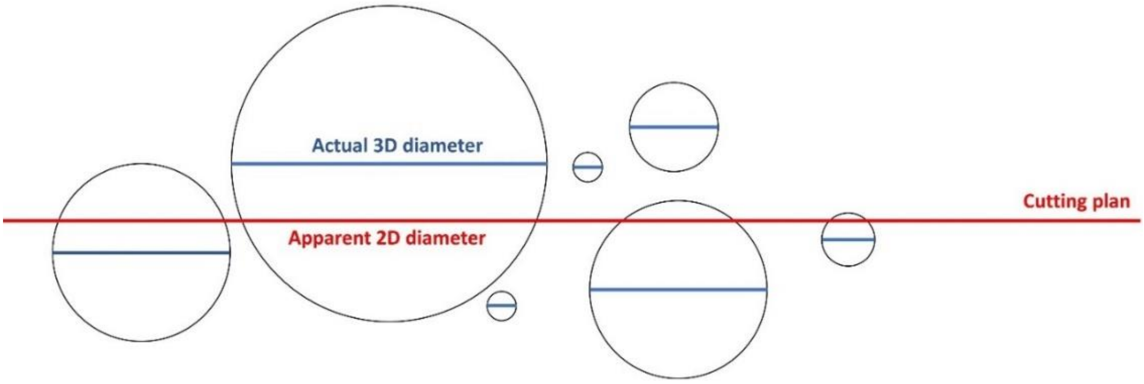

Figure 5.6: Cut spheres in a given plan to illustrate apparent (2D) and actual (3D) diameters.

Bubble 2D – 3D estimation is done, since bubble size plays an important role in bubble dynamics. It may affect several characteristics of the bubbled-melt, such as bubble residence time in the crucible and mass transfer coefficient.[13,20] Thus, this conversion must be done in order to better estimate the experimental results using the numerical simulation calculations. In this PhD, the procedure to convert 2D diameters into 3D ones is based on stereology, more precisely the Saltykov method.[10] We have used a Python script, GrainSizeTools,[12] developed by Lopez-Sanchez, to unfold the studied bubble populations. This is a stereological method that approximates, using the histogram of the apparent bubble size distribution, the actual bubble size distribution. This method uses a histogram of bubbles and a sequential subtraction procedure to convert the apparent size distribution into the actual particle size distribution. The method requires a system which follows the four basic assumptions:

i) The particles (bubbles) may be mono- or poly-dispersed, that is, all the particles may be of the same or different sizes.

ii) All the particles must have the same shape and differ only in size.

iii) The shape of the particles must be such a random plan intersects it only once. The distribution of particles must be statistically uniform, so that the number of particles per unit of volume, $\langle N_b^{3D} \rangle$, has a constant value.

iv) Particles are randomly oriented in space.

Our investigated system follows all this aforementioned assumptions except the second one. Indeed, bubbles in the surface do not have spherical shapes, having mostly oval shape. However, due to the small amount of oval shaped bubbles when compared to the spherical ones in the bulk sample, this non-spherical bubbles can be neglected.

Lopez-Sanchez *et al.*[11], listed some advantages and limitations of Saltykov method for investigating grains in mylonites. Firstly, this stereological method is versatile and enough sophisticated to deal with real data. Besides, it is free of size distribution assumptions, which is crucial when dealing with multimodal distributions. Lastly, it can be implemented and used in code routines by non-experts stereologists. In terms of drawbacks, Saltykov method requires large samples (>1000 particles), which is the current case. Besides, due to the use of histograms, the class size might determine the accuracy and success of the method. However, a trade-off exists because the larger the number of classes, the better approximation of the targeted distribution, whereas the smaller the number of class, the better numerical stability of the calculation. The most important limitation of this stereological method is that due to the use of histogram, we cannot obtain 3D individual bubble information. On the other hand, for the studied case, the given details are already enough and we do not need individual information.

Figure 5.7 displays the apparent and actual bubble distributions for the bubbled-samples partitioned into 5 and 15 classes. It is interesting to note that, for the system partitioned into 5 classes, the actual bubble distribution has nearly the same distribution as the apparent one obtained by optical microscopy imaging. On the other hand, the Saltykov method applied to the system partitioned into 15 classes show a slightly different bubble size distribution. For this last partitioned system, the 3D bubble distribution presents slightly more bubbles in the large classes, illustrating the idea previously mentioned, that 2D diameters might underestimate the 3D diameters. The large bars' width along with the small amount of them, in the system partitioned into 5 classes, makes the amount of bubbles which are promoted to other classes small when compared to the total of each class. Thus, the diameters before and after conversion are similar in systems portioned into small number of classes.

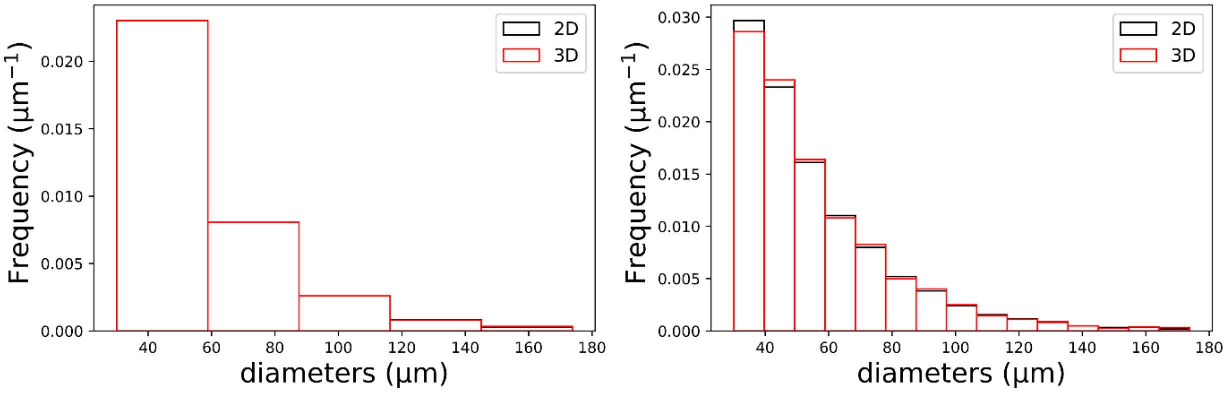

Figure 5.7: Histograms containing 5 (left) and 15 (right) classes displaying the 2D and 3D bubble distributions of the sample synthesized at 1000 °C during 20 min.

5.3.3 Partition of initial bubble position

Bubble initial position in the crucible may affect its residence time, and as consequence, the bubble mean density, bubble mean diameter and even the growth mechanism.[13,20] Thus, the last adaptation is the bubble initial position in the crucible. We start from the fact that, in a granular glass system, bubbles may be formed by air entrapment.[6,21] This is observed for this investigated system and we give more evidence of this type of bubble formation in the following section. Therefore, by understanding that bubbles are formed by air entrapment, one can conclude that they are formed by a non-classical nucleation type, as presented by Jones *et al.*,[22] and consequently, the initial position of these bubbles are in the interstices between glass beads, which were previously occupied by air. Therefore, it means that bubbles are, initially, homogenously dispersed in the glass matrix.

Practically speaking, we partitioned the system into 5 different initial positions (H). In this way, we dispersed the bubbles without overloading the computational effort. The initial position is based on the total height of the crucible (40 mm) as well as the apparent glass powder density (50 vol.%). Then, after melting this glass powder, the column of glass has a 20 mm height. Thus, the mentioned 5 bubble heights, in which the bubbles are distributed, are: 0, 4, 8, 12, 16 mm. In each of these different initial positions, we feed the system with the initial 3D bubble mean density $\langle \mathrm{N_b^{3D}} \rangle$ – **Figure 5.8**. It is important to note that, in this work, the horizontal distribution of bubbles in the crucible, is neglected. We consider that bubbles in different radial positions behave similarly.

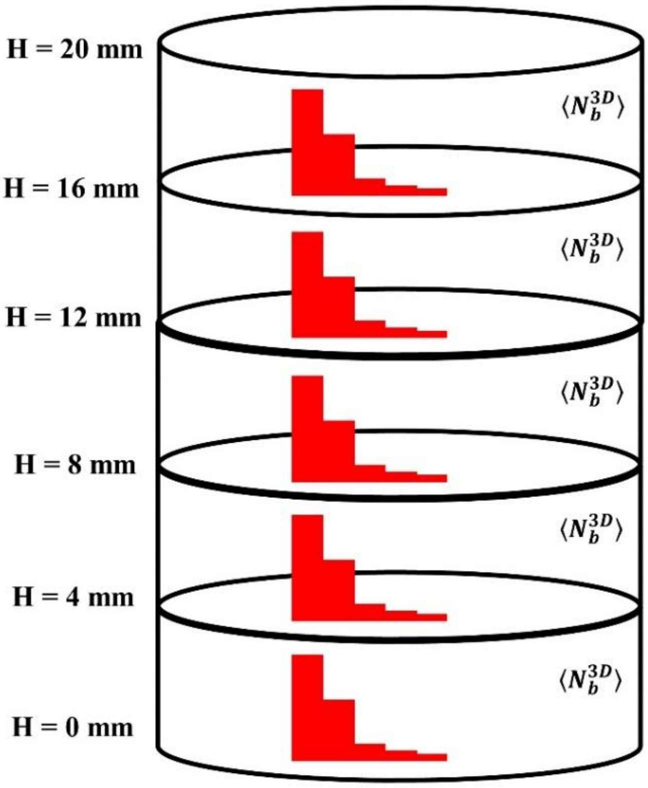

Figure 5.8: Crucible partition, in terms of height, showing the 5 different heights and each of them containing the bubble histogram and one fifth of the bubble mean density.

5.4 Results

We divide the bubble population results into experimental and computational modeling parts. In the former one, we present the main insights obtained by *post-mortem* bubble observation along with some characterization, such as cerium speciation and bubble gas composition. Thereafter, we present the numerical computations results, presenting the evolution of some features and a comparison with the experimental results.

5.4.1 Bubble population – experimental results

The experimental results are presented in this section. Firstly, we go through the multivalent (cerium) study, investigating its speciation over time and temperature. Subsequently, a comparison with the thermodynamic value of cerium speciation is done.[23] Afterward, we present how bubbles are nucleated in this melt and some features of the formed bubbles. Once they are formed, we exhibit a general overview of the bubbled-melt along with some bubble population features, such as bubble mean density and bubble mean diameter. Finally, we normalize the obtained bubble features, using a characteristic residence time, which is function of the glass melt properties.

I. Cerium speciation

Cerium is the chosen multivalent element of the simplified glass system. XANES spectroscopy measurements is carried out to reach cerium speciation in the synthesized glasses. **Figure 5.9** presents how $\mathrm{Ce(III)/Ce_{total}}$ evolves, with temperature and time, and it gives, indirectly, information about molecular oxygen production, as shown in Eq. (5.4). By way of illustration, if 100 % of the cerium, in our case, is in its reduced form, around 3.30 mL of molecular oxygen will be formed inside the molten glass (~10 mL).

The symbols, in **Figure 5.9**, are the experimental data obtained by XANES spectroscopy measurements, while the continuous lines represent the theoretical values, proposed by Pinet *el al.*[23] for a specific glass melt situation ($\mathrm{f_{O_2}}$ = 0.21 and Λ = 0.53). This oxygen fugacity is the thermodynamic one, in the case the molten glass is in equilibrium with atmosphere ($\mathrm{f_{O_2}}$ = 0.21). Since this atmospheric oxygen fugacity is higher than a typical commercial glass melt, $\mathrm{Ce(III)}$ fraction might be underestimated by this approach.[24] The optical basicity, in its turn, is calculated based on the concept and some tabulated values proposed by Duffy and Ingram.[25]

In **Figure 5.9**, it can be observed a difference between the theoretical and experimental values. Probably this difference is due to fact that we are not in equilibrium with atmosphere and an overestimation of oxygen fugacity in the model is assumed. Consequently, an underestimation of the $\mathrm{Ce(III)}$ fraction is observed for the theoretical values.

Considering the results at 900 and 1000 °C, an increase in $\mathrm{Ce(III)}$ fraction over time is observed, meaning that the cerium redox reaction, in this scenario, is not an instantaneous event. Hence, $\mathrm{Ce(III)}$ fraction increases over time for a fixed temperature and the higher is the temperature, the more reduced this multivalent will be.

$$\mathrm{Ce^{4+}} + \frac{1}{2}\,\mathrm{O^{2-}} \rightleftarrows \mathrm{Ce^{3+}} + \frac{1}{4}\,\mathrm{O_{2(g)}}. \tag{5.4}$$

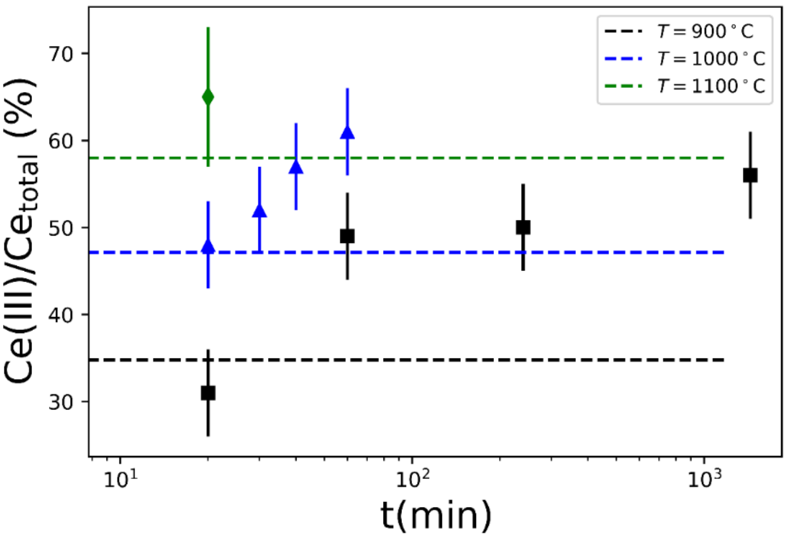

Figure 5.9: Ratio $Ce(III)/Ce_{total}$ as function of time in samples synthesized at 900, 1000 and 1100 °C, (f_{O_2} = 0.21 and Λ = 0.53).

The time dependence presented in **Figure 5.9** for 900 and 1000 °C is not yet fully understood. Hypotheses are presented to explain the non-instantaneous cerium reduction in the studied case. It is known that the reaction evolution depends on the incorporation of the added CeO_2 particles as well as the diffusion of the formed products ($Ce(III)$ and $O_{2(g)}$) from the reaction site to the molten glass.[26] What is observed at 900 °C is that even at the long experimental durations (900 °C 24h), there is still CeO_2 non-incorporated particles in the melt (**Figure 5.10**). Thus for this temperature low incorporation rate controls the kinetics of the redox reaction. On the other hand, at 1000 °C, scanning electron microscopic (SEM) images revealed that even at initial stages (1000 °C 20min), cerium oxide is completely incorporated in the glass matrix (no CeO_2 particles observed). Thus, the hypothesis proposed for this last temperature is that the generated products hardly diffuse from the reaction site, creating than a local equilibrium, which prevents a fast development of the redox reaction. In a similar system doped with iron, Cochain *et al.*[26] suggested that diffusion of oxygen is the rate-limiting factor for reduction or oxidation reactions. Thus, it must be pointed out that either low incorporation rate or low products diffusion from the redox reaction site may cause this observed time dependence.

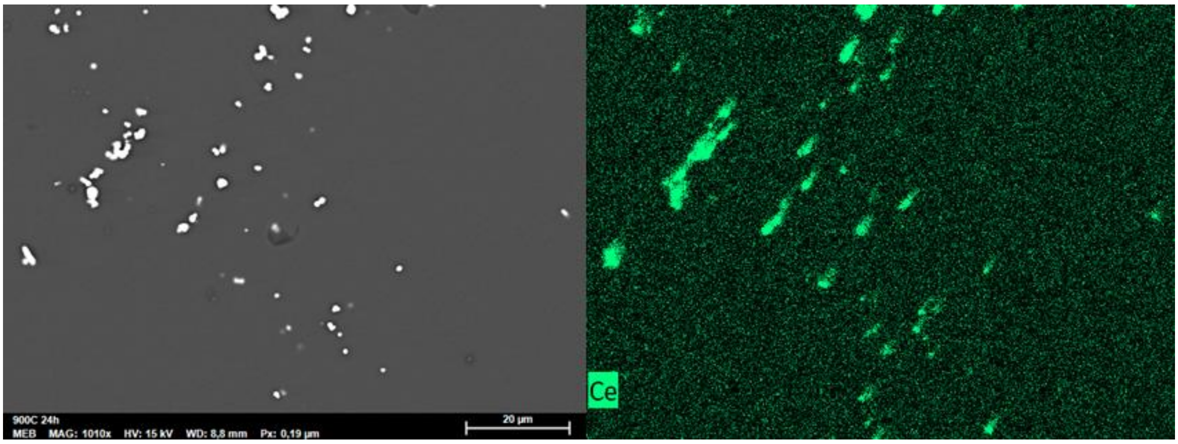

Figure 5.10: Scanning electron microscopic (SEM) image showing an example of region with non-incorporated cerium-IV oxide ($\mathrm{CeO_2}$) for the sample 900 °C 24h.

In order to illustrate the amount of molecular oxygen generated by the cerium redox reaction in the system, a simple stoichiometric calculation is carried out for the sample synthesized at 1000 °C for 20min. It is done by taking the melt density at 1000 °C (2283 Kg/m^3) along with the glass melt composition (20 g of borosilicate + 0.1 wt% of $\mathrm{Ce_2O_3}$) and the reduced cerium percentage ($\mathrm{Ce(III)}$ = 48 %). Thus, in this situation there are 8.75 mL of melt and a volume equals to 1.48 mL of molecular oxygen. By considering an idea gas situation, this gas volume is equivalent to around 15 % of the system.

II. Bubble nucleation

Bubble formation in glass melts is intimately related to the precursors and to the experimental procedure. In this case, both glass powders and bubbles are log-normally distributed. These previous statements are shown respectively in chapter 3 (section 3.1) and previously in this current chapter (section 5.3). In this investigation, the crucible is totally filled, at room temperature, with granular medium and it is introduced into the already heated furnace. The main effect of this introduction is a strong surface heating of the granular medium. Considering the main heat flux as radiative transfer, along with Eq. (2.20) and Eq. (2.21), described in the bibliographic review (chapter 2), the calculated time to melt a thickness of 1 mm is around few seconds. It means that the top surface of the medium is quickly melted and as consequence, the gas, which occupies the interstices between glass beads, cannot escape easily from the granular medium. This behavior is illustrated in **Figure 5.11**. In this figure, large amount of air is entrapped forming a torus, which is represented, in the 2D image, by two large black spots. When this large gas package is released, the system volume decreases roughly by half, which is consistent with the apparent density of the glass powder before melting (~50 vol%). Even having a great part of the entrapped air giving rise to the large air package, part of the air does not percolate until the torus and gets entrapped as microbubbles, which are log-normally distributed in terms of size.

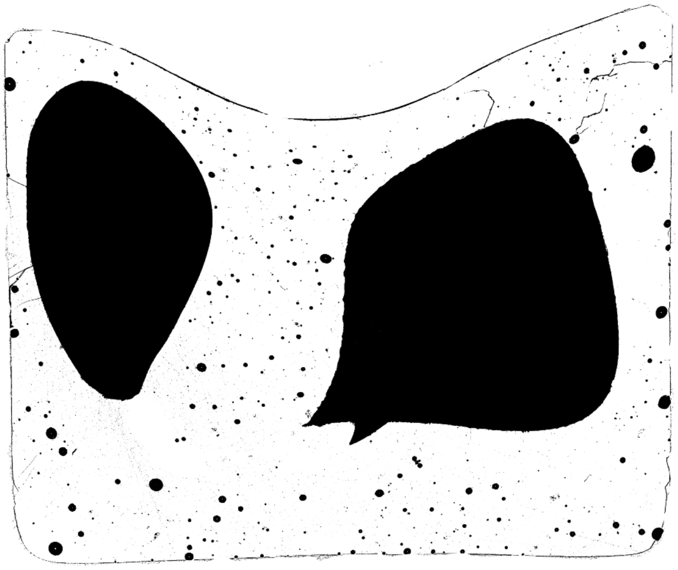

Figure 5.11: Sample synthesized at 800 °C during 20 min presenting a torus, represented in 2D by two large black dots, and several microbubbles homogeneously dispersed in the glass matrix.

These microbubbles are intimately related to the granular media.[6] They are well dispersed in the matrix, not having a preferential nucleation site. Likewise, as presented in **Figure 5.12**, bubble gas composition results reveal that the initial composition in low temperature (900 °C), in which bubble dynamics is extremely reduced, is mainly air. This is verified by the initial nitrogen amount and the ratio between nitrogen and argon, which is always constant. Therefore, this previous characteristic also reinforces the idea that initial bubbles come from entrapment of air during melting. Besides this information, one can notice from **Figure 5.12** that oxygen migrates from the melt to the bubbles over time and at the end of the experiment, the bubble mean composition is mainly composed by oxygen. Thus, the produced oxygen by the aforementioned cerium redox reaction may either feed the existing air bubbles or could be used to nucleate new oxygen bubbles.

These trapped microbubbles are extremely important in terms of bubble formation in the bubble population system. Jones *et al.*[22] examined a type of nucleation, in which bubbles come from pre-existing ones and it is called “non-classical nucleation”. The nucleation energy barrier in this previous case, does not exist because the pre-existing bubbles are larger than the critical radius. Thus, these previous facts suggest that the current system presents this type of bubble nucleation, which is not actually a nucleation event itself.

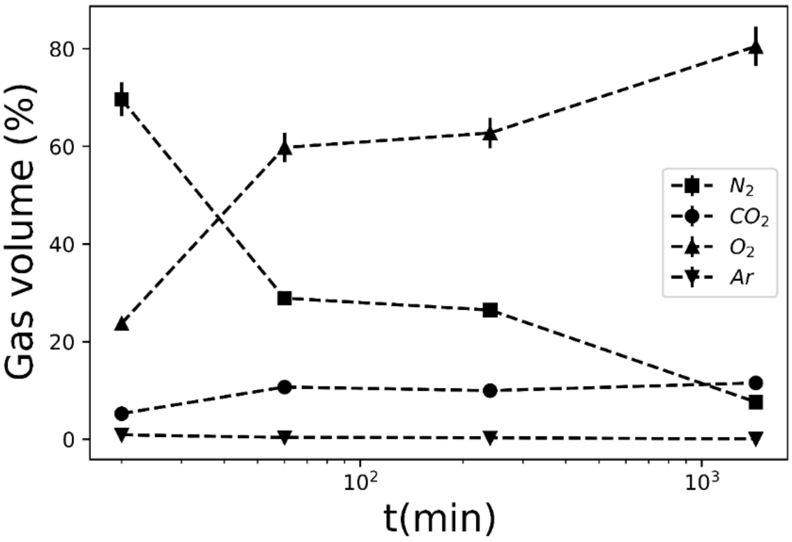

Figure 5.12: Mean volume percentage of gaseous species in bubbles as function of time in a sample synthesized at 900 °C.

III. Bubble behavior

After being formed, bubbles may undergo different phenomena in the melt, such as coalescence, mass transfer (growth or shrinkage) and buoyancy motion. Thus, bubble features, such as bubble mean density, bubble mean diameter and bubble surface fraction may change over time. **Figure 5.13** exhibits nine optical microscope images after image treatment giving an overview of how some bubble features evolve at different temperatures. These samples are obtained at 900, 1000 and 1100 °C and each of these temperatures have, as residence time in the furnace; 20, 60 and 120 minutes. While at 900 °C, the bubble mean density visually increases with time, for the two other temperatures, it decreases. At 1100 °C, this decrease seems to be more intense and for long residence times, the bubble mean density seems very low. Besides these temperatures, some experiments at 1200 °C have been carried out. At this temperature, bubble motion is even more elevated and the current *post-mortem* methodology is not suitable to provide enough information.

Through analyzing **Figure 5.13**, bubbles' shape might also draw our attention. It is known that bubbles tend to get a spherical shape in order to reduce their surface energy. This is what happen in the center of the crucible where bubbles are mainly surrounded by melt and are able to decrease this type of energy. However, in the free-surface of the crucible, bubbles interact with air and are also submitted to the glass meniscus deformation force. Therefore, bubbles in this mentioned region have, roughly, an oval shape, as displayed in some of the samples of **Figure 5.13**.

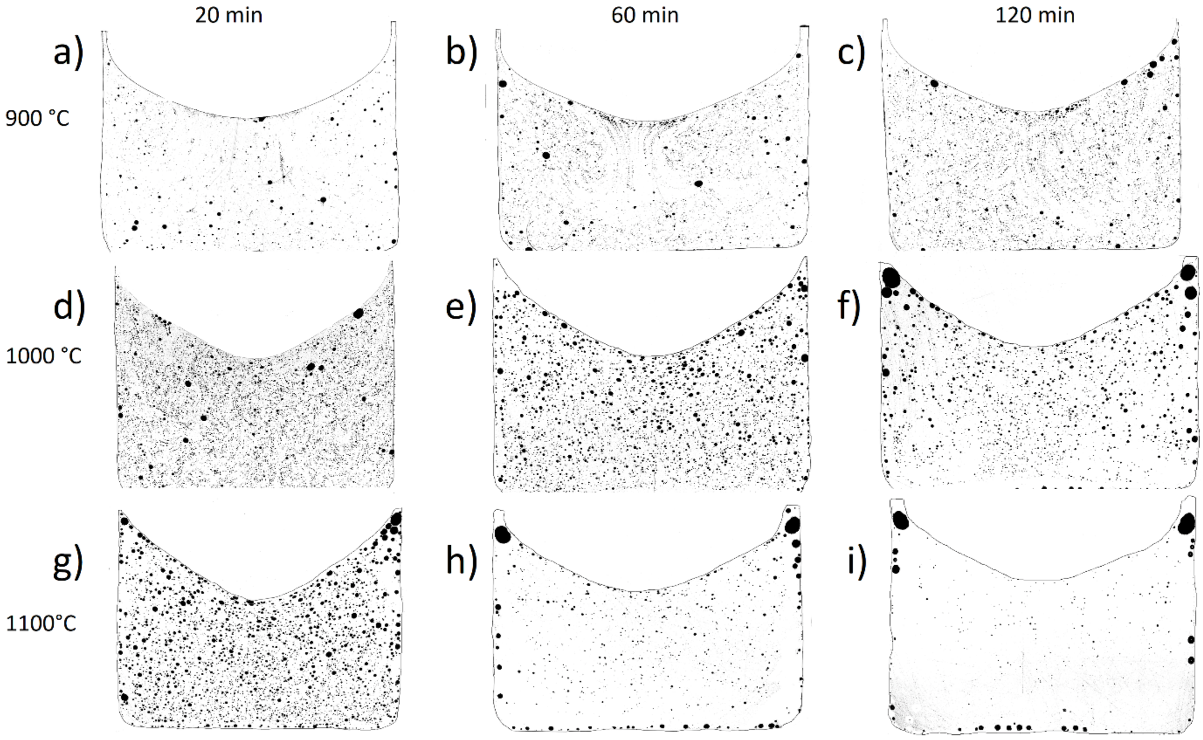

Figure 5.13: Binarized optical microscope images of samples treated at (A) 900°C 20 min, (B) 900°C 60 min, (C) 900 °C 120 min, (D) 1000°C 20 min, (E) 1000°C 60 min, (F) 1000°C 120 min, (G) 1100°C 20 min, (H) 1100°C 60 min and (I) 1100°C 120 min

Figure 5.14 exhibits bubble mean density, bubble mean diameter and bubble fraction for the samples synthesized at 1000 °C along with the related standard errors. For this specific temperature, each measurement is replicated five times in different surfaces of the samples (subsequent analyses and polishing procedures). This is done in order to validate the good reproducibility of the technique and an error is extracted from these measurements.

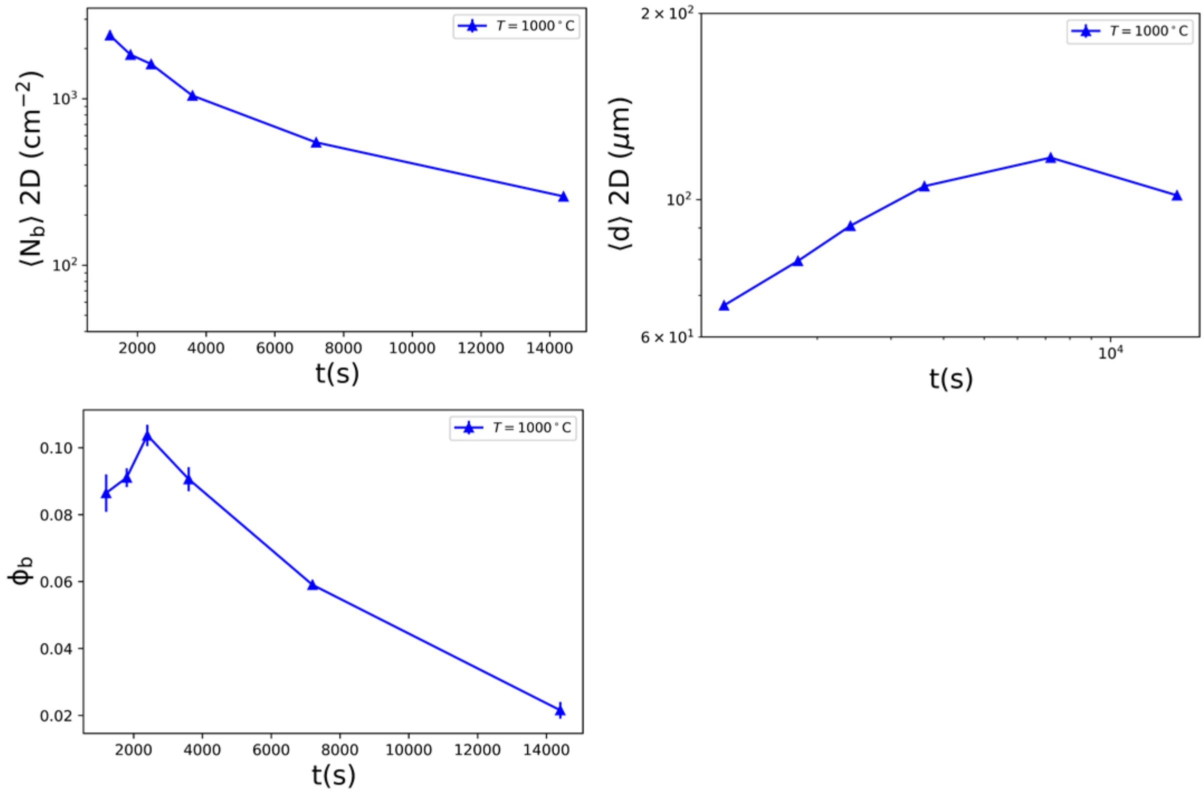

Figure 5.14: $\langle \mathrm{N_b} \rangle$, $\langle \mathrm{d} \rangle$ and $\phi_\mathrm{b}/\mathrm{max}\phi_\mathrm{b}$ as function of t for the studied melt doped with Ce for the samples synthesized at 1000 °C. The error bars for $\langle \mathrm{N_b} \rangle$, $\langle \mathrm{d} \rangle$ are smaller than the symbols.

Figure 5.15 presents the three mentioned bubble features for all the studied temperatures. This figure displays how $\langle \mathrm{N_b^{2D}} \rangle$, $\langle \mathrm{d^{2D}} \rangle$ and $\phi_\mathrm{b}^{\mathrm{2D}}$ change over time. Here, the related standard errors are not displayed because it would overwhelm the figure and we are interested in the general trend, and not the absolute values. Bubble mean density, at low temperatures (900 and 950 °C), initially rises until a maximum value is reached, decreasing after this moment. In order to not disturb the graph time scale, this last decrement at 900 °C is not displayed. On the other hand, for higher temperatures (1000, 1050 and 1100 °C), the aforementioned initial stage happens is not observed and only the second part of the curve is seen, in which bubble mean density drops. It is interesting to note that this decay is not linear with time, presenting roughly two stages. These decays are more intense for higher temperature situations.

In terms of bubble mean diameter, initially, at 900 °C, a decrease in this feature is noticed until it passes through a minimum and increases slowly afterward. Differently, for all the other temperatures, this initial decreasing stage is not observed and bubble mean diameter increases since the first investigated time (20 minutes). Afterward, for these latter temperatures, bubble mean diameter reaches a maximum and then drops. It is noteworthy that bubble mean diameter, in this case, is obtained in a cross-section surface, representing then the apparent (2D) bubble diameter, as previously discussed.

Finally, bubble surface fraction, at the beginning, for most temperatures (900 to 1050 °C), rises with time. After a certain duration in the furnace, it reaches a maximum value and it drops afterward. At 1100 °C, this initial increasing behavior might happen before 20 minutes and it cannot be observed in the current investigation. Therefore, since the first experimental time (20 min), a decrease of this feature at 1100 °C is observed. As for the other bubble features, the observed minimum and maximum points are function of the experimental temperature, appearing earlier for higher temperatures.

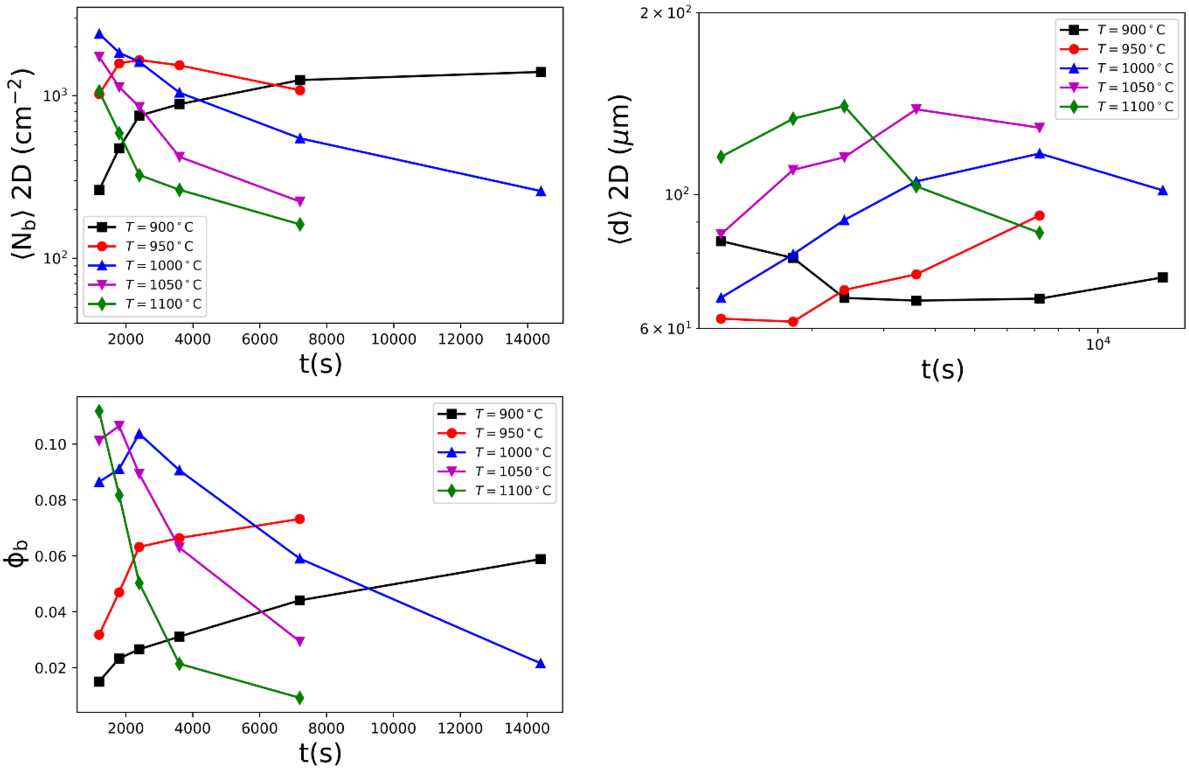

Figure 5.15: $\langle N_b \rangle$, $\langle d \rangle$ and $\phi_b / \max\phi_b$ as function of t for the studied melt doped with Ce for five temperatures from 900 to 1100 °C.

Here, we give a possible explanation about what is happening in the system to cause the aforementioned behavior presented in **Figure 5.15**. Initially, bubbles smaller than the detection limit (30 μm) are not computed by the employed methodology. Once they grow over this limit, they are computed and an increase of $\langle N_b^{2D} \rangle$ and ϕ_b^{2D} is observed. Moreover, a drop in $\langle d^{2D} \rangle$ is caused for this same reason. Another possible explanation would be the idea that cerium redox reaction, that is kinetically limited, keeps producing molecular oxygen and bubbles keep being nucleated and/or growing to decrease the supersaturation. Hence, the system would present two “nucleation” events. The first one made by air entrapment followed by this mentioned one to decrease the oxygen supersaturation. It is important to bear in mind that these two presented hypotheses to explain the initial part of the plots are not excluding, being possible then that both are correct. While the first hypothesis is supported by basic mathematic operations, the second one is supported by other methodologies (such as density and impedance spectroscopy – presented in chapter 6). Therefore, these two hypotheses would explain the initial increase in $\langle N_b^{2D} \rangle$ and ϕ_b^{2D}, and the decrease in $\langle d^{2D} \rangle$.

Once bubbles are continuously growing in this system, $\langle d^{2D} \rangle$ also does. This bubble feature keep growing until a certain point, in which their rising velocity is large enough to create a large exiting rate when compared to the growth rate. It happens because bubble rising velocity is proportional to the square of the diameter.[1,2] Thus, at the moment in which exiting rate overtakes the growth rate, $\langle N_b^{2D} \rangle$ and ϕ_b^{2D} decrease. $\langle d^{2D} \rangle$, in its turn, also does, because large bubbles rise faster and consequently leave the bath earlier.

We now introduce the characteristic time (t_η). It is determined taking into account the height of the glass bath (H = 20 mm) divided by $\rho g d_{max}^2/\eta$ which comes from buoyant and viscous forces balance.[27] While the former force comes from the volume of the displaced fluid the latter comes from the drag force cause by the bubble motion. It can be also seen as the terminal rising velocity proposed, in the last century, by Hadamard and Rybczynski.[1,2] Hence, we propose a characteristic time which is defined as follows:

$$t_\eta = \frac{\eta H}{\rho g (d_{max}^{2d})^2}, \tag{5.5}$$

where d_{max} is the maximum bubble mean diameter at a given temperature considering all the experimental durations.

The behaviors of the two-dimensional bubble mean density, bubble mean diameter and bubble surface fraction are plotted in **Figure 5.16** as function of t/t_η, in which t is the experimental time. A master behavior is clearly seen for these three normalized bubble features. Bubble mean density increases rapidly until t/t_η ~ 1, and afterward decreases approximatively exponentially until t/t_η ~ 3.5. Then, as aforementioned, the decay becomes softer. Bubble mean diameter, in its turn, decreases algebraically with time. For $t/t_\eta \in [0.1, 2]$, the bubble diameter increases also following an algebraic function of time and after this period, this feature drops due to the elevated bubble exit rate. Finally, the last bubble feature, bubble surface fraction, is plotted divided by the maximum bubble surface fraction $(\max\phi_b)$. After the fast increase until t/t_η ~ 1, this feature decreases approximatively exponentially until t/t_η ~ 3. Thereafter, the decay becomes softer, as reported for $\langle N_b \rangle$.

A master behavior of these three bubble features could be noticed by their normalization using the characteristic residence time. Thus, it is really important to recognize that for all the investigated temperatures, the mechanisms that govern bubble evolution are fundamentally the same. It is interesting to note that temperatures affects strongly the plots' optimum points making the events happen earlier for higher temperatures.

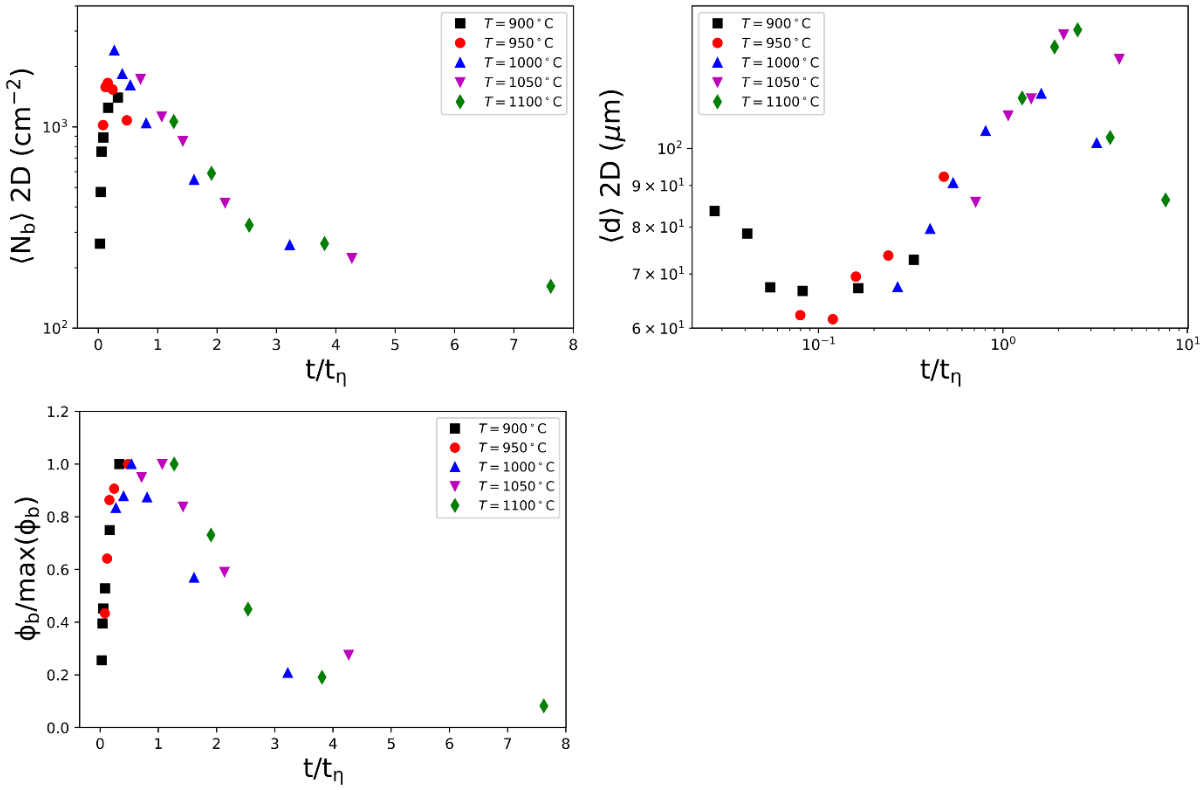

Figure 5.16: $\langle N_b \rangle$, $\langle d \rangle$ and $\phi_b/\max\phi_b$ as function of t/t_η for the studied melt doped with Ce for five temperatures from 900 to 1100 °C.

IV. Experimental section conclusion

We can highlight some interesting insights obtained experimentally, in terms of bubble population system. Cerium redox reaction was evaluated by XANES spectroscopy and a non-instantaneous development over time was noticed for lower temperatures (900 and 1000 °C). Possible explanations were raised for this last observation. SEM images give clues that cerium oxide presents low incorporation rate at 900 °C, what would limit the reaction development. On the other hand, at 1000 °C, the explanation is based on the fact the products of the reaction do not diffuse fast enough from the reaction site, avoiding then the reaction development. Besides, it was presented that bubbles are formed from pre-existing air microbubbles, being therefore homogenously dispersed in the volume and having initial composition similar to atmosphere air. Lastly, some bubble features were presented and a master behavior of them can be reached by dividing the experimental time by the characteristic time proposed herein. This latter is obtained using some characteristics of the system, such as viscosity and density.

5.4.2 Bubble population – numerical modeling results

Once the system is investigated by experimental means, we apply mass transfer laws in order to check if mass transfer can be the dominant bubble growth mechanism. If so, we will be able to predict events by numerical computations. These predictions are based on well-defined mass transfer and thermodynamic laws along with physical-chemistry and bubbles properties. These properties are obtained using the first experimental sample (1000 °C 20min), which is used as the input sample for the simulation. As concluded experimentally, the mechanisms that govern bubble evolution are fundamentally the same and the studied temperature affects the plots' optimum points, making the events happen earlier at higher temperatures. Thus, as mentioned, we investigate the bubble and melt behaviors at just one temperature, which is 1000 °C. In this section, we first present redox evolution in terms of cerium speciation and afterward, we present the evolution of some bubbles' features, such as vertical position of each class, average bubble composition, bubble mean density and bubble mean diameter. As explained in the section 5.2.1, we chose two different class numbers to carry out numerical computations. Here, we present, for these two classes, these mentioned results.

I. Cerium speciation

By considering the initial redox state of the melt (1000 °C 20min), along with the mass transfer laws, $\mathrm{Ce(III)}$ fraction evolution can be predicted. **Figure 5.17** displays this mentioned evolution, obtained numerically, for the two simulated systems (with 5 and 15 classes). The experimental results obtained by XANES spectroscopy are also presented as blue symbols. While the experimental result shows that $\mathrm{Ce(III)}$ fraction increases over time, the numerical one displays a slightly decrease.

The reason for this discrepancy is because we consider in the numerical simulation, that cerium redox reaction had already reached the equilibrium. However, in the reality, we could see that cerium reduction is kinetically limited by either by cerium oxide incorporation in the glass matrix or by products diffusion from the reaction site.[26] Hence, experimentally, this fraction keeps rising to reach the equilibrium, while numerically, $\mathrm{Ce(III)}$ slightly decreases due to mass transfer between the melt and the bubbles. Besides this observation, one can state that the number of class, in which bubbles are partitioned, does not play a role in the numerical simulation results.

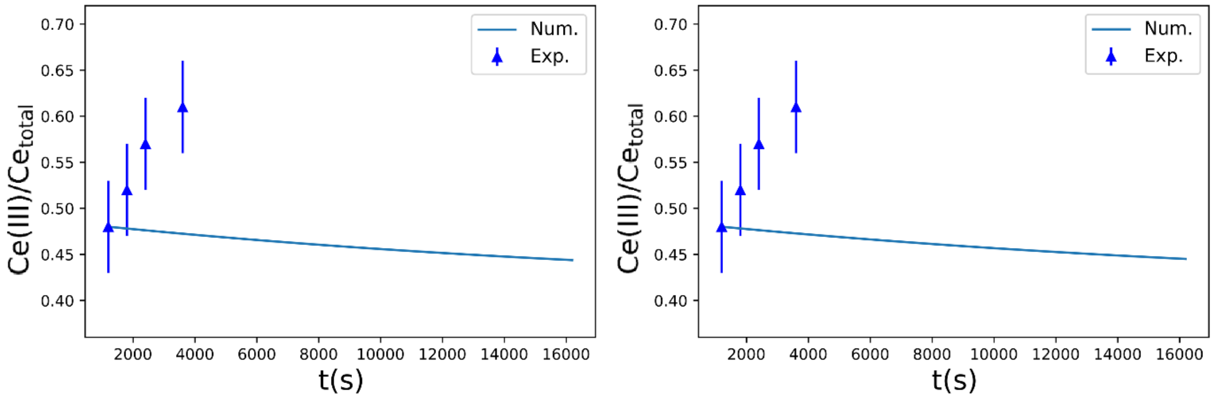

Figure 5.17: Experimental and numerical results of cerium redox evolution considering mass transfer between the glass melt and the population of bubbles. The left figure represents bubble population divided into 5 classes, according to their size, and on the right, divided into 15.

II. Bubbles' vertical position

Let's consider now some simulated results for bubble features. We first present the evolution, in terms of height, of each bubble class in the crucible. In both simulated systems, experimental insights have shown that bubbles are initially homogenously distributed and to represent it numerically, we divide the bubble population into 5 vertical positions, as mentioned. **Figure 5.18** exhibits the vertical position evolution for each bubble class during the numerical simulation. There are 25 classes in the first simulated system, while the second is composed by 75. For a given initial height, large bubbles rise faster and get to the upper surface (H =0.02 m) earlier.[1,2] Once a bubble class reaches this upper surface, it leaves the glass bath and it stops being computed by the calculations, modifying therefore the bubble features. The first bubble class takes, for the two situations, around 6000 s to leave the crucible. This class represents the large bubbles which is placed in the position close to the surface.

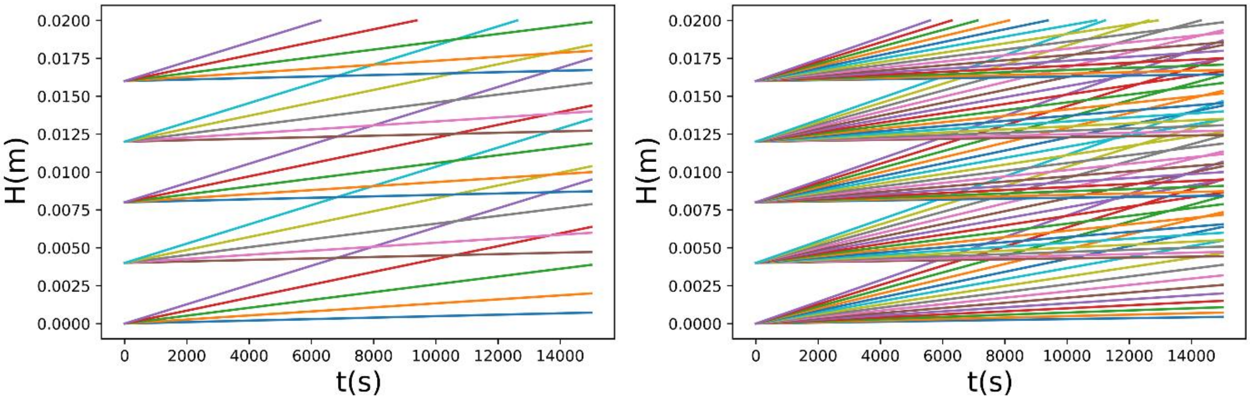

Figure 5.18: Numerical results of height evolution of each bubble class in the studied glass melt. The left figure represents bubble population divided into 5 classes and on the right, divided into 15.

III. Bubbles' gas composition

Due to the difference of gas concentration between the bubbles and the glass melt, gas may diffuse from one to other.[13] Based on the initial average bubble composition, obtained experimentally, along with well-defined mass transfer laws, we can predict how the average bubble composition changes over time. As mentioned in chapter 4 (section 4.3) along with the gas composition results previously presented (section 5.4.1), we consider in this model three gaseous species: O_2, N_2 and CO_2. **Figure 5.19** exhibits, for the two simulated systems, the experimental and numerical results in terms of average bubble composition. Experimental results demonstrate an increase of the average molar fraction of oxygen, a decrease of nitrogen and an almost constant behavior in terms of carbon dioxide. On the other hand, numerical results demonstrate a nearly constant molar fraction over time, for all of these mentioned gases.

Thus, as we can verify, the numerical results do not estimate the experimental data. As previously mentioned for redox state evolution (**Figure 5.17**), the discrepancy might be due to the consideration of the system in equilibrium, in terms of the redox reaction. If we considered in the model the non-equilibrium situation, molecular oxygen would keep being formed and this gas might diffuse towards the bubbles, making the oxygen fraction rises and the other ones drop proportionally. Besides, it can be stated that the number of class, in which bubbles are partitioned, does not play a role in the numerical simulation results.

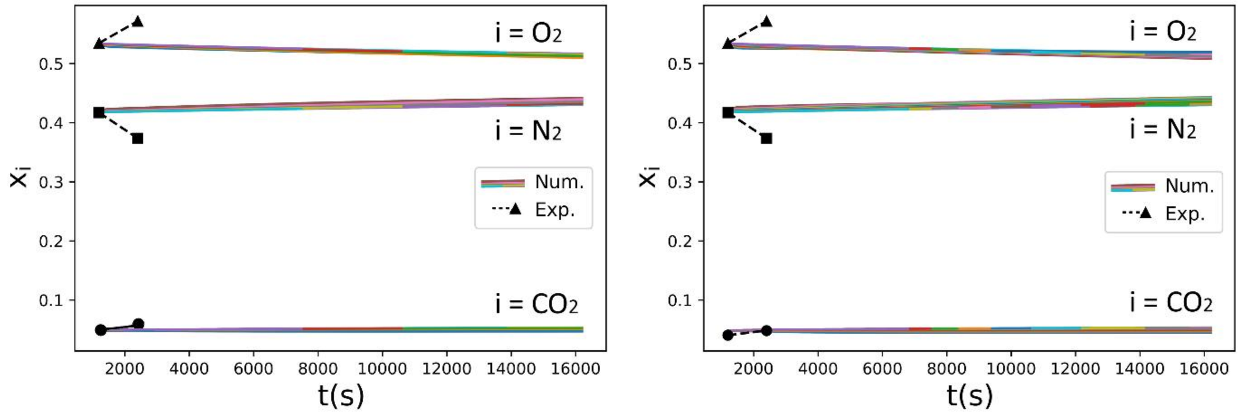

Figure 5.19: Experimental and numerical results of avarage bubble composition, in terms of molar fraction of the present gases. The left figure represents bubble population divided into 5 classes and on the right, divided into 15.

IV. 3D bubble mean diameter

Figure 5.20 exhibits the experimental and numerical 3D bubble mean diameters, as function of time, taking into consideration the redox, gas diffusion and the mass transfer laws. For the experimental results, as explained in the experimental section, there is an initial increase and after reaching a maximum value, it drops. The initial increase is due to a bubble growth mechanism and the observed decrease is explained by the exit of large bubbles, since these ones rise faster. On the other hand, numerical results demonstrate, in both cases, a slightly and continuous decrease of the bubble mean diameter over time. This decrease is not associated with bubbles exit, since the first bubble class leaves the system at around 6000 s of simulation (**Figure 5.18**).

Two reasons might explain this mismatch. The first is the assumption, used in the numerical computations, that redox equilibrium is reached and there are no kinetic limitations. Bubble mean size is not growing because numerical computations are considering redox reactions as an instantaneous event and consequently molecular oxygen production, which is formed after this initial stage, is ignored. Thus, the oxygen concentration difference between the glass melt and the bubbles is also underestimated, making then the mass transfer’s driving force smaller or even negative. This latter situation would make bubbles shrink instead of grow, as we could see in the presented results as well as by analyzing the ones in terms of redox (**Figure 5.17**).

The other possible reason to explain the discrepancy between experimental and numerical results is the considered growth mechanism. In the numerical simulation, as mentioned, the only considered growth mechanism is mass transfer. Then, a possible addition of bubble coalescence in the model may explain this bubble growth. Indeed, we should assume that coalescence might be taking place in the system because it was observed, by *in-situ* camera observation, that some bubbles are undergoing coalescence (**Figure 5.21**). Since through this technique, we are not able to obtain a volumetric information, it is difficult to estimate the coalesce rate using camera imaging. Therefore, by taking the glass melt properties along with bubble features, a coalescence model can be written in order to estimate the experimental behavior.

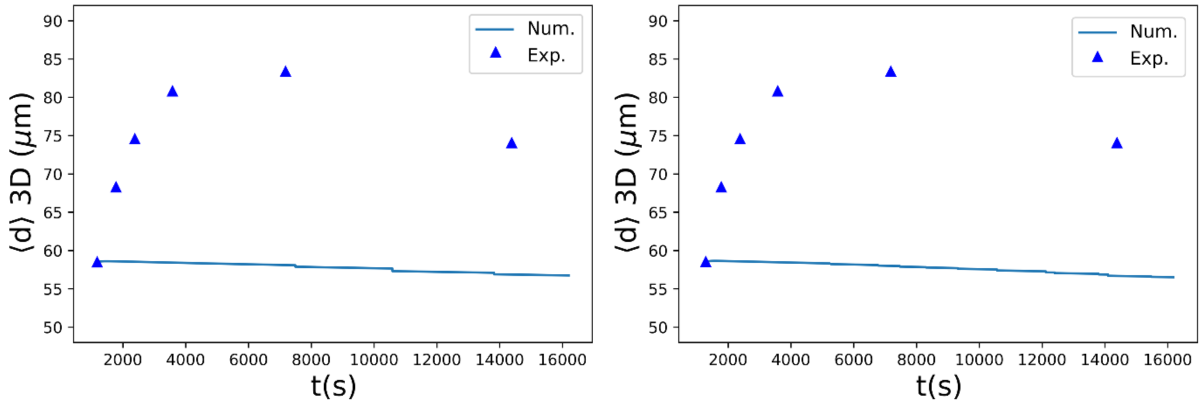

Figure 5.20: Experimental and numerical results of 3D bubble mean diameter. The left figure represents bubble population divided into 5 classes and on the right, divided into 15.

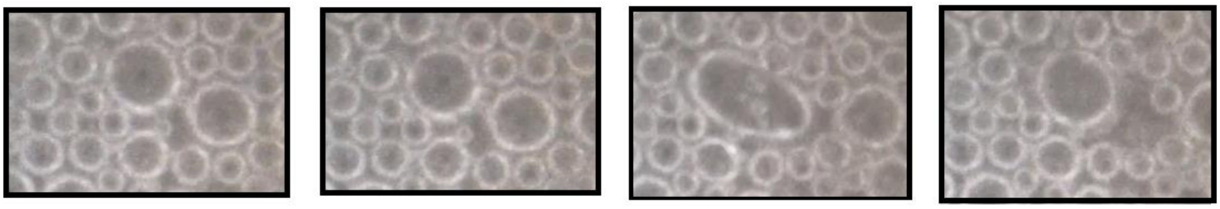

Figure 5.21: Different images, acquired by *in-situ* camera observation, illustrating the fact that bubble might undergo coalescence in a similar glass melt system (borosilicate beads doped with 0.1 wt% Ce_2O_3.

Figure 5.21 displays figures which are part of a video, obtained by *in-situ* camera imaging, showing two bubbles undergoing coalescence and giving rise to a large one. If two equal sized bubbles undergo coalescence, the new bubble has a diameter 26 % larger than the progenitor bubbles. This value comes from the fact that, in coalescence events, the volume is conserved and not the diameter.

Paying attention to the absolute values of 2D bubble mean diameters (**Figure 5.15**) and to the absolute 3D ones (**Figure 5.20**), the idea explained by Cuzzi *et al.*[19] is confirmed. They mentioned in a stereological study that 2D mean bubble diameter ($\langle d^{2D} \rangle$) might overestimate the real 3D ones because large bubbles are more likely to be cut.

V. 3D bubble mean density

3D bubble mean density is also simulated numerically and its evolution is presented in **Figure 5.22**. Experimentally, bubble mean density decreases over time and this behavior is due to the bubble exit from the crucible. Besides, this decrease may be related to bubbles which are undergoing coalescence, as previously suggested. Numerically, a slight decrease is observed and it is related to bubble exit, since the observed decrease is compatible with the moment in each the first bubble class leave the glass melt (around 6000 s).

The discrepancy between experimental and numerical data can be explained by the same idea used to explain bubble mean diameter results. If the cerium redox reaction was not kinetically limited, it would have more available oxygen in the melt, which would make bubbles grow faster, increasing consequently their rising velocity. Consequently, it would promote bubbles to leave with a higher exiting rate, decreasing more intensely bubble mean density.[1,2] Furthermore, bubbles undergoing coalescence might also explain bubble mean density behavior, since in coalescence events two or more bubbles become a large one.

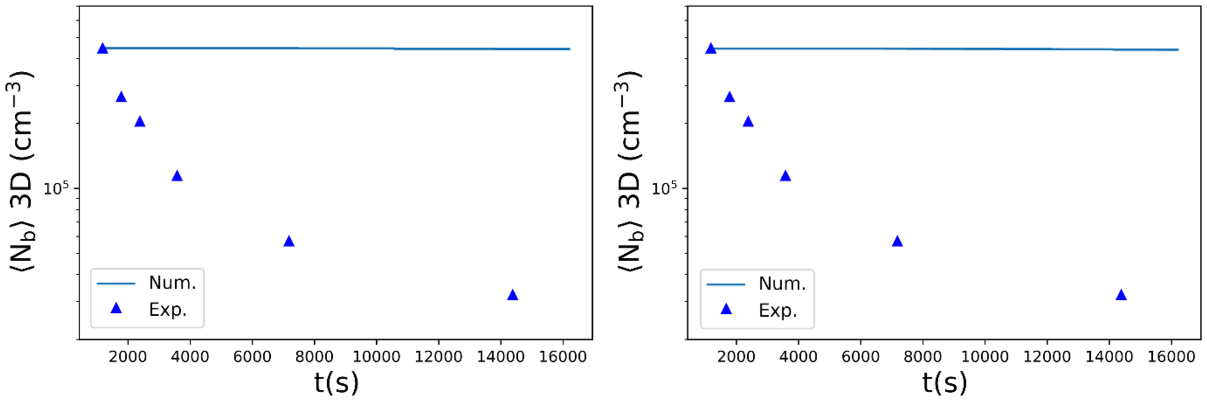

Figure 5.22: Experimental and numerical results of 3D bubble mean density. The left figure represents bubble population divided into 5 classes and on the right, divided into 15.

Theoretically, by applying coalescence events to the mass transfer model, it should make bubbles grow faster and make bubble mean density decreases. This last feature would decrease due to the coalescence event itself and because the formed bubbles, generated by coalescence, would leave the bath faster due to their large sizes. Besides, several numerical simulations, taking just mass transfer into consideration, were run for varying different parameters but it did not well estimate the experimental results. Thus, it also supports the idea coalescence should be taken into account.

VI. Coupling coalescence to the numerical model – first results

In this section, based on mentioned clues implying that coalescence events could be taking place, we executed some numerical calculations to verify this idea and proof that it a is reasonable path to keep researching. Cable[28] underlined that bubble coalescence can play a role in the dynamics at early stages of glass melting processes, especially in situations with low surface tension (0.20 – 0.40 N/m). It is important to mention that we present just an introduction of the future study. The main propose of this forthcoming work is to apply the population balance theory to our system considering the contributions of both mass transfer and coalescence.

To describe the dynamics of a population undergoing processes such as mass transfer and coalescence, a model based on the population balance theory[29,30] needs to be developed. The mass transfer part of this numerical code is based on the mass transfer model presented previously in this document. The coalescence part is under development and it is not described here. In this bubble population model, the direct quadrature method of moments, initially proposed by Marchisio and Fox,[31] is chosen to solve the population balance equation. This method enables us to take into account various processes such as bubble growth, coalescence, break-up and nucleation phenomena with a simple closure procedure.

Here, in **Figure 5.23** , we present the first result in terms of bubble mean density. This bubble feature is normalized by the initial bubble mean density ($t = 0$) versus the normalized time (t/t_η). This graph is composed by the experimental results (symbols) along with one numerical result that takes into consideration just mass transfer (blue line) and another numerical result that considers coalescence and mass transfer phenomena (red line).

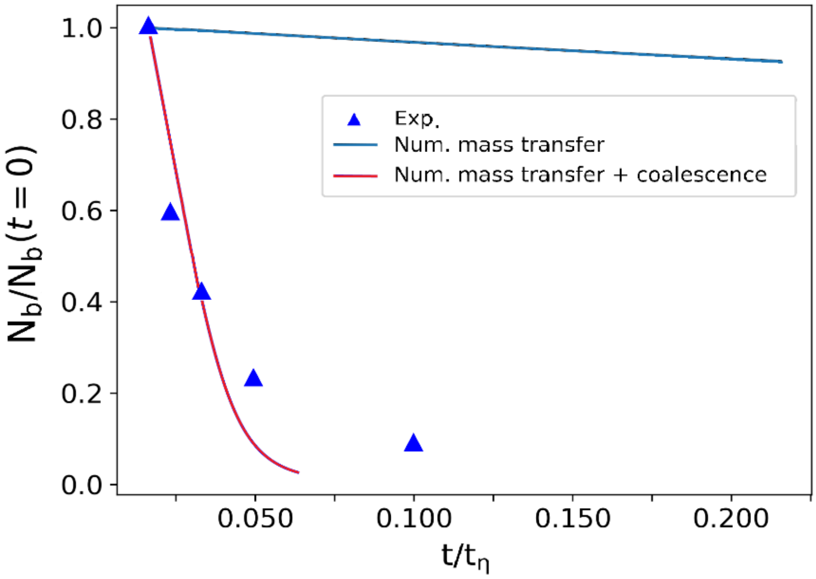

Figure 5.23: Experimental, mass transfer modeling, and mass transfer with coalescence modeling results in terms of normalized bubble mean density as function of the normalized time.

VII. Numerical section conclusion

By just taking the mass transfer numerical model into consideration, one can observe a mismatch between the experimental data and the simulated one. After executing some numerical calculations taking into account the coalescence contribution, the simulated results approached to the experimental ones. Indeed, we exhibited some experimental and numerical evidences showing that this mentioned growth mechanism should be presented. Therefore, between the two possible limitations of the applied model (cerium redox kinetics and coalescence events), the latter contributes mostly and by considering population balance theory along with mass transfer and coalescence, the complete modeling should be achieved.

5.5 Conclusion

In this chapter, it was investigated a population of bubble in a borosilicate glass melt doped with cerium oxide. This study was done by experimental means (*post-mortem* optical microscopy and other characterizations) and by computational modeling (mass transfer code). By the experimental approach, through XANES spectroscopy results, we concluded that $\mathrm{Ce(III)}$ fraction takes time at 900 and 1000 °C to reach the highest observed values. Still considering the experimental results, interesting results were observed in terms of bubble formation. We concluded that bubbles are nucleated by a non-classical way, being formed by air-entrapment and possibly new bubbles could be formed after this first nucleation event. Additionally, scientific advances about bubble behavior were presented. It was recognized, that for all the investigated temperatures, the mechanisms that dictate bubble evolution are fundamentally the same and that the optimum points are strongly influenced by temperature.

In terms of the numerical simulation, it was reported thermochemical and bubble features results. In terms of mass transfer modeling, the partition of the bubble system into 5 or 15 classes, according to bubble size, does not play an important role on numerical results, since they present really similar results. Thus, by using the portioned system into 5 classes one may save computational effort. Besides we concluded that if coalescence phenomenon was taken into consideration, the numerical results would be closer to the ones acquired experimentally

Since the use of *post-mortem* optical microscopic method to observe bubbles is a laborious and time-consuming task, in the following chapter, we propose the use of a novel technique to infer, in an *in-situ* way, bubble volume fraction in melts.

5.6 References

(1) Hadamard, J. S. *Compt. Rend. Acad. Sci.* **1911**, *152*, 1735.

(2) Rybczynski, W. *Bull. Acad. Sci.* **1911**, *A*, 40.

(3) Seshadri, V.; Tavares, R.; Da Silva, C. A.; Da Silva, I. A. *Fenômenos de transporte: fundamentos e aplicações nas engenharias metalúrgica e de materiais.*; Associação Brasileira de Metalúrgia, Materiais e Mineração (ABM), **2010**.

(4) Mourtada-Bonnefoi, C. C.; Laporte, D. *Journal of Geophysical Research-Solid Earth* **2002**, *107*, 19.

(5) Gardner, J. E.; Hajimirza, S.; Webster, J. D.; Gonnermann, H. M. *Geochimica et Cosmochimica Acta* **2018**, *226*, 174.

(6) Lautze, N. C.; Sisson, T. W.; Mangan, M. T.; Grove, T. L. *Contributions to Mineralogy and Petrology* **2011**, *161*, 331.

(7) Zanotto, E. D.; James, P. F. *Journal of Non-Crystalline Solids* **1985**, *74*, 373.

(8) Cassar, D.; Lancelotti, R.; Nuernberg, R.; Nascimento, M.; M. Rodrigues, A.; Diz, L.; Zanotto, E. *The Journal of Chemical Physics* **2017**, *147*, 14501.

(9) Exner, H. E. In *Physical Metallurgy (Fourth Edition)*; Cahn, R. W., Haasen †, P., Eds.; North-Holland: Oxford, **1996**, p 943.

(10) Saltykov, S. *Stereology* **1967**, 163

(11) Lopez-Sanchez, M.; Llana-Funez, S. *Journal of Structural Geology* **2016**, *93*, 149.

(12) Lopez-Sanchez, M. *The Journal of Open Source Software* **2018**, *3*, 863.

(13) Pigeonneau, F. *Chemical Engineering Science* **2009**, *64*, 3120.

(14) Sturges, H. A. *Journal of the American Statistical Association* **1926**, *21*, 65.

(15) Doane, D. P. *The American Statistician* **1976**, *30*, 181.

(16) Pigeonneau, F. *Glass Technology: European Journal of Glass Science and Technology Part A* **2007**, *48*, 66.

(17) Barba Rossa, G., Université Grenoble Alpes, **2017**.

(18) Yaginuma, S.; Nakajima, C.; Kaneko, N.; Yokoyama, Y.; Nakayama, K. S. *Scientific Reports* **2015**, *5*.

(19) Cuzzi, J. N.; Olson, D. M. *Meteoritics & Planetary Science* **2017**, *52*, 532.

(20) Pigeonneau, F. *International Journal of Heat and Mass Transfer* **2011**, *54*, 1448.

(21) Pereira, L.; Podda, O.; Fayard, B.; Laplace, A.; Pigeonneau, F. *Journal of the American Ceramic Society* **2020**, *103*, 2453.

(22) Jones, S. F.; Evans, G. M.; Galvin, K. P. *Advances in Colloid and Interface Science* **1999**, *80*, 27.

(23) Pinet, O.; Phalippou, J.; Di Nardo, C. *Journal of Non-Crystalline Solids* **2006**, *352*, 5382.

(24) Boloré, D.; Pigeonneau, F. *Journal of the American Ceramic Society* **2018**, *101*, 1892.

(25) Duffy, J. A.; Ingram, M. D. *Journal of Non-Crystalline Solids* **1976**, *21*, 373.

(26) Cochain, B.; Neuville, D. R.; De Ligny, D.; Roux, J.; Baudelet, F.; Strukelj, E.; Richet, P. In *Journal of Physics: Conference Series* **2009**; Vol. 190.

(27) Manica, R.; Klaseboer, E.; Chan, D. Y. C. *Langmuir* **2015**, *31*, 6763.

(28) Cable, M. *Glass Technology: European Journal of Glass Science and Technology Part A* **2016**, *57*, 205.

(29) Hulburt, H. M.; Katz, S. *Chemical Engineering Science* **1964**, *19*, 555.

(30) Randolph, A. D.; Larson, M. A. *AIChE Journal* **1962**, *8*, 639.

(31) Marchisio, D. L.; Fox, R. O. *Journal of Aerosol Science* **2005**, *36*, 43.

Chapter 6

Novel method to infer bubble fraction in melts

Chapitre 6

Nouvelle méthode de détermination de la fraction de bulles dans la fonte

Résumé : Un matériau contenant une deuxième phase moins conductrice (*e.g.* des bulles), peut présenter une conductivité électrique globale plus faible. Nous proposons donc ici l'utilisation de la spectroscopie d'impédance *in situ* à haute température pour déduire la fraction volumique de bulles dans un bain de verre. Dans un premier temps, nous présentons les échantillons considérés. Pour confirmer la viabilité de cette nouvelle méthode expérimentale, trois autres méthodes robustes de la littérature sont exploitées et présentées dans ce chapitre. La détermination individuelle de la fraction de bulles est faite pour chaque méthode et une comparaison globale des résultats démontre la viabilité théorique et technique de cette nouvelle méthode *in-situ*.

Chapter 6

Novel method to infer bubble fraction in melts

At this point of this PhD manuscript, we have already investigated, using experiments and computer modeling, a single bubble system and a population of bubbles immersed in a borosilicate melt doped with cerium oxide. Experimentally the single-bubble system was investigated by *in-situ* camera imaging while the population of bubbles by *post-mortem* optical microscopic technique. As discussed in chapter 5, this last technique allow us to acquire different information about the bubbled-melt, including individual bubble information. However, due to the laborious and time-consuming characteristics of this approach, in this chapter, we present a novel method to infer, using an *in-situ* technique, bubble volume fraction of a melt, at high-temperature.

Here, based on the fact that a material containing a less conductive second phase (*e.g.* bubbles), presents lower overall electrical conductivity, we propose the use of impedance spectroscopy at high temperature to infer bubble volume fraction through the variation of electrical conductivity, in an *in-situ* mode. The use of this novel method is validated by comparing the obtained results with the ones from i) optical microscopy, ii) density measurements and iii) *post-mortem* impedance spectroscopy at low temperature (LT). At the end of this chapter, we present a general plot that contains the evaluated methods and the observed discrepancies are rationalized. The impact of high-temperature observation (*in-situ*) of the novel method is described as well.

Similarly to the studied case, ionic conductivity has been also applied to infer residual glass composition during glass crystallization as well to study liquid-liquid phase separation and structural relaxation of glasses.[1-4] This novel method brings the enormous advantage of being an *in-situ* technique, and due to this, a much easier and faster pre-synthesis step and no sample preparation steps are required. Therefore, a great time saving is achieved. Besides, it gives *in-situ* information and in this way, the idea of bubble/glass contraction/expansion during the cooling stage, which was previously ignored, now is taken into consideration. In practical ways, new glass formulation could be tested much easier and the fraction of bubbles would be accessed in a much faster and cheaper way than the ones currently available in the literature.

Since for a homogeneously dispersed phase, surface fraction, linear fraction and point fraction are statistically unbiased estimations of the volume fraction; in this chapter we fusion the terms bubble surface fraction and bubble volume fraction into one.[5] This terms will be called “bubble fraction”, and is described by ϕ_b.

6.1 Samples

To validate the use of high-temperature impedance spectroscopy to infer bubble fraction in a glass melt, we select the compositions used at the bubble population study (chapter 5). Thus, we select the borosilicate glass powder with controlled granulometry (250 – 500 μm), and cerium-IV oxide (< 5 μm), supplied by Aldrich and with chemical purity above 99.9 %. The final composition is composed by 0.1 wt% of Ce_2O_3 and it is presented in chapter 3 (section 3.1) along with the particle size distribution of the precursors. The glass transition temperature (T_g) of this final composition is 531 °C (804 K).

In this chapter, there are two groups of samples. The first one is the cerium-doped glass samples, which are firstly pre-synthesized, prepared, and then submitted to density and low-temperature impedance spectroscopic measurements. The second one can be described as synthesized directly inside the high-temperature impedance measurement system while electrical conductivity measurements are carried out, characterizing then an *in-situ* technique. It is important to emphasize that both series have exactly the same composition and the same synthesis historical is sought.

Samples from the first group are synthesized exactly like the ones from the bubble population study (chapter 5), but at just one temperature (1000 °C). For each sample of the first group, glass powder is initially mixed mechanically with CeO_2 and afterward, placed in a cylindrical alumina crucible (CeraQuest AC20), with an outer diameter, a height and a wall thickness equal to 30, 40, and 2 mm respectively. They are melted at 1000 °C for different durations: 20, 40, 60, 120, 240, and 360 min. The samples are subsequently removed from the furnace and are cooled down to room temperature in air. After being synthesized, these samples are cut in the middle and a parallelepiped sample of about 2 mm thick and with a surface of about 100 mm^2 is taken from it. **Figure 6.1** displays an optical microscopic image showing schematically the position and orientation where the sample is taken from the crucible. This parallelepiped solid sample is afterward polished and is used for density and low-temperature *post-mortem* impedance spectroscopic measurements.

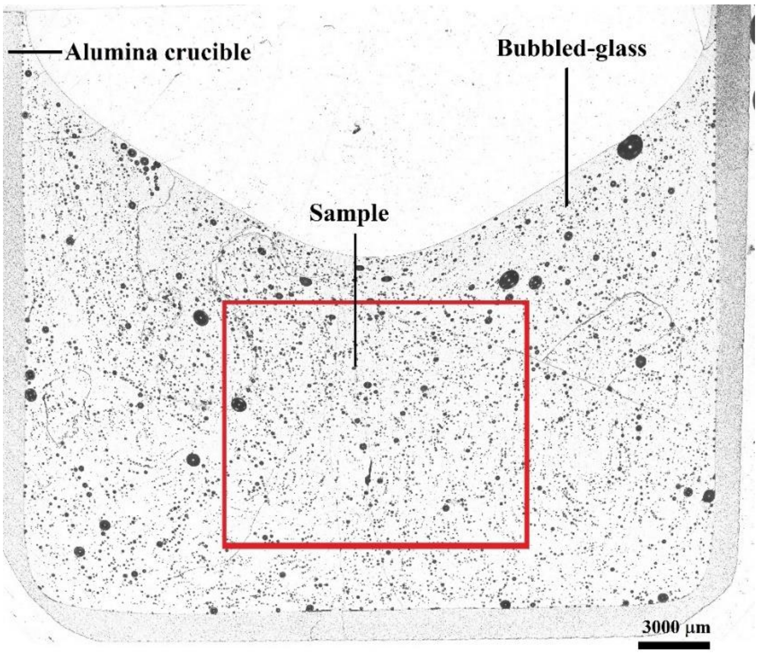

Figure 6.1: Optical microscope image of the glass sample synthesized at 1000 °C during 20 min showing the parallelepiped sample used for density and low temperature impedance spectroscopic measurements.

The sample of the second group, which is evaluated by high-temperature impedance spectroscopy, is synthesized by mixing mechanically the glass powder with $\mathrm{CeO_2}$ and melting the mixture in a platinum crucible with an outer diameter, a height and thickness equal to 30, 25, and 2 mm respectively. The crucible is previously filled up in a muffle furnace at 700 °C with about 50 g of the glass powder and $\mathrm{CeO_2}$ mixture that is partially added in three steps. After each mixture addition, the crucible is kept in the furnace during 20 minutes in order to sintering and create space for the next addition, up to the point where the crucible is nearly full filled. When this is achieved, the crucible is removed from the furnace and introduced in the high-temperature impedance measurement system. Bubble motion can be neglected in this pre-synthesis stage, because at 700 °C, this glass melt is extremely viscous (1.35 10^5 Pa.s). This value is obtained by the extrapolation of the VFT model fit presented in chapter 3 (section 3.2).

Figure 6.2 presents a scheme to illustrate these two samples groups used to validate the use of high-temperature *in-situ* impedance spectroscopy to infer bubble fraction. The scheme on the left is the *post-mortem* sample, called first group, which is evaluate by overall density, low-temperature impedance spectroscopy and optical microscopy. The one on the right is the *in-situ* sample, also called second group, and it is analyzed by high-temperature impedance spectroscopy.

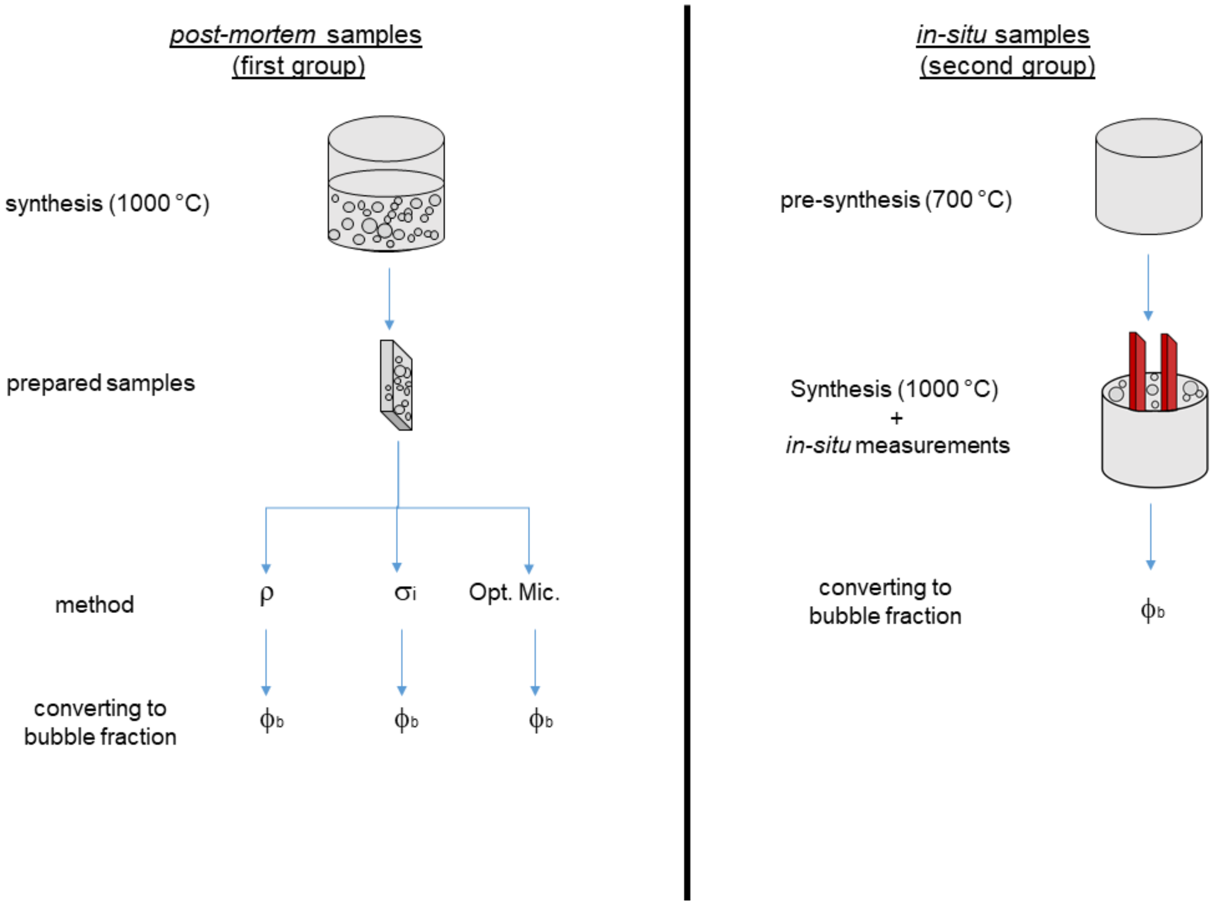

Figure 6.2: Scheme illustrating the *post-mortem* samples evaluated by density (ρ), ionic conductivity (σ_i) and optical microscopy (Opt. Mic.) and the *in-situ* sample that is evaluate by high-temperature electrical resistance.

6.2 Methods to infer bubble fraction

As previously mentioned, to validate the use of high-temperature impedance spectroscopy to infer bubble fraction in molten glass, we also examine the equivalent solid samples by two different methods besides the one already studied (optical microscopic approach). These two previous methods used herein are density and *post-mortem* impedance spectroscopic measurements on solid samples.

6.2.1 Density measurements

Density measurements on the bubbled glasses are performed at room temperature using Archimedean method having water as an immersion fluid and a Mettler AT200 scale.[6] Using this methodology, the density of a sample can be calculated by:

$$\rho = \frac{\mathrm{W_A} - \mathrm{W_N}}{\mathrm{W_A} - \mathrm{W_W}}(\rho_{\mathrm{w}} - \rho_{\mathrm{a}}) + \rho_{\mathrm{a}}, \tag{6.1}$$

where W_A the balance reading with the specimen on the stirrup above the water, W_N is the balance reading with no specimen, W_W the balance reading with the specimen on the submerged stirrup, ρ_w the density of water and ρ_a the density of air at the measurement temperature.

Once the density of the bubbled-glass is obtained, we can reach bubble fraction. Then it is determined by the ratio between the apparent density of this samples and a free-bubbled glass sample. Consequently, subtracting the glass fraction from unit, the bubble fraction is obtained. The free-bubbled glass employed as reference here is the one synthesized at 1000 °C during 360 min. The bubble fraction of this latter sample, acquired using *post-mortem* optical microscopic approach is around 0.005. In this study, an approximation to zero is assumed in order to have the similar sample historic in all of the investigated techniques, which will allow us to compare them directly afterward. It is important to emphasize that the same samples used here are also the ones used for the low-temperature spectroscopic measurements.

6.2.2 Low-temperature impedance spectroscopic measurements

Subsequently to the density measurements, gold electrodes about 100 nm thick are sputtered on both sides of the two opposite polished faces of the samples to ensure electrical contact. Impedance spectroscopic measurements are conducted using a Solarton 1260 Impedance/Gain Phase Analyzer over the frequency range 1 MHz - 1Hz with an applied root mean square AC voltage of 100 mV. A two-electrode cell configuration equipped with flat platinum plates is employed to facilitate efficient electrical contacts. Measurements are performed in air atmosphere and at temperatures below T_g, ranging from 600 to 800 K (327 – 527 °C). The furnace is set to a heating rate of 20 °C per hour and the impedance measurements are continuously performed every 30 minutes under heating. Since the impedance spectroscopic measurements takes about 2 min the variation temperature of the sample during the measurement is about 0.66 °C. A type S thermocouple is placed a few millimeters from the sample to assess the real temperature of the sample at the time of the measurement.

6.2.3 High-temperature impedance spectroscopic measurements

Impedance spectroscopic measurements are conducted using a Material Mates impedance analyzer over the frequency range 1 MHz – 10 Hz, with an applied root mean square AC voltage of 20 mV. Measurements are performed in a two-electrode cell adapted from a four-electrode cell.[7] The two-electrode setup is chosen because the four-electrode setup has two central electrodes that prevents bubbles from freely escaping. The sample pre-synthesized at 700 °C is placed in the high-temperature impedance spectroscopic measurement system and is heated up under a heating rate of 30 °C/min up to 1000 °C. The temperature of the crucible takes about 20 minutes to fully equilibrate as evidenced by temperature measurements taken with a type S thermocouple placed at the bottom of the crucible. Meanwhile, the two plate-like electrodes with dimensions of 12 mm x 8 mm and 10 mm away from each other are inserted in the melt. The electrode cell is coupled mechanically with a micrometric displacement system, allowing to detect the surface of the liquid with precision and therefore to plunge the electrodes to a reproducible depth. The detection of the surface of the liquid is based on the contrast between the impedance of the air and the low impedance of the liquid. The electrode cell is then inserted into the liquid to the immersion depth (around 6 mm below the surface). It is also important to keep the electrodes at a safe distance from the bottom of the crucible to avoid parasite current flowing through the platinum crucible wall (at least half of the distance that the electrodes have between them). Once the chosen temperature of 1000 °C is reached with a maximum variation over time of 1 °C, measurements are carried out in air during 720 min. This latter duration is selected just to double check that bubbled-melt resistance does not change considerably from 360 to 720 min.

6.3 Results

6.3.1 Apparent density

The glass fraction in the bubbled material can be determined by the ratio between the apparent density of the sample and a free-bubbled glass sample. Consequently, subtracting the glass fraction from unit, the bubble fraction is obtained, as follows:

$$\phi_{\mathrm{b}} = 1 - \frac{\rho_{\mathrm{bubbled}}}{\rho_{\mathrm{bubble-free}}}, \tag{6.2}$$

where ϕ_{b} is the bubble fraction while ρ_{bubbled} and $\rho_{\mathrm{bubble-free}}$ are the densities of the bubbled-glass, the free-bubbled one, respectively.

Figure 6.3 exhibits the bubbled-glass densities and bubble fractions evolutions for the glasses synthesized at 1000 °C for distinct synthesis durations (20, 40, 60, 120, 240, and 360 min), in which the last value, as mentioned above, is used as a free-bubbled glass. Indeed, the density of this last sample found by optical microscopic approach is around 0.005. In this way, by selecting the 1000 °C 360 min sample to be the reference sample of this study, we are capable to fairly compare the results of the different techniques, having a reasonable compromise between the minimization of the experimental time and maximization of accuracy.

As one might observe in **Figure 6.3**, a decrease of the apparent density occurs until it passes through a minimum around the synthesis duration of 60 min and increases afterward. Consequently, the bubble fraction behaves inversely, passing through a maximum at the same time and decreasing towards zero at the end. The same samples, as presented in chapter 5, were investigated by *post-mortem* optical microscopy, and it was demonstrated a similar behavior in terms of the evolution of bubble fraction as a function of time. Therefore, through this current technique, we confirm that the initial bubble fraction increase, as discussed in chapter 5, is not only an artefact of measurement but also a real phenomenon. It is believed that this initial increment could be indeed linked to the slow development of cerium redox reaction. Thus, bubbles are initially formed by air entrapment in the really beginning of the experiment and once cerium reduces, oxygen are produced and this gaseous species might either diffuse towards air bubbles or nucleate new bubbles. The former is more likely to happen due to the lower required energy.[8]

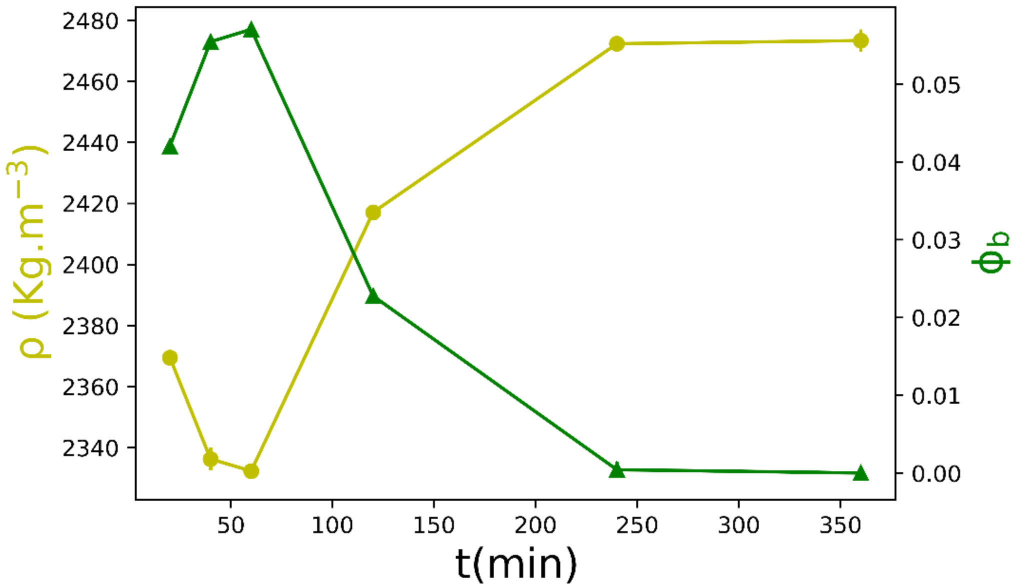

Figure 6.3: Apparent density and bubble fraction of glasses having different synthesis duration at 1000 °C. The standard errors are calculated based on three weightings of the same sample but, in most of the cases, the error bars are smaller than the symbols.

6.3.2 Low-temperature ionic conductivity

Still considering the *post-mortem* samples synthesized at 1000 °C under distinct dwell times, we aim now to verify if the electrical conductivity is sensitive enough to estimate bubble fraction. Besides, we also aim to verify if the cerium speciation have any influence on the electrical conductivity. The determination of the bubble fraction based on the electrical conductivity is only reliable if the conductivity of the glass phase remains unaffected as the bubble fraction evolves. In other words, the conduction mechanism should be the same regardless the evolution of cerium speciation. As demonstrated in chapter 5 (section 5.4), cerium reduction, from Ce(IV) to Ce(III), is limited by kinetics phenomena and therefore cerium speciation changes over time at 1000 °C for our melt system. Besides, cerium oxidation state influences on how this element would act in the glass structure, being either network-former or network-modifier. In this way, cerium speciation might also affect the electrical conductivity of the glass.[9,10]

Thus, we carry out *post-mortem* impedance spectroscopy at different temperatures, in order to determine the activation energy associate to the conduction mechanisms and evaluate whether or not the change in the cerium valence state affects the electrical conductivity of the glassy phase. The impedance responses of the glass samples display a usual ion-conducting behavior, typified by a straight and steep increase of the imaginary part of impedance (spike) at low frequency, jointly to the impedance response of the sample (semi-circle) at higher frequencies (**Figure 6.4**). The presented equivalent circuit is employed for impedance data fitting in order to identify and separate the contributions. Due to the nature of glass samples, containing both a resistive and capacitive characteristics, this kind of equivalent circuit is generally used by glass scientists.[11]

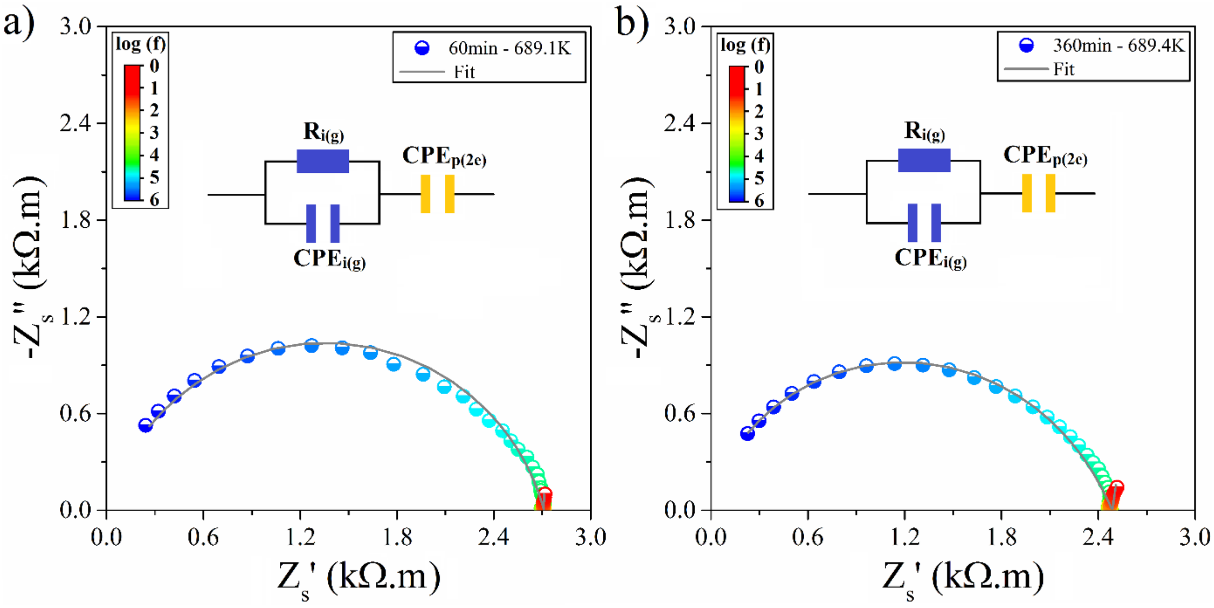

Figure 6.4: Typical complex impedance plots of Ce-doped glasses synthesized during a) 60 min and b) 360 min. Measurements are perform under T_g in the low-temperature impedance measurement system. The complex impedance data shown here have already been normalized regarding the shape factor of each sample for comparison purposes. The shown equivalent circuits are employed for impedance data fitting. Acronyms R and CPE represent resistive and constant phase elements. i and p denote ionic and polarization mechanisms; g and $\mathrm{2e}$ account for the glass sample response and the 2-electrode setup, respectively.

This low-frequency response is commonly denoted as a polarization effect and is given by the blockage of mobile ions at the interface glass/metallic electrodes.[12] A suitable equivalent circuit is employed to fit the impedance data and extract the resistance of the sample (**Figure 6.4**). The ionic conductivity of each sample is then calculated according to their resistance and their respective dimensions, given by:

$$\sigma_i = \frac{L}{RA}, \tag{6.3}$$

where L and A are the thickness and the surface of the sample, respectively, and R the electrical resistance. The ionic conductivity of the glass samples are determined in the range of temperature between 650 K – 750 K (376 – 476 °C). At temperatures lower than 376 °C the impedance of the samples falls out of the upper limit accuracy of the equipment and at temperatures higher than 476 °C the glass approaches its T_g changing the dependence of the conductivity with the temperature.

Finally, the dependence of ionic conductivity on the inverse of temperature is plotted applying the linearized form of the Arrhenius-like relation. σT-equation is chosen in this work instead of the σ-equation, because it is derived from the Nernst-Einstein equation,[13] which express a straight relationship between diffusion and conductivity.[14] This is expressed by:

$$\sigma_i T = A_i \exp\left(\frac{-E_a}{K_B T}\right), \tag{6.4}$$

where A_i is the pre-exponential factor, E_a is the activation energy for ionic conductivity, K_B is the Boltzmann constant, and T is the absolute temperature. Following this methodology, the slope of linear fit is proportional to the activation energy, which therefore provides access to the energetic barrier for ionic conductivity. **Figure 6.5** exhibits the Arrhenius-like plots of ionic conductivity, obtained by *post-mortem* impedance spectroscopy, of the glass samples synthesized at 1000 °C during different synthesis duration. As one might see, regardless the synthesis duration and consequently the cerium speciation, the slopes of linear fits are nearly the same. The calculated activation energy for ion conducting in all samples ranged from 1.018 to 1.022 eV and within errors originated from the linear fitting procedure, evidencing therefore, that under this conditions, the change of cerium speciation at the used concentration has no significant effect on the electrical conductivity of the researched glasses. Therefore, we can guarantee that electric conductivity variations during the process are not related to structural changes of the glassy matrix.

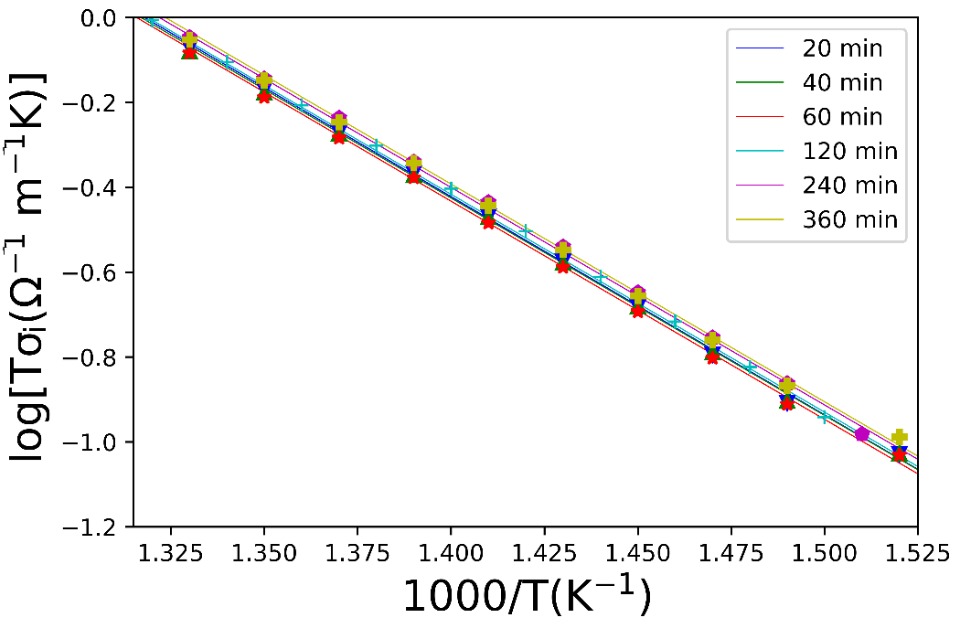

Figure 6.5 : Arrhenius-like plots of the ionic conductivity of glasses synthesized under distinct dwell time and consequently having different bubble fractions and cerium speciation.

By means of the linear fit curves from **Figure 6.5**, we can now estimate the conductivity at any fixed temperature within the studied temperature range (376 – 476 °C). Then, we can use the electrical conductivity to infer bubble fraction employing the Maxwell-Wagner equation derived from the “effective medium theory”.[15] The expression derived from this model and adapted for the present case is given by:

$$\frac{\sigma_{\mathrm{bubbled}}}{\sigma_{\mathrm{bubble-free}}} = \frac{2\sigma_{\mathrm{bubble-free}} + \sigma_{\mathrm{gas}} - 2\phi_{\mathrm{b}}(\sigma_{\mathrm{bubble-free}} - \sigma_{\mathrm{gas}})}{2\sigma_{\mathrm{bubble-free}} + \sigma_{\mathrm{gas}} + \phi_{\mathrm{b}}(2\sigma_{\mathrm{bubble-free}} - \sigma_{\mathrm{gas}})}, \tag{6.5}$$

where $\sigma_{\mathrm{bubbled}}$, $\sigma_{\mathrm{bubble-free}}$, and σ_{gas} are the electrical conductivities of the bubbled-glass, the free-bubbled one and the gaseous phase, respectively. ϕ_{b} is the bubble fraction of the analyzed bubbled-glass sample. By neglecting the electrical conductivity of the gaseous phase, Eq. (6.5) is reduced to the form:

$$\frac{\sigma_{\mathrm{bubbled}}}{\sigma_{\mathrm{bubble-free}}} = \frac{2 - 2\phi_{\mathrm{b}}}{2 + \phi_{\mathrm{b}}}. \tag{6.6}$$

Since the activation energy of all samples are the same, the choice of the temperature here is not important. Therefore, we choose the middle temperature (427 °C) to extract the conductivities of each sample and by applying Eq. (6.6), bubble fractions are obtained. **Figure 6.6** presents the overall electrical conductivity and the respectively bubble fraction of all glass samples synthesized at 1000 °C. Similarly to apparent density results, the electrical conductivity of the glass samples decreases as a function the synthesis dwell time up to around 60 min when this tendency is inverted. Conversely, the bubble fraction increases for short synthesis durations but around 60 min the bubble fraction starts to decrease with the synthesis time. In summary, the bubble fraction results appear to be in fair accordance with the density measurements as well as with optical microscopic ones presented previously in this document.

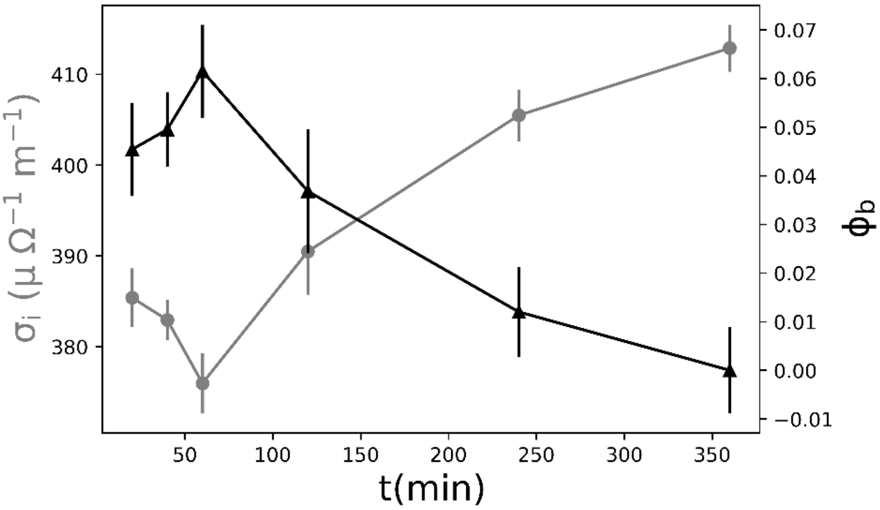

Figure 6.6: Electrical conductivity (σ_i) and the respectively bubble fraction (ϕ_b) of glass samples synthesized at 1000 °C for different synthesis durations. The standard errors presented here are propagated from the 95% confidence bands sourced from the Arrhenius linear fits.

Therefore, by using low-temperature impedance spectroscopic measurements we could confirm that cerium valence state, which changes over time at this studied situation, do not affect electrical conductivity. Thus, it allows us to apply high-temperature impedance spectroscopy to infer bubble fraction in an *in-situ* mode.

6.3.3 High-temperature ionic conductivity

Once bubble fraction is sensibly detected by *post-mortem* electrical conductivity measurements and the cerium speciation does not affect the electrical conductivity of the glass matrix, we present herein the results obtained by means of impedance spectroscopy at high temperature. In this step, we use the sample from the second group already pre-synthesized at 700 °C. This sample is evaluated by an *in-situ* technique using high-temperature impedance spectroscopy during the synthesis procedure. Thus, we can follow the bubble evolution process in the melt. During the measurement, bubbles are supposed to grow/shrink and leave the melt, causing changes in its overall electrical resistance. The impedance response of the melt also exhibits a usual ion-conducting behavior according with the straight and steep increase of the imaginary part of impedance (spike) at low frequency. Yet, as opposed to a glass ion-conducting behavior, the impedance response of the melt does not show any capacitive response at higher frequencies as one might expect, due to the melt structure mobility at temperatures above T_g (**Figure 6.7**). As we have done previously, an equivalent circuit proper to an ionic liquid is employed to fit the impedance data and extract the resistance of the sample (**Figure 6.7**).[7]

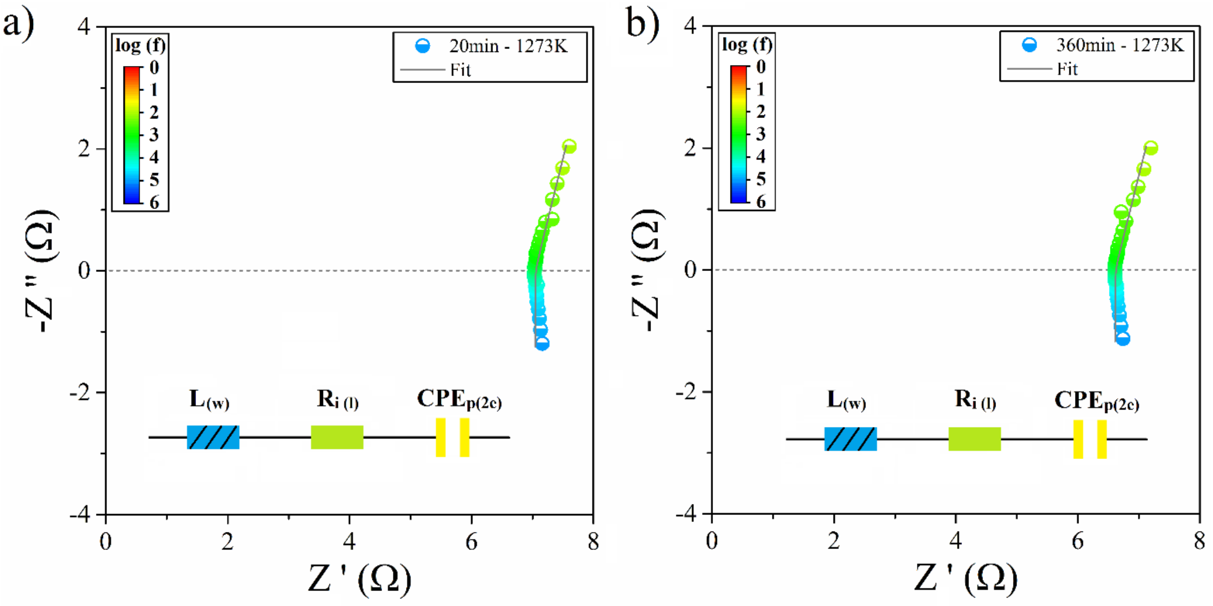

Figure 6.7 : Typical complex impedance plots of Ce-doped glass melts synthesized during a) 20 min and b) 360 min. Measurements are perform above T_g in the high-temperature impedance measurement system. The shown equivalent circuits are employed for impedance data fitting. Acronyms L, R and CPE represent inductive, resistive and constant phase elements. i and p denote ionic and polarization mechanisms; w, l and $\mathrm{2e}$ account for the cell wires, glass-forming liquid sample response and the 2-electrode setup, respectively.

Generally, the electrical conductivity is accessed by determining previously the shape factor of the cell (L/A ratio) by using an aqueous KCl solution of known conductivity which is often a demanding work.[7] However, in this case, we are interest in the ratio between the bubbled glass and the free-bubbled glass conductivities. Thus, the resistance of the melt is enough to determine the bubble fraction because the shape factor of the cell does not change during the *in-situ* impedance measurements. Consequently, by rearranging the Maxwell-Wagner model adapting it to the resistance, by utilizing Eq. (6.3), we can directly access the bubble fraction without determine the shape factor of the cell. This adapted form of Maxwell-Wagner model is:

$$\frac{\mathrm{R_{bubble-free}}}{\mathrm{R_{bubble}}} = \frac{2+\phi_b}{2-2\phi_b}. \tag{6.7}$$

Figure 6.8 presents the evolution of both resistance and bubble fraction applying the aforementioned model. Both of them behave similarly because in this case the electrical resistance and bubble fraction are directly proportional properties, giving rise to curves that have roughly the same behavior. Indeed, both resistance and bubble fraction increase in the initial moment and after 20 min of measurements, these features decrease. In summary, the bubble fraction evaluated by this current method also behaves similarly to the previous ones.

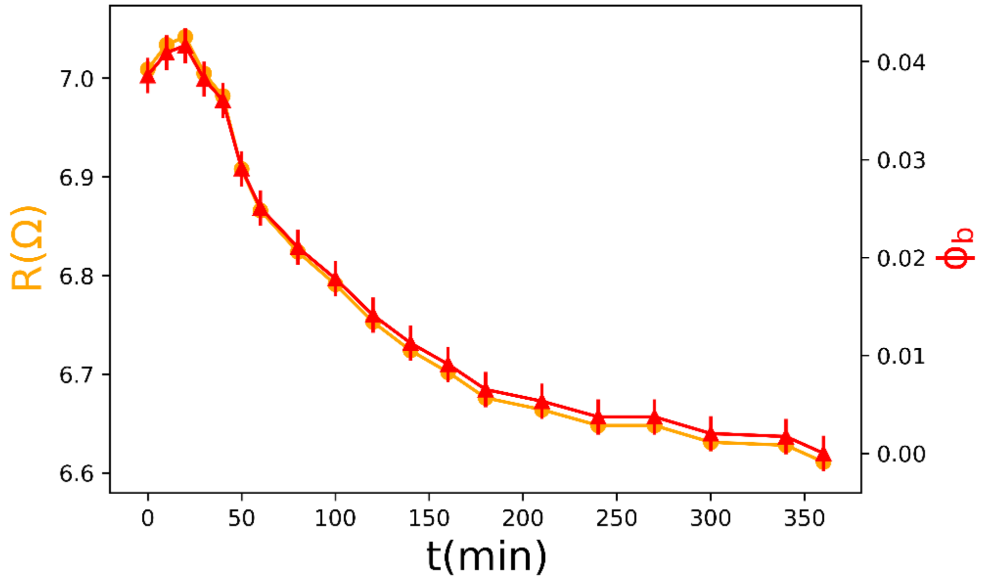

Figure 6.8: Electrical resistance (R) evolution, obtained by high-temperature impedance spectroscopy, and the respective bubble fraction (ϕ_b) versus time for the cerium-doped molten sample synthesized at 1000 °C.

6.3.4 Comparison of all investigated methods

A comparison among bubble fractions, evaluated by the presented methods, along with optical microscopic technique, is presented in this section. This last method is described in chapter 5 and here is applied to infer bubble fraction. **Figure 6.9** compiles bubble fraction results obtained by *post-mortem* density measurements, *post-mortem* low-temperature impedance spectroscopy and *in-situ* high-temperature impedance spectroscopy as well as *post-mortem* optical microscopic technique. It is important to emphasize that in this compiled result, optical microscopic technique is carried out on the same solid samples used for density and low-temperature measurements (**Figure 6.1**), and not on the whole crucible as done in chapter 5. Taking into consideration the overall evolution of the bubble fraction with time for the four methods, the sensitivity of the proposed electrical properties based-methods is acceptable.

Discrepancies of the employed methods are spotted but they can be rationalized. First of all, the *in-situ* high-temperature impedance method seems to have the bubble fraction peak shifted toward the left when compared to the other ones. This shift should be indeed expected once the *in-situ* high-temperature method takes between 20 and 30 min to reach the temperature of measurement (1000 °C). This duration is composed by the heating time from 700 to 1000 °C, along with the time spent to reach thermal equilibrium at the latter temperature. It enables then the evolution of bubble fraction before the beginning of the resistance measurements. On the other hand, the solid samples take around 3 min to reach the isothermal situation at high-temperature. The second and more important discrepancy can arise from a series of fundamental differences between the *post-mortem* and *in-situ* methods. The most likely, in our view, it would arise from the quenching effect on *post-mortem* synthesized sample. It is well known that thermodynamic properties like volume and even kinetic quantities, such as T_g, change with the cooling rate.[16] This idea is used in industrial process such as the production of tempered glass to create toughened glass sheets. In this process, the surface of the glass is rapidly frozen defining its apparent volume while the center would experience a slower cooling rate, resulting in a smaller equilibrium volume that cannot be fully accomplished creating compression and tensile stress in the surface and in the bulk, respectively.[17] Similarly, the same would happen in the quenched samples because the outer layer of glass is defined before the center cools down. However, in this case, the stress caused by unmatched volumes would be partially relieved by expanding the bubbles in the bulk before the inner super cooled liquid frozen into a glass. Consequently, *the post-mortem* samples would present higher bubble fraction when compared to the sample studied directly in liquid state.

Another observed discrepancy is the elevated values obtained by *post-mortem* optical microscopic approach. As previously mentioned, there are mathematical treatments proving that, for a homogeneously dispersed phase, area and volume fractions are equal.[5] Therefore, due to the transparency of the glass along with the depth of interaction, between light and matter, this mentioned method computes bubbles from more than a plan. It increases thus bubble surface fraction, that when converted, overestimate bubble volume fraction. Still comparing *post-mortem* optical microscopy with the other methods, one might question that the last value (360 min) is not equal to zero. This difference is because this microscopic methodology is an absolute and not relative, as the other ones.

In summary, the use of *in-situ* impedance spectroscopy to infer bubble fraction has in fact, a much easier and faster pre-synthesis step and no sample preparation is required. Therefore, great time saving is achieved. Besides, it gives *in-situ* information and in this way, the idea of the glass contraction/expansion during the cooling stage is not ignored, as it is for the *post-mortem* methods.

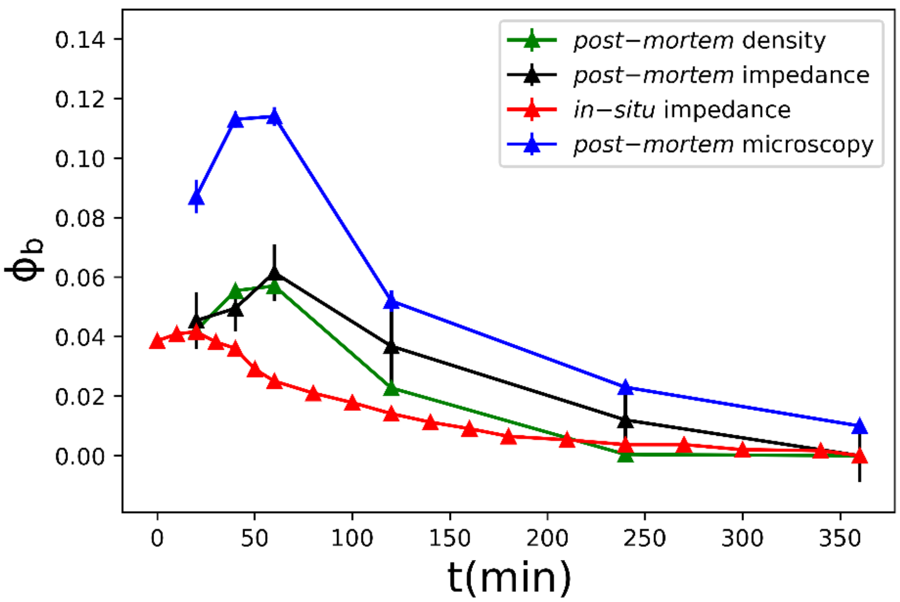

Figure 6.9: Bubble fraction (ϕ_b) evaluated by the four studied methods: *post-mortem* apparent density measurements and low-temperature impedance spectroscopy as well as *in-situ* high-temperature impedance spectroscopy.

Besides the validation of this methodology, it is now useful to confirm the idea previously mentioned in the chapter 5 (section 5.4). In this part of the manuscript, we raised a hypothesis that the increment of bubble fraction could be a physical phenomenon related to the kinetics of the cerium redox reaction at the studied temperature. Here, we proof therefore by different techniques that, indeed bubble fraction increases in the initial stages of the experiment at 1000 °C. So, it is not just an artefact of measurement but there is also a physical meaning. As previously mentioned, this increment could be due to nucleation of new bubbles or simple diffusion of formed molecular oxygen to the already formed air bubbles. Again, the latter is more likely to happen because it requires lower amount of energy.[8]

6.4 Conclusion

In this chapter we evaluated the use of high-temperature impedance spectroscopy as a technique to infer bubble fraction in molten glasses in an *in-situ* mode. After acquiring electrical resistance of the system, it is converted to bubble fraction by applying Maxwell-Wagner model. In order to validate the use of this technique, we compared the obtained results to *post-mortem* density, *post-mortem* impedance spectroscopy and *post-mortem* optical microscopy.

The main results demonstrate the theoretical and technical viability of this approach. Surely, this novel method has a great advantage, when compared to the *post-mortem* ones.

A much easier pre-synthesis step and no sample preparations are required. Thus, the time-consuming and laborious characteristics of the *post-mortem* approaches can be avoided. Besides, this novel technique gives an *in-situ* overview of the system and information that might be lost during the cooling stage is now taken into consideration.

Globally, the four examined methods present similar bubble fraction tendency over time. Higher values for bubble fraction are found for the case of *post-mortem* results when compared to the ones obtained by *in-situ* impedance spectroscopy. However, these discrepancies could be rationalized based on fundamental differences between the methodologies. Optical microscopic approach presented higher values when compared to the other applied methods. This last overestimation is believed to be due the type of image acquisition.

6.5 References

(1) Nuernberg, R. B.; Bello, T. S.; Fokin, V. M.; Zanotto, E. D.; Rodrigues, A. C. M. *Journal of Non-Crystalline Solids* **2019**, 510, 158.

(2) Prado, M. O.; Campos Jr, A. A.; Soares, P. C.; Rodrigues, A. C. M.; Zanotto, E. D. *Journal of Non-Crystalline Solids* **2003**, 332, 166.

(3) Ravagnani, C.; Keding, R.; Rüssel, C. *Journal of Non-Crystalline Solids* **2003**, 328, 164.

(4) Bragatto, C. B.; Cassar, D. R.; Peitl, O.; Souquet, J. L.; Rodrigues, A. C. M. *Journal of Non-Crystalline Solids* **2016**, 437, 43.

(5) Exner, H. E. In Physical Metallurgy (Fourth Edition); Cahn, R. W., Haasen†, P., Eds.; North-Holland: Oxford, **1996**, p 943.

(6) Cawthorne, C. D.; Sinclair, W. J., *Journal of Physics E: Scientific Instruments* **1972**, 5, 531.

(7) Simonnet, C.; Phalippou, J.; Malki, M.; Grandjean, A. *Review of Scientific Instruments* **2003**, 74, 2805.

(8) Jones, S. F.; Evans, G. M.; Galvin, K. P. *Advances in Colloid and Interface Science* **1999**, 80, 27.

(9) Mekki, A. *Journal of Electron Spectroscopy and Related Phenomena* **2005**, 142, 75.

(10) Deshpande, V. K.; Taikar, R. N. *Materials Science and Engineering: B* **2010**, 172, 6.

(11) Nuernberg, R., UFSCar and University of Montpellier, **2018**.

(12) Jayasinghe, G. D. L. K.; Dissanayake, M. A. K. L.; Bandaranayake, P. W. S. K.; Souquet, J. L.; Foscallo, D. *Solid State Ionics* **1999**, 121, 19.

(13) Einstein, A. *Annalen der Physik* **1905**, 322, 549.

(14) Nuernberg, R. B. *Ionics* **2020**, 26, 2405.

(15) Barsoukov, E.; Macdonald, J. R. *Impedance Spectroscopy: Theory, Experiment, and Applications*, **2005**.

(16) Zheng, Q.; Zhang, Y.; Montazerian, M.; Gulbiten, O.; Mauro, J. C.; Zanotto, E. D.; Yue, Y. *Chemical Reviews* **2019**, 119, 7848.

(17) Lee, E. H.; Rogers, T. G.; Woo, T. C. *Journal of the American Ceramic Society* **1965**, 48, 480.

Chapter 7

Conclusion

Chapitre 7

Conclusion

Résumé : Dans cette dernière partie, un récapitulatif de chaque chapitre est réalisé, avant de résumer les avancées propres à la thèse. Nous récapitulons également les interrogations posées en début du manuscrit et auxquelles une réponse a été apportée durant cette thèse. Enfin, des perspectives sont proposées en se basant sur les limitations rencontrées au cours de ce travail.

Chapter 7

Conclusion

7.1 General conclusion of this PhD thesis

In this PhD thesis, we investigated bubbles in an oxide glass melt in nuclear waste vitrification context. We focused on oxygen bubble formation and behavior linked to redox reaction of a multivalent element. Thus, this thesis was articulated between these two previous topics: oxygen production by redox reaction and bubble formation linked to it. We simplified the glass system by choosing a borosilicate composition doped with just one multivalent element (cerium). We did not try to investigate oxygen bubbles in a specific vitrification process. This study concerned mostly with events taking place in a fundamental scale, being therefore a generalized study which could be applied to different vitrification processes.

In the first stage of this PhD work, we characterized the glasses and the melts, in terms of physical and thermochemical properties (viscosity, density high-temperature, density room-temperature, surface tension, oxygen fugacity and others). These characterizations were useful for the interpretation of the experimental results as well as for feeding the numerical model and for probing some mechanisms. Since there is a lack of information in terms of borosilicate melt properties in the literature, we have added some of these characterizations to one of our articles (Pereira *et al.* 2020a).[1]

Later, we investigated, by experimental and numerical means, mass transfer of a single-oxygen bubble freely rising in the borosilicate melt. The experimental part was carried out using *in-situ* camera imaging device. Several situations, for varying cerium loadings (wt% $\mathrm{Ce_2O_3}$) and redox ratios ($\mathrm{Ce(III)/Ce_{total}}$) have been analyzed. The results confirmed that cerium redox reaction significantly enhances the mass transfer, mainly in reduced states and high cerium oxide contents. A theoretical model assuming instantaneous redox reaction and a diffusion dominated by molecular oxygen allowed, globally, to explain the experimental results (Pereira *et al.* 2020a).[1]

Afterward, an expansion of the single-bubble system to a bubble population scenario was carried out. As previously done, we also investigated by numerical and experimental approaches. Experimentally, we applied *post-mortem* optical microscopic technique to study this system. By using this approach along with some characterizations, we presented some insights in terms of cerium redox reaction, bubble formation as well as bubble behavior in the studied melt. The melting of a granular medium, composed by glass beads, led to a bubble population nucleated mainly due to air trapping. Assuming that the bubble dynamics was driven by the residence time of bubbles in the crucible, the overall dynamics at various temperature were similar (Pereira *et al.* 2020b).[2] A numerical model based only on mass transfer did not estimate bubble behavior. Thus the suggested idea is that coalescence should be taking place. Indeed, it has been also observed experimentally that some bubbles were undergoing coalescence.

Therefore, up to here, we could answer some of the questions displayed in the introduction of this document. We could understand the type of bubble nucleation, which was created by air trapping during granular medium melting. Moreover, by applying the mass transfer numerical model along with some experimental results, we concluded that besides mass transfer, coalescence is one of the main growth mechanisms. Besides, experimental results, as just mentioned, gave us insights about the bubble behavior as function of temperature and time. All of these insights were obtained with the help of laboratory experiments and numerical computations.

Lastly, due to the laborious and time-consuming characteristics of the *post-mortem* optical microscopic approach, we proposed the use of high-temperature impedance spectroscopy, as a novel method to infer, in an *in-situ* fashion, bubble volume fraction in glass melts. Indeed, the results demonstrated the theoretical and technical viability of this approach. It has an advantage of time-saving as well as giving information at high-temperature, avoiding then the loss of information that may occurs during the cooling stage (Pereira *et al.* 2021a).[3]

7.2 Suggestions for future works

This doctorate is one of the first works, executed by our research team, to understand how oxygen bubbles linked to redox reactions are formed in nuclear waste vitrification context. Even though we answered several questions of the introduction, we still have several questions to ask and some suggestions for future work.

In terms of single-bubble study, the use of the mass transfer model in a system with a multivalent element, which exchanges more than one electron has not yet been explored. In this context, chromium would be a good candidate in industrial and nuclear waste vitrification context.[4,5] Furthermore, the cerium redox situation at low temperature (900 and 1000 °C) caught our eyes. Results demonstrate a low reduction rate from $Ce(IV)$ to $Ce(III)$. Evidences suggested that it could be limited by CeO_2 particles dissolution and/or low O_2 diffusion from the reaction site.[6,7] Thus, a possible future study would be the kinetics of dissolution of CeO_2 particles in melts and more calculations of diffusion of redox products from the reaction site. Finally, as mentioned, mass transfer numerical results for bubble population study showed that another growth mechanism would be taking place. Indeed, experimental and numerical results demonstrated that coalescence should be taking place. Then, another interesting work for the future would be the coupling between mass transfer and coalescence into a model to predict bubble behavior in this type of melt.

7.3 References

(1) Pereira, L.; Kloužek, J.; Vernerová, M.; Laplace, A.; Pigeonneau, F. *Journal of the American Ceramic Society*, *in press.*

(2) Pereira, L.; Podda, O.; Fayard, B.; Laplace, A.; Pigeonneau, F. *Journal of the American Ceramic Society* **2020**, *103*, 2453.

(3) Pereira, L.; Neyret, M.; Laplace, A.; Pigeonneau, F.; Nuernberg, R. B. *International Journal of Applied Glass Science* (**submitted**).

(4) Gin, S.; Jollivet, P.; Tribet, M.; Peuget, S.; Schuller, S. *Radiochimica Acta* **2017**, *105*.

(5) Vernaz, E.; Gin, S.; C, V.; Elsevier: Amsterdam, **2012**; Vol. 5, p 451.

(6) Cochain, B., Université Paris VI **2009**.

(7) Cochain, B.; Neuville, D. R.; De Ligny, D.; Roux, J.; Baudelet, F.; Strukelj, E.; Richet, P. In *Journal of Physics: Conference Series* **2009**; Vol. 190.

RÉSUMÉ

Ce doctorat est réalisé dans le cadre de la vitrification des déchets nucléaires et est focalisé sur la production de gaz formé lors du processus de vitrification à haute température. Nous nous concentrons sur l'oxygène moléculaire produit par des réactions d’oxydo-réduction d'éléments multivalents. En effet, ces éléments sont présents dans plusieurs domaines naturels et industriels. Cette thèse vise à comprendre, fondamentalement, les mécanismes de formation et de croissance des bulles d'oxygène et comment ceux-ci sont liés aux réactions d’oxydo-réductions se déroulant dans ce contexte. Nous avons choisi un système de verre nucléaire simplifié composé d'un verre borosilicaté dopé avec l'oxyde de cérium. Pour étayer notre compréhension de la formation et de la croissance des bulles, nous avons caractérisé le système simplifié en termes de propriétés physiques et thermochimiques.

Nous avons tout d’abord étudié le transfert de masse entre une bulle d'oxygène et la fonte verrière avec différentes teneurs en cérium (% $\mathrm{Ce_2O_3}$) et différentes fugacités en oxygène ($\mathrm{f_{O_2}}$). Cette étude a été menée à la fois par des moyens expérimentaux et numériques. Les résultats confirment que la réaction d’oxydo-réductions du cérium augmente de façon significative le transfert de masse pour les milieux réduits et à forte teneur en oxyde de cérium. Un modèle théorique considérant les réactions d’oxydo-réductions comme instantanées et une diffusion dominée par celle de l'oxygène permet globalement de retrouver les résultats expérimentaux.

Nous avons ensuite étendu le système à une population de bulles. Cette partie de la thèse a également été abordée par des moyens expérimentaux et numériques. En faisant fondre un milieu granulaire, constitué de grains de verre, la nucléation des bulles est principalement liée à l'emprisonnement de l'air. En considérant que la dynamique des bulles est pilotée par leurs temps de résidence dans le creuset, le comportement des bulles à différentes températures se révèle équivalent. Un modèle numérique basé sur le simple transfert de masse ne permet pas d'estimer le comportement des bulles, ainsi la coalescence des bulles devrait être prise en compte.

Enfin, nous avons proposé une nouvelle méthode *in-situ* pour déterminer la fraction volumique des bulles. Nous avons démontré la viabilité théorique et technique de cette nouvelle méthode en utilisant d'autres approches robustes de la littérature.

MOTS CLÉS :

fonte de verre d’oxyde, bulles, réaction d’oxydo-réduction, méthode expérimentale, méthode numérique.

ABSTRACT

This doctorate takes place in the framework of nuclear waste vitrification and it deals with gas production occurring during the high-temperature process. We are focused on molecular oxygen produced by redox reactions of multivalent elements. Indeed, these elements can be found in different contexts, including natural and industrial systems. This thesis aims to understand, fundamentally, the mechanisms of oxygen bubble formation and growth and how they are linked to redox reactions taking place in this context. We have chosen a simplified nuclear glass system composed of a borosilicate glass doped with cerium oxide. To support the understanding of bubble formation and growth in this given context, we characterized the simplified system in terms of physical and thermochemical properties.

First, we studied the mass transfer between an oxygen bubble and the melt, for varying cerium contents (% $\mathrm{Ce_2O_3}$) and oxygen fugacities ($\mathrm{f_{O_2}}$). This study was carried out by both experimental and numerical means. The results confirm that cerium redox reaction significantly enhances the mass transfer, mainly in reduced states and high cerium oxide contents. A theoretical model assuming instantaneous redox reaction and a diffusion dominated by molecular oxygen allows, globally, to explain the experimental results.

Afterward, we expanded the study to a bubble population scenario. This part of the work has also been investigated by both experimental and numerical means. The melting of a granular medium, composed of glass beads, leads to a bubble population nucleated mainly due to air trapping. Assuming that the bubble dynamics is driven by their residence time in the crucible, the overall dynamics at various temperatures is the same. A numerical model based only on mass transfer does not estimate bubble behavior, and consequently coalescence should be taken into account.

Finally, we proposed a novel *in-situ* method to infer bubble volume fraction. We demonstrated the theoretical and technical viability of this novel method by comparing the results with other well-established approaches from the literature.

KEYWORDS:

oxide melt, bubbles, redox reaction, experimental approach, and numerical approach